Formation and Evolution of Extreme Debris Disks through Giant Impacts of Planetary Embryos

Lewis Watt

A thesis submitted to the University of Bristol
in accordance with the requirements of the degree of
Doctor of Philosophy
in the Faculty of Science

School of Physics,
H.H. Wills Physics Laboratory,
Tyndall Avenue,
Bristol,
BS8 1TL

December 2022

$\sim 37,000$ words

Abstract

In many formation scenarios, it is necessary for giant impacts between planetary embryos to form the terrestrial planets we find within our own Solar System. Giant impacts will eject a substantial amount of material to the surrounding stellar environment. The material will form a disk that potentially can be observed from outside the system. A subclass of debris disks known as extreme debris disks are candidates for recent evidence of a giant impact. Extreme debris disks are bright and warm which usually places them close to their host star within the terrestrial planet formation space. Typically they are observed around young stars with ages less than 200 Myr which places them in the expected time for late-stage terrestrial planet formation that involves giant impacts.

Extreme debris disks are often observed with variability within their lightcurves on yearly and sub-yearly timescales which is much shorter than the variability expected from traditional debris disk on the scale of millions of years. Some variability within extreme debris disks has been observed to be periodic. The periodicity has been linked to giant impact produced dust forming an asymmetric disk with two pinch points: the collision point and anti-collision line. In chapter 3 of this thesis we show how a giant impact can form the periodic variability seen in some extreme debris disks. We also show how the behaviour of an extreme debris disk formed from giant impacts differs with varying collision parameters through many simulations. One main result we find is that all giant impacts produce dust anisotropically and the orientation of the giant impact within the stellar system will change the behaviour seen in the lightcurve of the disk.

For the extreme debris disks to be observable soon after the giant impact, it is assumed that the vaporised escaping ejecta from the giant impact will form small grains with typical sizes of $\mu\mathrm{m} - \mathrm{mm}$. It is expected that the small vapour condensate grains will collisionally evolve very quickly to sizes below the blowout size of the star. The expected fast removal of dust does not line-up with the multi-year observations of extreme debris disks. Some extreme debris disks have exhibited increases in their lightcurves more steady than expected if caused by a giant impact. It has been proposed that a boulder population made of planetesimals formed from the ejecta of a giant impact could sustain the extreme debris disk for longer than expected if only made up of vapour condensate grains. We show in chapter 4 simulations and analysis of a collisionally evolved planetesimal population formed from giant impacts for varying disk

and collision parameters. For disks placed close to the star that the collision rate between the planetesimals is substantial enough to sustain an extreme debris disk through extremely destructive collisions between planetesimals. The evolution of the collision rate is consistent across all varying parameters and it is the initial collision rate which sets how many collisions will take place in a boulder populated disk.

Acknowledgements

I would like to thank my supervisors Dr. Zoë Leinhardt and Dr. Phil Carter whose support and advice has helped me greatly throughout my PhD. I would also like to thank Dr. Kate Su for giving an observers perspective to the first piece of published work I did, and Dr. Jack Dobinson for helpful discussion on radiative transfer and N-body code. Thank you to all the academics and staff within the astrophysics department for being very friendly and helpful. Thank you to my parents for always being supportive. Finally, thank you to everyone within my cohort and those that I shared an office with. It was very fun to study with you all and the support you all showed me got me through the tough points. I would like to especially thank Cai Wood whose photos of his dog Maude and more recently of his son Otto Wood were always uplifting and a delight to see.

This work was carried out using the computational facilities of the Advanced Computing Research Centre, University of Bristol - http://www.bristol.ac.uk/acrc/. I acknowledges support from an STFC studentship (grant number: ST/S505274/1)).

COVID-19 Statement

I acknowledge the impact that COVID-19 had on the research within this thesis. Due to time lost the scope of research for chapter 4 was reduced and limited. Radiative modelling was removed from planned work for chapter 4, as was simulating a more complex collision criteria. I did not have time to explore a singular model for vapour condensate disk and the boulder populated disk, instead we treated these as two separate entities in chapter 3 and chapter 4. The future work in chapter 5 outlines the potential directions that the research could have gone in if time was not lost due to the COVID-19 pandemic.

Declaration

I declare that the work in this dissertation was carried out in accordance with the Regulations of the University of Bristol. This work is original except where indicated by special reference in the text and no part of the dissertation has been submitted for any other degree. Any views expressed in the dissertation are those of the author and in no way represent those of the University of Bristol. The dissertation has not been presented to any other university for examination either in the United Kingdom or overseas.

I note here any contributions to the work from collaborators for each of the individual chapters.

Chapter 3 – *Planetary Embryo Collisions and the Wiggly Nature of Extreme Debris Disks* – This chapter is published as "Planetary Embryo Collisions and the Wiggly Nature of Extreme Debris Disks" Watt, L., Leinhardt, Z. and Su, K., Monthly Notices of the Royal Astronomical Society, Volume 502, Issue 2, April 2021, Pages 2984–3002, https://doi.org/10.1093/mnras/stab106. I conducted all of the numerical simulations, analysis and wrote the paper. My coauthors provided the general topic, critical feedback and discussion on my work.

Chapter 4 – *Post-Giant Impact Planetesimals Sustaining Extreme Debris Disks* – This chapter is a second paper that I have written but has yet to be submitted. The paper is a collaborative project with my two thesis supervisors Dr. Zoë M. Leinhardt and Dr. Phil Carter. Again I have been solely responsible for completing all of the numerical simulations, analysis and writing supported by discussion and feedback from my coauthors.

Other Work – "Isolating the extreme debris disc signature - explorations of eccentric extreme debris discs formed by giant impacts", Lewis, T. Watt, L. and Leinhardt, Z., Monthly Notices of the Royal Astronomical Society, Volume 519, Issue 1, February 2023, Pages

172–191, https://doi.org/10.1093/mnras/stac3541 – This paper is a continuation of the research presented in chapter 4. This research was completed as a Masters by Research project by Thomas Lewis. My contribution was the initial idea for the project. I also provided background SPH simulations and N-body code used in the work as well as constructive feedback and discussion on the paper. The paper is referenced in chapter 5.

Contents

List of Figures

List of Tables

1

Introduction

Planetary formation is complex and results in diverse outcomes. The drive to understand it is a quest to ultimately understand how we came to be. The last quarter of a century has been a golden age to study planetary formation with the discovery of thousands of exoplanets (5227 as of 12/06/2022 NASA Exoplanet Archive (2022)). Many systems include objects like Hot Jupiters (short period giant planets), Mini-Neptunes (planets with masses much larger than Earth but small than ice giants), and Super-Earths (terrestrial planets that are about ten times the mass of Earth) that are not found within our own Solar System. With all systems forming from similar building blocks of the interstellar medium, the diverse range of systems indicates that the formation of planetary systems is a complex and intricate process. Exoplanet systems offer a snapshot into the final configurations which can occur, but to study the overall formation of a planet we need information on every step of the process. Various ground and space based observations have allowed us to peak into parts of the formation process, but to fully grasp the full formation process theoretical numerical models are needed to complete the dynamical picture.

The focus of this thesis is to better understand the late-stage formation of terrestrial planets and how impacts between embryos are linked to the sudden influx of vapourised material which produces a bright extreme debris disk. With the removal of gas from the protoplanetary disk, planetary embryos enter a period of chaotic encounters which result in highly excited systems. The planetary embryos are then either excited onto unbound orbits or collide with one another. Impacts between planetary embryos often have significant energy which allows the vapourisation and ejection of a substantial amount of material into the surrounding environment. The

vapour material will condense into small grains and form a bight asymmetric disk which has initial conditions linked to the characteristics of the impact which formed it. Bight disks with little gas are often classed as extreme debris disks. Our work focuses on the formation, observability and lifetime of extreme debris disks through numerical modeling of giant impacts and evolution of debris disks post-giant impacts.

1.1 Overview

It is no understatement that the discovery of the first exoplanet orbiting around the pulsar PSR B1 257+12 (Wolszczan & Frail, 1992) caused a revolution in our understanding of how planetary systems form. PSR B1 257+12 was an exciting discovery as it showed us planets can survive around evolved stars which had gone supernova. Planets around evolved stars were not part of the formation model of planets at that point. Before this discovery the only data points we had were the planets within our Solar System. Based on the organisation of our own solar system planets were assumed to form in-situ, meaning that planets formed in their present day configuration. The discovery of the first exoplanet around an evolved star, and subsequent exoplanets thereafter have shown us many systems are not like our own with the in-situ formation model potentially not always a good fit for exoplanet systems, and maybe even our own Solar System.

The first exoplanet discovery around a main sequence star was 51 Pegasi b (Mayor & Queloz, 1995). 51 Pegasi b is a Jupiter-sized planet that has a semi-major axis of 0.05 au. As it sits so close to the star, it is tidally locked and has a day side temperature of 1300 K (known as a Hot Jupiter). 51 Pegasi b was discovered using the radial velocity technique. Fig. 1.1 shows the orbital motion of 51 Pegasi. The radial velocity technique is an indirect detection method that uses the fact that the centre of mass of the star-planet system is off-set from the centre of the star itself. Planets orbiting around a star gravitationally interact with the star so that the star has a small orbit about the centre of mass of the whole system. If the star has motion along our line of sight then the light we measure from the star will be Doppler shifted as the star moves towards and away from us. More massive and closer in planets will cause greater displacement of the star and larger Doppler shifts.

The discovery of 51 Pegasi b was a major breakthrough in understanding the formation mechanisms of planets within stellar systems as it provided evidence for migration. A Jupiter mass planet cannot form so close to the host star because it is too hot but a planet like 51 Peg

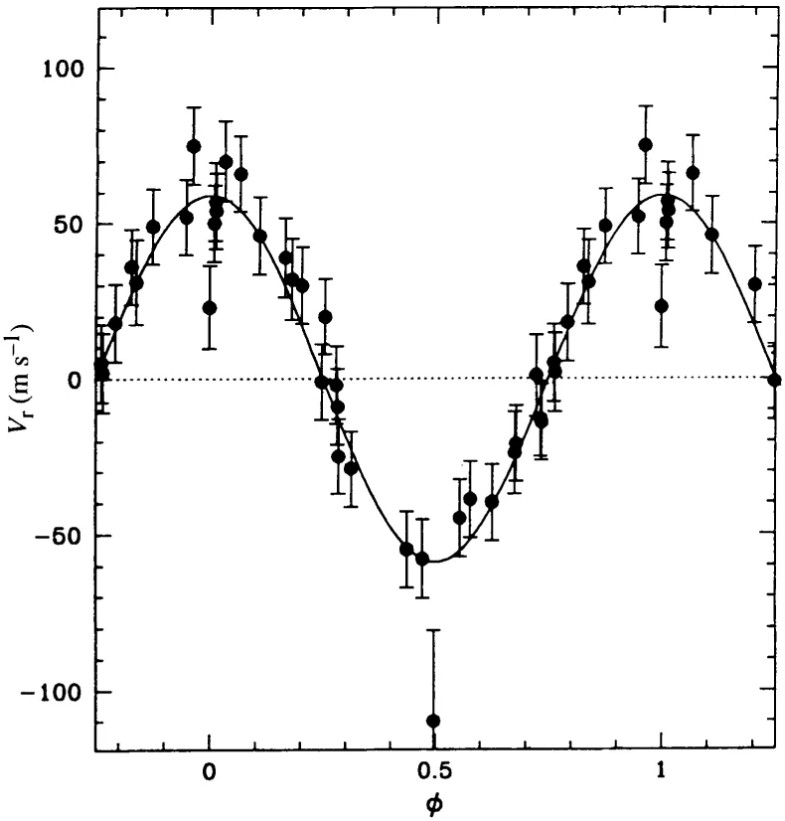

Figure 1.1: The orbital motion of 51 Pegasi corrected from the long term variation of the centre of mass velocity. The data points are obtained from four different epochs between September 1994 and 1995 using the ELODIE spectrograph located in Haute–Povence Observatory. The solid line represents the fit to the data calculated from parameters displayed in Table 1 from Mayor & Queloz (1995). Fig. 4 from Mayor & Queloz (1995).

could have initially formed beyond the snow-line where volatiles could condense and move closer to the central star after formation instead of forming in-situ (Lin et al., 1996). 51 Pegasi b and the discovery of many other Hot Jupiter systems led to a rethink of planetary formation mechanisms. Typically it is now thought that gas giants migrate through the disk via type II migration. A planet with enough mass will form an annular gap within the protoplanetary disk. The inner disk and outer disk repel the planet to the centre of the gap. The planet migrates inward as long as gas is accreted onto the star (for a review on planet-disk interactions see Baruteau et al., 2014).

Besides Hot Jupiters, there are many other examples of systems which host planets which are very different to planets within our own Solar System. Many systems host planets known as Super-Earths and Mini-Neptunes. Others are extremely compact in resonant or near-resonant chains like the TRAPPIST-1 (Luger et al., 2017) and Kepler 107 (Bonomo et al., 2019) systems. The process which forms the very diverse cast of planetary systems cannot happen in-situ. Current models suggest a few methods of structuring the inner terrestrial region of systems. These models are motivated by the search for planets which could support life. By understanding our own formation story, we can better plan for missions which would search for and detect similar planets to Earth. Early work focused on the formation of the terrestrial planets in isolation. Greenberg et al. (1978) simulated the growth of ~ 500 km sized objects from a swarm of km sized planetesimals. The collision outcomes of planetesimals were adopted from experimental and theoretical impact results allowed collision outcomes such as rebound, cratering and catastrophic fragmentation. Kokubo & Ida (2002) investigated the formation of protoplanetary systems from planetesimal disks spanning from 0.5 au to 1.5 au. A perfect merging regime was used to grow protoplanets within these simulations. It was shown that perfect merging could be assumed as it only decreased the formation timescale of protoplanets. Overall, the oligarchic growth model, where embryo-planetesimal/embryo-embryo collisions are on average merging and planetesimal-planetesimal collisions are on average destructive, held for a wide variety of planetesimal disks. With a fragmentation model for collisions Leinhardt & Richardson (2005) got results for the formation of protoplanets from planetesimals that were indistinguishable from Kokubo & Ida (2002). Many early models had difficulties exactly matching the properties of the early Solar System. One big difference between the models and what we observe is the mass of Mars. Dubbed the 'small Mars problem', models often overestimated the mass of Mars.

Other formation models looked at the whole stellar system and how material outside the

terrestrial zone could sculpt the architecture of the terrestrial zone. These typically include migration of material from the outer solar system to the inner solar system either through migration of giant bodies like Jupiter, drifting inwards of smaller material or instabilities causing material to get kicked into and out of the inner solar system. Some of these models are summarised below.

- Early Instability - The Early Instability model (Clement et al., 2018, 2019, 2021) is built on the Nice model (Gomes et al., 2005; Tsiganis et al., 2005; Morbidelli et al., 2005). The Nice model developed to explain the Late Heavy Bombardment which was a spike in the impact rate on Solar System bodies a few hundred million years after the start of planet formation. It suggested that the trigger for the Late Heavy Bombardment was an instability between the giant planets' orbits. The cause was gravitational interactions between the giant planets and a planetesimal disk exterior to their orbits.

  The Early Instability model invokes the same instability between the giant planets within our Solar System but sets the time for the instability to occur when terrestrial planet formation is taking place. An additional giant planet is added in the Early Instability model which is ejected after the instability is triggered. The trigger for the instability is caused by the dispersal of the gas disk which shifts the orbits of the giant planets as it disperses outwards.
- Grand Tack - The Grand Tack model (Walsh et al., 2011) was proposed to solve the 'small Mars problem' when simulating the formation of the terrestrial planets through the depletion of material in Mars' feeding zone (Hansen, 2009). The scenario plays out like so: 1) Jupiter migrates inwards as Saturn is forming. The inward migration causes the inner disk to become excited causing the removal of a large amount of material from Mars' feeding zone. 2) Saturn, when nearly fully grown, starts to migrate inwards more rapidly than Jupiter until both are in a 3:2 mean motion resonance (Pierens & Raymond, 2011). 3) Both planets then migrate outwards until the disappearance of the gas in the disk.
- Pebble Accretion - Pebble accretion occurs when aerodynamically small particles coupled to the gas within a protoplanetary disk are accreted onto a gravitationally large body. Pebble accretion onto a body only depends on the mass of the body not its radius. In the pebble accretion regime pebbles streaming into the hill sphere of the large object are captured within a cross-section much larger than the radius of the body (Ormel, 2017). The pebble accretion model of forming terrestrial planets assumes that planetesimals are formed at specific locations in the disk through some mechanism such as the streaming instability in multiple

generations (Johansen et al., 2021). Planetesimals that become massive enough pebble accretion starts and the planetesimals migrate inwards. The terrestrial planets are formed from the migrating planetesimals growing in size due to pebble accretion. The pebble accretion model can reduce the number of collisions needed to form the inner Solar System down to a minimum of one collision – the Moon-forming impact. The impact is needed to produce an Earth that is more massive than Venus which otherwise would not happen. The model does come under some criticism. The isotopic distribution of material in the terrestrial planets should show a mix from the outer and inner regions of the Solar System if pebble accretion is the main driver of formation. Burkhardt et al. (2022) show that the outer Solar System material is limited in Earth and Mars to only a few percent of their mass. This would refute the pebble accretion model of forming the inner terrestrial planets.

- Convergent Migration - The Convergent model suggests that there is a "sweetspot" for converging migrations which happens at around the Earth's semi-major axis (Brož et al., 2021). Material migrates from either side of the "sweetspot" to form the most massive object (the Earth). The less massive objects then form as a function of distance away from the "sweetspot" as there is less material feeding these objects. This can explain the distribution of terrestrial planets we see in the Solar System. A giant impact is still needed to form the Earth-Moon system.
- Low Mass Asteroid Belt - The low mass asteroid belt model simply suggests that the region which Mars feeds from in its formation is simply depleted of material (Raymond & Izidoro, 2017). Models have suggested that planetesimals form in narrow rings as opposed to a broad disk. This is because planetesimals form from coagulation of dust at certain locations in the disk. Observations of dust rings in protoplanetary disks also suggest that narrow band planetesimal formation is taking place. The model suggests that Mars sits between two such narrow bands of planetesimals. The modern day asteroid belt would be made up of material from captured planetesimals from the outer and inner bands of planetesimals.

As the gas dissipates, all models point to at least one giant impact within all planetary systems. Most suggest a period of dynamically excited planetary embryos, whether it occurs from mutual gravitational interactions in the post-gas disk (Low Mass Asteroid Belt) or stirring from external bodies (Grand Tack and Early Instability). The different models will vary in the rate of collisions between planetesimals and planetary embryos. For most objects in the disk, the lack of gas allows embryos within the disk to dynamically excite one another through gravitational

interactions as the interactions are no longer damped through gas drag. Impacts now on average are more energetic which leads to a change from average growth to an average destructive collision regime. Only the planetesimals that grew into planetary embryos will continue to grow and accrete their final few percent of their total mass. Giant impacts between planetary embryos in this stage are not perfect merging events. A percentage of the mass, dependent on the specific energy of the impact, will be ejecta escaping into the surrounding area. One example is the canonical Moon-forming impact which has a Mars-sized body (named Theia, Halliday, 2000) glancing a proto-Earth with a low velocity (Canup, 2004, 2008). In the canonical Moon-forming impact, 37% of the giant impact ejecta will be accreted by Earth and Venus. A further 8% will be ejected by Jupiter or other minor bodies in 10 Myr (Jackson & Wyatt, 2012). Note that recent work indicates that the Moon formed from a different type of impact to that in the canonical case. In the short term, the ejecta should be observable as an infrared excess, for the Moon-forming impact it has been estimated the disk will be observable at 12 μm and 24 μm for at least 100 years and with potential uncertainties up to 10 million years (Wyatt & Jackson, 2016). Disks produced from giant impacts offer us an insight into planetary formation if we can observe one. Observed warm and bright debris disks known as extreme debris disks are often linked to a recent giant impact. Extreme debris disks then can be a probe for ongoing terrestrial planet formation. These probes can help give insight to the formation processes which occur such as the occurrence rate of giant impacts. Many planetary formation mechanisms which form the terrestrial planets of the Solar System have tens of impacts occur between embryos. Understanding how extreme debris disks evolve over time can help us determine which formation mechanism is potentially dominant. Extreme debris disks are observed around tens of stars but if giant impacts are meant to be a common feature of terrestrial planet formation why do we not observe more around young stars? Is this because giant impacts are a rare event like pebble accretion or convergent migration might suggest or do these disks have such short lifetimes hence have a low probability to be observed?

1.2 Planet Formation

1.2.1 Protoplanetary Disks

Protoplanetary disks are the birth places of planets. A protoplanetary disk forms from a stellar nebula just after the collapse of a core that forms a star. The material that initially surrounds

the forming star flattens into a disk through angular momentum conservation. These disks contain the same building blocks as the star, with the disk being made up of 99% gas and 1% dust (Williams & Cieza, 2011). The dust content of a protoplanetary disk initially shares the composition of diffuse interstellar medium (ISM) dust. The dust is mainly composed of silicates with sizes less than 0.1 microns. There are also other components such as graphite grains and poly aromatic hydrocarbons (Draine, 2003). In molecular clouds, molecules will freeze out from the gas and form icy mantles on the surfaces of dust grains (Bergin & Tafalla, 2007). Over time the dust grains will collisionally agglomerate.

The gas in the disk orbits at sub-Keplerian speeds. The inner disk rotates faster than the outer part, causing a frictional torque on the gas. The 'slow' gas in the disk has a huge impact on the transfer of mass. If it is assumed that the disk is in a steady-state, then mass flow is constant and independent of orbital distance. Gas will inflow onto the star at a velocity

$$v_r = \frac{3\nu}{2r}, \tag{1.1}$$

where r is the orbital distance and ν is the viscosity of the disk. The small grains ($d \lesssim 0.1\ \mu\mathrm{m}$ where d is the size of the grain) that initially make up the bulk dust mass in the disk have a large surface area-to-mass ratio and their motion is coupled to the gas. As the grains grow, the surface area-to-mass ratio decreases and the larger grains decouple from the gas. The larger grains experience a drag force from the gas and settle towards the mid-plane of the disk (Williams & Cieza, 2011).

1.2.2 Formation of Planetesimals

For planets to form, dust must be funnelled to build a larger object. This must either happen through a bottom up scenario where intermediate sized objects are formed through core accretion or through a top down scenario like direct collapse through a gravitational instability. The gravitational collapse of dust to form large cores was proposed to form giant planets like Jupiter (Boss, 1997, 2011), though mass-metallicity relations suggest a core accretion scenario (Thorngren et al., 2016; Ginzburg & Chiang, 2020). For giant planets on wide orbits, the disk instability model is a potential mechanism of formation as further out in the protoplanetary disk the radiative cooling rates are higher and the Toomre criterion (Toomre, 1964) is lower (Cai et al., 2006). However for planets within tens of au to have formed through a disk instability both Toomre criterion would not be filled and the cooling timescale to be small enough which is

unlikely. It has also been shown that irradiation of a protoplanetary disk stabilises a disk from gravitational instabilities further making it disk instability unlikely (Matzner & Levin, 2005). Further evidence shows that the composition of terrestrial planets including Super-Earths and Mini-Neptunes are too refractory rich, where refractory rich is material with high condensation temperatures so cools into solids early during cooling of the protoplanetary disk. It is likely that these planets formed from a bottom up mechanism. The formation of planetesimals happens early in the lifetime of a system but the exact time range for their formation is not totally clear. We can identify a minimum age through analysing unmodified meteorites that include various components with different ages. This is assuming that the oldest meteorites are similar to the planetary building blocks planetesimals formed from. Calcium-aluminium rich inclusions (CAIs) are the oldest formed components we find within meteorites (Amelin et al., 2010). Using isotope dating we know that planetesimals form after the formation of CAIs though we do not know for certain if some planetesimals formed before CAIs. The planetesimals that formed planets must have formed before the dispersal of the gas disk in order for there to be a proto-Jupiter. This sets an upper limit on the formation time of planetesimals used in planet formation. It can be argued that the gas disk lasted at least ~ 3.7 Myr after CAI formation from paleomagnetic measurements and petrographic observations of chondrules from the CR chondrites (Schrader et al., 2018; Fu et al., 2020), and in a similar process looking at CH chondrites (Morris et al., 2015) it is estimated the disk dissipated between ~ 3.8 and 4.8 Myr after CAI formation. The process by which planetesimals form is still uncertain.

The dust within a protoplanetary disk starts off with sizes ranging from sub-micron to centimetre dust grains. The gas in the disk acts to slow the collisional velocity of the dust so that dust grains stick together. The dust grains coagulate through this process until around a metre in size. The sticking velocity is material dependent. Ices are easier to stick together (Blum & Wurm, 2008) which is why larger planets are found to have formed past the snow-line. Once the dust coagulations start to reach a metre in size, the growth past this point is not fully understood. As objects grow in size they will feel an increasing drag force from the sub-Keplerian orbiting gas with the drag force being maximal for metre-sized objects (Wettlaufer, 2010). Metre-sized objects spiral into the star on extremely quick timescales. With the large drift speeds, collisions are in a destructive regime rather than a growth regime. This issue, coupled with the fast removal of boulders due to inward migration, is called the metre-sized problem.

One model invokes a streaming instability to overcome the metre-sized problem. The streaming instability stems from the drifting objects exerting a friction on the gas. The interaction leads to a small overdensity of particles accelerating the gas, diminishing the difference from the Keplerian speed. The drift speed of local particles is reduced inside the instability, which leads to a runaway process where particles drift into the dead-zone and the density exponentially grows. These highly dense regions reach densities several thousand times the density of the surrounding gas. The high density of material triggers a gravitational collapse to form planetesimals with a characteristic size of $\sim$100 km (Johansen et al., 2015; Simon et al., 2016).

Once planetesimals have formed they continue to grow through two potential methods, pair-wise accretion and pebble accretion. Pair-wise accretion involves planetesimals growing through collisions between similar sized bodies. Typically the phase of accretion is known as runaway growth which is defined to start when,

$$\frac{d}{dt}\frac{M_1}{M_2} > 0, \tag{1.2}$$

where M_1 is the big object and M_2 is the small object. In runaway growth, gravitational focusing is efficient due to the gas dampening the relative velocities between planetesimals. Here we can define a gravitational focusing factor between two planetesimals as,

$$F_g = 1 + \frac{v_{esc}^2}{v_{rel}^2}, \tag{1.3}$$

where v_{rel} is the relative velocity between the two planetesimals and v_{esc} is the mutual escape velocity of the planetesimals. The escape velocity is found through a function of their masses and radii,

$$v_{esc}^2 = \frac{2G(M_1 + M_2)}{(R_1 + R_2)}. \tag{1.4}$$

As a planetesimal continues to grow and increase in mass, the gravitational focusing factor grows larger if the relative velocities stay damped. This leads to a positive feedback loop in which the mass of the planetesimal grows increasingly quickly. The orbital parameters, such as eccentricity and inclination, of the largest bodies in runaway growth are kept small due to dynamical friction with the smaller bodies (Wetherill & Stewart, 1989; Ida & Makino, 1992).

The runaway growth of planetesimals stops when the largest planetesimals start to govern the dynamics of the system. The condition this occurs at is when $v_{esc} \sim v_{rel}$ so that $F_g \sim 1$. Here the largest objects can be defined as planetary embryos and will continue to grow through an oligarchic process of accreting many planetesimals. The growth of smaller planetesimals is

limited as the relative velocities between them are increased to the point that growth impacts are not common (Kokubo & Ida, 1998, 2000).

1.2.3 Growth of Planetary Embryos

The largest planetesimals in the system which we now will call planetary embryos dominate their local area and grow through an oligarchic regime. A planetary embryo starts to dominate their local area when their mass roughly exceeds 100 times that of the average planetesimal (Ida & Makino, 1993). The random velocities of the neighbouring planetesimals are then tied to the planetary embryo by $v_{rel} \propto M^{1/3}$ where M is the mass of the planetary embryo. In oligarchic growth, the growth between neighbouring planetary embryos is orderly. A process known as orbital repulsion keeps neighbouring planetary embryos at approximately 10 mutual Hill radii apart. The Hill radius, $r_{\rm H}$, is defined as

$$r_{\rm H} = a(1-e)\sqrt[3]{\frac{m}{3M}}, \tag{1.5}$$

where m is the mass of the smaller body (e.g. Earth), M is the mass of the larger body (e.g. Sun), a is the semi-major axis and e is the eccentricity. If two planetary embryos form closer, gravitational interactions between the bodies will act to grow the eccentricity and inclinations of the bodies, widening the orbits between them. The smaller planetesimals will then act to re-circularise the orbits of the planetary embryos through dynamical friction (Kokubo & Ida, 1995). Planetary embryos will continue to grow through feeding on planetesimals in their local area.

After the dispersal of gas from the disk, gravitational interactions between planetary embryos mutually excite their orbits, leading to an increase in eccentricities and inclinations in the whole system. Known as the chaotic growth phase, planetary embryo orbits are altered and can intersect one another. The intersecting orbits will lead to giant collisions between planetary embryos (Chambers & Wetherill, 1998). A standard disk model suggests that Mercury and Mars are left over planetary embryos with a quick formation time, $<$10 million years (Raymond et al., 2014). In this pair-wise growth of planetary embryos, it is roughly expected that in the formation of the terrestrial planets, most would have undergone mutliple giant impacts (Quintana et al., 2016).

An alternative to pair-wise growth is growth through pebble accretion. Planetesimals with enough mass will have a much larger cross-section than their physical radius as particles drift

into their area of influence. The final mass of the objects formed from pebble accretion is then reliant on the radial pebble flux. A larger pebble flux will form super-Earth objects while a reduced pebble flux will result in Moon and Mars sized objects (Lambrechts et al., 2019). The pebble accretion model in Johansen et al. (2021) suggests that all terrestrial planets in our Solar System formed from pebbles. While pair-wise accretion models can well match the masses and orbits of the terrestrial planets today, the pebble accretion model is better at explaining how we get to the compositions we see today. Though as noted earlier, the pebble accretion model claim of matching the compositions we see today is challenged by Burkhardt et al. (2022). The only giant impact suggested in the pebble accretion model is the Moon forming impact between a proto-Earth and another planetary embryo.

1.3 Debris Disks

Here I outline the importance of studying debris disks and the sub-classification extreme debris disks.

1.3.1 Traditional Debris Disks

Debris disks were initially classified as disks of solid material with little to no detectable gas. They typically are thought to have a typical size distribution of particles defined by the largest object within the disk and a minimum size related to the size needed to efficiently remove particles through radiation pressure. The evidence for gas in debris disks has led to a change in the definition in which debris disks are defined as optically thin while protoplanetary disks are typically optically thick. They form from protoplanetary disks after the dispersal of the gas through various mechanisms such as photoevaporation, stellar winds and the building of large gravitationally bound bodies such as Jupiter-like objects. The transition from a protoplanetary disk to a debris disk can be traced through measuring near-IR excess. Near-IR disk emission is indicative of dust within 1 au of the star, and for sun-like stars near-IR disk emission decreases from near 100% to 0% over 6 Myr (Hernández et al., 2007). While the near-IR excess tracks dust within 1 au, it is thought that the dust is dragged into the inner stellar system by gaseous accretion disk processes. The lack of near-IR excess at levels between those observed for protoplanetary disks and debris disks after accretion onto the star has ceased suggests that the transition is rapid (Williams & Cieza, 2011). Debris disks are not just the left-over material though as an active

process called a steady-state collisional cascade replenishes the small grains that are lost over time through the grinding down of large objects in the disk. An example of a traditional debris disk is seen in our own Solar System. Fig. 1.2 shows a systematic view of the components that make up a debris disk within our Solar System and demonstrates how a measured SED would look (figure 1 from Hughes et al., 2018). An external observer would see two components to the debris disk in our Solar System; one being a warm component in the inner Solar System (Zodiacal cloud) made up of material from disintegrated comets flung in by Jupiter, and a cold component (Kuiper Belt) which extends from outside Neptune's orbit to around 50 au. Both components are too faint to be observable outside the Solar System, hence debris disks observed around other stars are assumed to be scaled up larger and/or more massive versions of our own system. Multi-component debris disk systems are good evidence for a planetary system as planets are efficient at shepherding debris into disks (Shannon et al., 2016).

The study of debris disks is important as it is not only an indicator for successful planet formation, but the structure and composition of dust in the disks can tell us the architecture of the planets that reside within and the building blocks used to grow these planets. As the surface area of debris disks is dominated by small millimetre/micron grains, they are infrared bright. The primary method of detection is through measuring the spectral energy distribution (SED) of the system. With the star modelled as a blackbody, the presence of a debris disk will cause the SED to deviate from a single blackbody with an excess of infrared being measured. It is assumed that the SED of the disk itself can also be described by a separate blackbody (Chen et al., 2006; Hillenbrand et al., 2008), hence it is possible to characterise the deviations away from the system SED through the addition of the blackbody components within the debris disk. The deviations away from the stellar SED is wavelength dependent as different wavelengths probe different grain sizes. Dust grains only emit efficiently (thermal and scattering) at wavelengths shorter than their physical size (Hughes et al., 2018). Therefore the intensity observed at a specific wavelength is dominated by the smallest grain size that can emit efficiently. Small grains of comparative sizes to near-IR wavelengths need to be hotter than grains with sizes similar to mid-IR wavelengths to emit efficiently. Hence, different wavelengths will probe different areas of the disk with shorter wavelengths probing the inner warmer disk and longer wavelengths probing the outer colder disk (Wyatt, 2008). Often debris disks are found in large infrared surveys. Discoveries have used: Infrared Astronomical Satellite (IRAS Neugebauer et al., 1984),

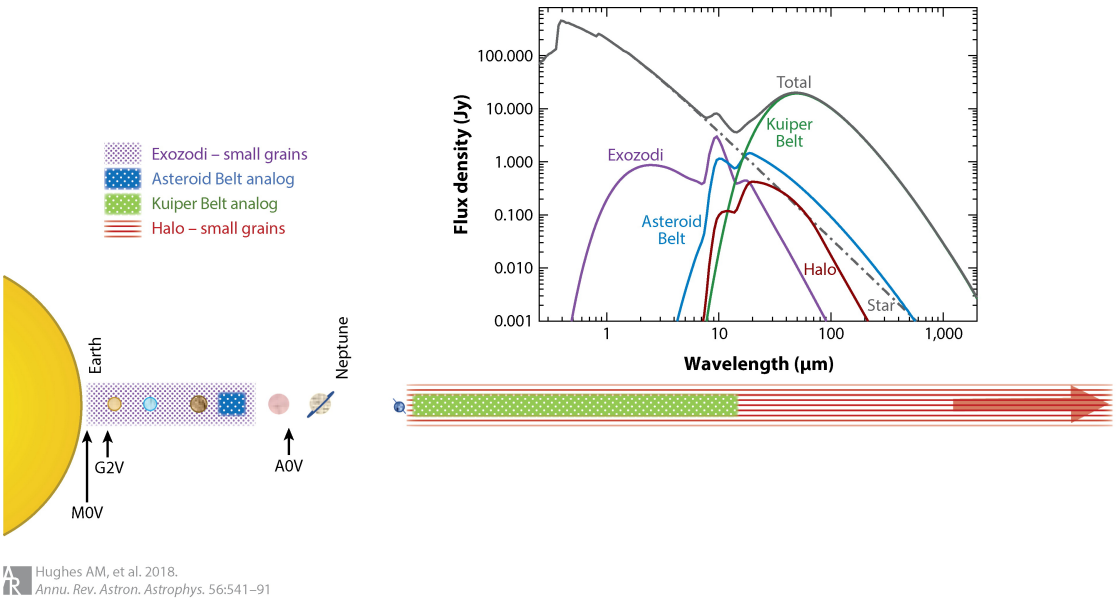

Figure 1.2: A systematic view of components that make up the debris disk within our Solar System with illustrative SED. Figure 1 from Hughes et al. (2018).

the Spitzer space telescope (Werner et al., 2004), AKARI (Murakami et al., 2007), the Wide-Field Infrared Survey Explorer (WISE Wright et al., 2010) and the Herschel Space Observatory (Pilbratt et al., 2010). The first debris disk observed was around Vega by IRAS in 1984 (Aumann et al., 1984).

The dynamical perturbations caused by the formation of protoplanets can cause collisions between planetesimals to transition from net accretion events to net destruction events. This transition starts a collisional cascade which depletes the disk of large objects over time. In the process small dust grains are produced. The lifetime of the debris disk is then set by the mass of the largest objects in the collisional cascade. All 'settled' debris disks are sustained through a steady-state collisional cascade of material. The small dust grains which are lost from the disk are replenished over time through collisions of larger objects. The observable disk therefore only makes up a small percentage of the total mass in the disk. A steady-state collisional cascade results in a size distribution which follows a power law such that,

$$\frac{dN}{da} = a^{-q}, \tag{1.6}$$

where a is the grain size and q takes on a value between 3-4 (Dohnanyi, 1969). Most of the mass in a debris disk is found in the largest objects while the surface area is dominated by the smallest

grains. Material close to and smaller than the blowout size from a debris disk is lost over time through radiation blowout (Thébault & Augereau, 2007). Other processes such as stellar winds and Poynting-Robertson drag also contribute to removing dust from the system. The blowout grain size is the grain size at which the ratio between forces is such that,

$$\beta_{forces} = \frac{F_{rad} + F_{wind}}{F_{grav}} \geq \frac{1}{2}, \tag{1.7}$$

where F_{rad} is the force on the dust from radiative pressure, F_{wind} is the force acting on the dust from stellar winds, and F_{grav} is the gravitational force acting on the dust from the star. As a consequence of how they evolve, material close into the star is processed quicker as the disk evolves on orbital timescales as the collisional cascade of material occurs on orbital timescales. Hence, debris disks clear inside-outwards.

The main observational difference between protoplanetary disks and debris disks is that debris disks are typically optically thin across the EM spectrum while protoplanetary disks are optically thick at optical wavelengths. The observational metric often used for debris disks is the fractional luminosity defined as $f = L_{disk}/L_*$, the ratio between the excess luminosity from the disk and from the star respectively.

By observing debris disks we can understand the their composition. The building blocks for debris disk formation are the same as for planet formation so dust composition in debris disks gives us a window into the materials used in building exoplanets. The Spitzer mission observed many debris disks from which it was found that the dust composition is dominated by common silicates (Olofsson et al., 2012; Mittal et al., 2015). Typically traditional debris disks have $f \leq 10^{-4}$ and evolve on Myr timescales.

1.3.2 Extreme Debris Disks

Extreme debris disks are labelled extreme as they have unusually bright fractional luminosity of $f \geq 10^{-2}$ and are often variable on short timescales as short as years or even months. Extreme debris disks are found around only $\sim 1\%$ of stars aged between 3-150 Myr (Balog et al., 2009). Though the fraction of extreme debris disk detection increases up to $\sim 10\%$ for stars in young clusters with ages between 2-40 Myr (Meng et al., 2017). The extreme debris disk population is mostly around young stars with ages less than 200 Myr, bar a few exceptions like TYC 8830-410-1 which is highly variable but not periodic with an age >500 Myr (Melis et al., 2021) and BD+20 307 around a >1 Gyr star (Weinberger et al., 2011). The bright near-IR excess seen from

extreme debris disks either suggests there is a massive population of planetesimals supplying a collisional cascade close to the star or that the near-IR excess is produced through other means.

It is expected that giant impacts will produce vast quantities of ejecta (Jackson & Wyatt, 2012; Genda et al., 2015; Kenyon & Bromley, 2016). It is not clear what the size distribution of material will be of ejecta from giant impacts but evidence from cratering impacts suggest that a standard size distribution seen in traditional debris disks will not be formed. In fact, different characteristic sizes will be formed depending on what state the material was shocked to (Johnson & Melosh, 2012, 2014). The variability in the lightcurves of extreme debris disks on timescales of years and months indicate that they do not meet the criteria of a steady state collisional cascade (Meng et al., 2015; Wyatt & Jackson, 2016; Su et al., 2019). It is thought that giant impact ejecta will form disks with a non-standard size distribution which could lead to a substantial small grains of size similar to near-IR wavelengths. It is expected that the small grains will be processed and removed from the system extremely quickly (Meng et al., 2012, 2015; Wyatt & Jackson, 2016; Su et al., 2019) leading to a large change within the near-IR excess when the small grains are added to the system and also when removed. The creation of ejecta from a giant impact can also potentially explain why some disks show periodic variability on smaller than orbital timescales (Jackson & Wyatt, 2012; Jackson et al., 2014; Su et al., 2019). As the fractional luminosities do not match models for usual steady-state collisional cascades, along with them being highly variable and existing around young stars at an age terrestrial planet formation can take place they are inevitably linked to potential giant impacts between planetary embryos. Examples of EDDs are given in table 1.1, from which we see that many EDDs are observed around young stars.

One extremely bizarre disk surrounds the solar-like star ID8 and shows many different behaviours which could indicate a recent giant impact (Meng et al., 2012, 2014, 2015; Su et al., 2019). ID8 was observed as part of the Spitzer warm mission at 3.6 and 4.5 μm between 2012 and 2017. The time series excess for ID8 and P1121 is shown in fig. 1.3 which is fig. 1 from Su et al. (2019). The short wavelengths trace hot dust that sits close to the star. At small semi-major axis, the impact velocity between two objects can massively exceed the mutual escape velocity resulting in mass vaporisation of the colliding material. Over the five year period, the disk massively decreased in near infrared flux twice, once in late 2012/ early 2013 and another between 2015 and 2016. The disk also had a massive increase in flux from 2013 to the peak in late 2014, and a steady increase in flux from late 2015 onwards. Within the time-series excess, there was

Table 1.1: Observed extreme debris disk examples. Citations along with age of the system in Myr, the location of the disk around the star in au and if any short-term variability is observed is given. Short-term variability is defined as variability observed in the light curve on timescales that correspond to the orbital timescales of the disk's location.

Name	**Citations**	**Age (Myr)**	**Location (au)**	**Short-term Variability**
HD 113766	Su et al. (2020)	$\sim$20	0.5 – 1.2	no
HD 145263	Fujiwara et al. (2013); Lisse et al. (2020)	$\sim$10	$\sim$3	maybe
HD 15407	Melis et al. (2010); Meng et al. (2015)	80	$\sim$0.6	no
HD 165012	Fujiwara et al. (2010); Lisse et al. (2015)	< 100	$\sim$0.7 – 4.4	no
HD 166191	Su et al. (2022)	$\sim$10	$\sim$0.62	no
HD 23514	Rhee et al. (2008); Meng et al. (2015)	120	~ 0.25	no
ID8	Gorlova et al. (2007); Su et al. (2019); Meng et al. (2012, 2014, 2015)	35	0.32 – 0.64	yes
P1121	Gorlova et al. (2004); Meng et al. (2015) Su et al. (2019)	80	0.2 – 1.6	maybe
Rz Psc	de Wit et al. (2013)	30 – 40	$\sim$0.5	yes
TYC 4209-1322-1	Moór et al. (2021)	$\sim$275	$\sim$0.3	yes
TYC 8241-2652-1	Melis et al. (2012); Günther et al. (2017)	10	$\sim$0.6	no
V488 Per	Zuckerman et al. (2012); Zuckerman (2015)	90	$\sim$0.06	no

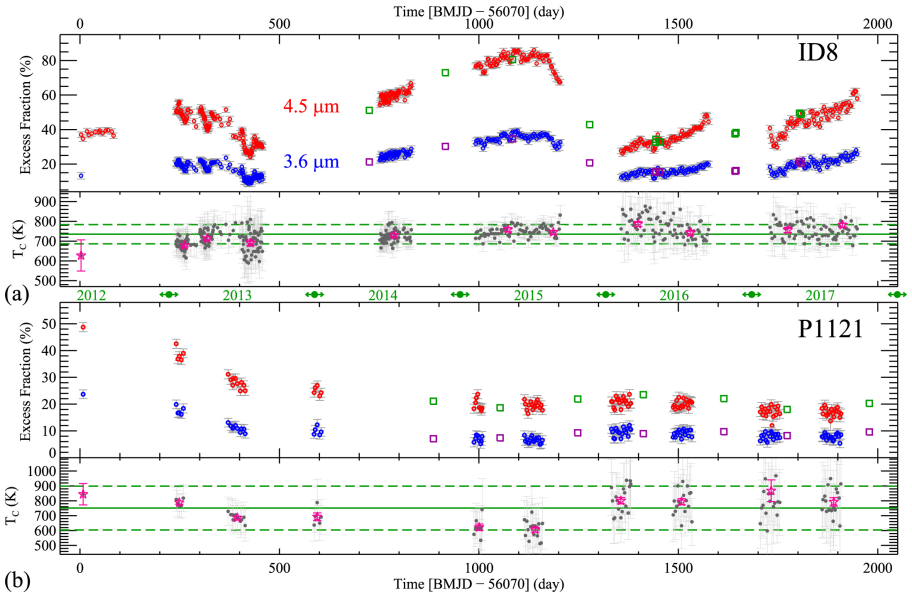

Figure 1.3: The time series excess are shown in the upper panels and the color temperatures are shown in the bottom panels for the systems (a) ID8 and (b) P1121. The open circles are spitzer measurements with red and blue corresponding to 4.5 and 3.6 μm respectively. The squares show measurements from WISE with W1 and W2 being purple and green respectively. The upper panels are excess fluxes relative to the stellar photosphere. Figure 1 from Su et al. (2019).

also two distinct examples of short-term modulations. In 2013 there were two intermixed periodicities found with periods of 26 and 33 days. These periods are too short when the debris location is inferred from SED models. A model in Olofsson et al. (2012) puts the position of the disk between 0.32 and 0.64 au away from the star which corresponds with a period range of 66 to 187 days. The contention can be resolved via an optically thick cloud being sheared along an orbit that is viewed edge-on. The cloud is elongated in the orbital direction and so at the disk ansa the cloud is viewed with the smallest extent. Therefore, as the dust passes through the disk ansa we would see dips in the lightcurve every half an orbit.

Dips in the lightcurve can also be caused by the dynamics of the debris if the debris is produced in a giant impact like event. The site of the giant impact, known as the collision point, sets the point in space where all the ejecta from the impact is produced. As the ejecta is formed in the same place, all particles that form the ejecta share the collision point as a node in orbital plane which all the ejecta must pass through. The debris then must share a line of nodes on the other side of the star to the collision point, known as the anti-collision line, where the orbits of the debris cross again (Jackson et al., 2014; Su et al., 2019). As the debris passes through the plane at both the collision point and anti-collision line, these locations act as 'pinch points' in which the physical extent of the debris cloud is smaller. Therefore, we expect to find dips in the lightcurve with a periodicity one half that of the dust cloud. Su et al. (2019) found after modelling the debris evolution with radiative transfer calculations that the largest dips in the lightcurve are associated with the collision point and ant-collision line, and the second largest dips are associated with the disk ansa. The gap between the largest dips found in the 2013 short-term modulation were separated by 54 days suggesting that the optically thick dust cloud orbited with a period of 108 days. This places the 2013 clump at 0.43 au from the star. The dominant periods of 26 ± 1 days and 34 ± 2 days can replicated if the angle between the collision point and the disk ansa is 70°. The 2014 short-term modulation occurred when the flux of the disk was showing an upward trend, while the 2013 case had a downward trend. The modulation period of 10.4 days of the 2014 data suggests that the angle between the collision point and disk ansa was 90°. Therefore the true orbital period is 4 times 10.4 days so 41.6 days. This places the 2014 impact at 0.24 au from the star. This is a lot closer than 0.43 au found for the 2013 impact showing that these two events are separate impacts.

It is thought that the longer term variation within extreme debris disks is caused by the collisional evolution of the dust formed from vapour, with the potential for the disk lifetime to be

extended from the collisional evolution of larger objects formed in a giant impact. For ID8, the flux decline seen in 2013 with the timescale of roughly one year is consistent with a collisional cascade of material ranging from $100\mu\mathrm{m}$ to mm in size. This favours an impact related event as it has been numerically modelled that impact produced vapour plumes will produce the size ranges required (Johnson & Melosh, 2012). Su et al. (2019) showed ID8 had 3 distinct periods with flux variation on yearly timescales. One in 2013 caused by a potential impact event in 2012 with the flux declining. The second in 2014 with a potential impact in late 2013/ early 2014 with the flux increasing then a sharp fall off in 2015. Finally a steady increase in flux from 2015 onwards. While the first two cases have clear short-term modulations, there is no clear periodicity found in the latest case. It has been suggested that the flux increase seen between 2015 and 2017 could be caused by the collisional cascade of a boulder population (Su et al., 2019). A boulder/planetesimal population can be formed in giant impacts from the non-vapourised material. The timescale to produce observable dust from larger boulders/planetesimals is dependent on size, hence it takes more time for the effects of mutual collisions between boulders to be seen in the lightcurve compared to the vapour condensate. While ID8 shows evidence for an extended period of an extremely bright disk it is not known whether a boulder population would be apparent in all systems. We explore boulder populations in chapter 4.

Besides giant impacts, there are other mechanisms that could potentially cause a bright extreme debris disk. One example is an collisional avalanche (Artymowicz, 1997; Grigorieva et al., 2007). In a collisional avalanche, dust is produced through some mechanism inside the inner edge of a debris disk. The dust is blown into the debris disk through radiation pressure. The dust blown into the disk causes an over density, with the fast travelling particles causing erosion and destruction within the disk. A knock-on effect takes place where dust in the disk now starts to collisionally evolve faster resulting in a brighter disk. Numerical modelling has shown that a collisional avalanche can cause a significant brightening in the disk but cannot replicate the sudden drop in excess flux from the disk or the periodic variability seen in some observed extreme debris disks (Thebault & Kral, 2018).

1.4 Giant Impacts

Giant impacts start to occur after the clearing of gas from the protoplanetary disk. The mutual gravitational interactions between giant objects can lead to orbital crossings. Evidence for giant

impacts can be found within our own Solar System. The Earth-Moon system is formed from at least one giant impact, the unusual iron core fraction of Mercury and the tilt of Uranus also suggest giant impacts played a part in their formation. There is also evidence for giant impacts in exoplanet populations: Kepler-107c is nearly twice as dense as Kepler-107b with both planets having near identical radii. The imbalance cannot be explained by the stellar XUV irradiation but is consistent with a giant impact event stripping the silicate mantle of Kepler-107c (Bonomo et al., 2019).

Early numerical planet formation models used perfect merging assumption in impacts to reduce computational time. While these early models were quite successful at replicating our Solar System, perfect merging is not a common occurrence. Giant impacts will have a range of outcomes depending on the energy involved in the impact from perfect mergers to super catastrophic disruption (Leinhardt & Stewart, 2012). The ejecta produced will escape the potential well of the largest remnant forming a circumstellar disk of material.

Giant impacts become the dominant growth mechanism of planetary embryos after the protoplanetary disk transitions to a debris disk while planetesimal impacts go from growth events on average to destructive. The time giant impacts are expected to occur in is the final stages of terrestrial planet formation, 10-200 Myrs after the formation of the central star. Extreme debris disks are mostly found around young stars within the terrestrial planet forming region, though there are a few exceptions. Giant impacts can produce a significant amount of ejecta with a composition that matches what we observe in extreme debris disks. Below I summarise important works in the field of giant impacts and how they are linked to extreme debris disks.

1.4.1 Theoretical Models

In collisions of planetary bodies and planetesimals, there are two separate collision regimes. Material strength is the dominant binding energy of small objects. For larger objects, the dominant binding energy is the object's self gravity. All planetary embryo collisions will fall into self-gravity regime, therefore to liberate material from a planetary object the gravitational binding energy needs to be overcome.

Housen & Holsapple (1990) used dimensional analysis to create a scaling law to predict the minimum specific energy required to remove half the mass of the target. The study was expanded by Leinhardt & Stewart (2012) to look at projectiles of similar size to the target and in giant impacts this can be common. Leinhardt & Stewart (2012) define the centre of mass

specific energy as,

$$Q_R = \frac{0.5\mu v_i^2}{M_{\rm tot}}, \tag{1.8}$$

where $M_{\rm tot}$ is the sum of the projectile ($M_{\rm proj}$) and target ($M_{\rm targ}$) masses, μ is the reduced mass $M_{\rm proj}M_{\rm targ}/M_{\rm tot}$ and v_i is the impact velocity. The R subscript on the specific energy denotes reduced mass. The catastrophic disruption threshold, the specific energy required to remove half the total mass, is then,

$$Q^*_{RD} = \frac{0.5\mu V^{*2}}{M_{tot}}, \tag{1.9}$$

where V^* is the critical impact velocity required to disperse half of the total mass for a given impact. The catastrophic disruption criterion is a function of two components which describe the strength regime and the gravity regime. In the strength regime, Q^*_{RD} decreases with increasing size while in the gravity regime Q^*_{RD} increases with size. The general form of Q^*_{RD} was derived using $\pi-$scaling theory (Housen & Holsapple, 1990),

$$Q^*_{RD} = q_s(S/\rho_1)^{\frac{3\bar{\mu}(\phi+3)}{(2\phi+3)}} R_{C1}^{\frac{9\bar{\mu}}{(3-2\phi)}} V^{*(2-3\mu)} + q_g(\rho_1 G)^{\frac{3\bar{\mu}}{2}} R_{C1}^{3\bar{\mu}} V^{*(2-3\bar{\mu})}, \tag{1.10}$$

where the first term is dominant in the strength regime and the second term is dominant in the gravity regime. The variables are defined as: R_{C1} is the combined radius of the target and projectile masses assuming a density of $\rho_1 \equiv 1000$ kg m^{-3}, q_s and q_g are dimensionless coefficients with values close to 1, S is the material strength measured in units of Pa s$^{3/(\phi+3)}$, ϕ is a measure of the strain-rate dependence of material strength, and $\bar{\mu}$ is a measure of how energy and momentum from the projectile are coupled to the target. In our work we solely focus on impacts that occur overwhelmingly in the gravity regime.

1.4.2 Vaporisation

Many early simulations did not take into account phase changes as part of the giant impact process due to being purely N-body simulations. Vaporisation of material plays a key role in the size and composition distributions. Evidence for such a dichotomy of material between vaporised and melted debris is found from cratering impacts on the Earth and on the Moon. On the Earth, hyper-velocity impacts from large asteroids created and displaced a global layer of material (Johnson & Melosh, 2012, 2014). Impacts produce a shock wave through the target and projectile. Material jumps to a point along the Hugoniot curve and within a giant impact material that is shocked becomes mostly supercritical. The supercritical fluid expands in a adiabatic

fashion rapidly above the impact site. When decompressing, the material falls into one of three states, melt, vapour or a mix of melt and vapour. Material condensing from a vapour state was shocked onto the Hugoniot curve and then followed a adiabat which intersected the melt-vapour coexistence curve from the vapour side. Melt follows adiabats which intersect the coexistence curve from the liquid side. Johnson & Melosh (2012) modelled spherule formation in vapour plumes caused by Chicxulub-like asteroids. They found for a 10 km sized asteroid impacting Earth at $21\,\mathrm{km\,s^{-1}}$ with an impact angle of $45°$, the vapour condensate forms into a distribution of sizes centred on $270\ \mu\mathrm{m}$. This matches the global layer of glassy silicates found in the K/Pg boundary layer. For higher velocity impacts, the mean size of the vapour condensate spherules increased but the distribution remained the same.

To model a giant impact we need a good understanding of the material that is involved. For terrestrial-like planets, the solid component is often made of two materials with the core typically represented with iron and the mantle as rock. In order to understand how the materials change in phase through the impact we need equations of state (EOS). ANEOS (Analytic Equations of State) are one of the most widely used EOS for giant impact modeling (e.g. Carter et al., 2015, 2018; Bonomo et al., 2019; Davies et al., 2020; Denman et al., 2020) which uses analytical expressions that describe the Helmoltz free energy across a wide parameter range of pressures and temperatures. ANEOS is used in work present in this thesis (see section 2.2.1.b)). Rock is often represented with the forsterite ANEOS as there is an abundance of data on the phase changes of forsterite along with the forsterite being olivine rich and olivines dominate the upper crust of the Earth. The current ANEOS has been extended into modelling molecular vapour species (Melosh, 2007) which is sometimes denoted as M-ANEOS.

Giant impacts occur below the stellar nebula pressure, which is approximately where the triple points of silicates lie (Davies et al., 2020). Shocked material in a giant impact will follow the principle Hugoniot becoming supercritical. When no shear strength is present (planetary embryos are dominated by gravitational binding energy), the decompression path is reversible and isentropic. Material is shocked to a specific entropy value, which stays constant as the material starts to decompress. In pressure-specific entropy or temperature-specific entropy space, the material falls past the critical value into the liquid-vapour dome. The material is then a mix of liquid and vapour. It can be assumed that material will decompress until it reaches the triple point temperature at which point it will solidify, though decompressing to a pressure of 1 bar

then measuring the mix of the material can also be assumed for impacts occurring in an Earth-like atmosphere, for example when studying catering impacts in an Earth-like planet (Davies et al., 2020).

Impact velocities need to exceed 6-8 $\mathrm{km\,s^{-1}}$ in order to start vapourising silicates, for ices the vapourising velocity is reduced to $\sim$ $1\mathrm{km\,s^{-1}}$. These values roughly match the escape velocity of Mars-sized objects, hence any collision with objects of this size or larger will be approaching the vaporisation regime (Davies et al., 2020). An impact between two planetary embryos involves a transfer of energy between the potential, kinetic, and internal energies of the material. Moon-forming events have been shown to widely differ in terms of the outcomes when considering the state of the material, and the canonical Moon-forming impact is a relatively low-energy event (Carter et al., 2020). An example of a non-canonical Moon forming impact is an impact with high energy and high angular momentum which creates a post-impact structure that exceeds the corotation limit known as a synestia. A synestia can explain the composition and isotopic similarity between the Earth and the Moon through the vapourisation of silicate and then mixing between proto-Earth and impactor mantles (Lock et al., 2018).

1.5 Outline

The focus of my thesis is on understanding how giant impacts form and influence the behaviour seen in extreme debris disks. In chapter 2 I outline the SPH and N-body codes used to conduct simulations of giant impacts and extreme debris disks. It will also summarise the radiative transfer code used to estimate what our simulated disks looked like and any other analytical processes I undertook. In chapter 3 I discuss the vapourisation of ejecta material and how that can form an initially bright disk with variable behaviour. Chapter 4 focuses on the boulder population that potentially forms in giant impacts and how that could sustain an extreme debris disk. Chapter 5 summarises the work discussed in this thesis and future work that will extend on the topics covered.

2

Numerical Methods

2.1 Introduction

Observations offer us snapshots into the many Myr process of planet formation. Extreme debris disks are different to traditional debris disks in that they have been observed to show behaviour change which is observable on yearly and monthly timescales. Though as extreme debris disks sit close to their star, they cannot be spatially resolved. To understand the behaviour of extreme debris disks we set out a numerical campaign to explore their formation and evolution through giant impacts. The three part campaign looks at the initial giant impacts using smoothed particle hyrdrodynamical code (SPH) GADGET-2 (Springel, 2005), then the formation and evolution of the debris disk using two different N-body codes one which was built by me and the second Rebound (Rein & Liu, 2012), and finally the lightcurves of the evolving disks are estimated using radiative transfer code RADMC3D (Dullemond et al., 2012).

2.2 Smoothed Particle Hydrodynamical code: GADGET-2

2.2.1 Theory

Smoothed particle hydrodynamics (SPH) is a mesh-free method of modelling fluids. The continuous system can be represented by a series of discrete particles which independently hold information on the state of the fluid. A Lagrangian is used to evolve the fluid equations. For our use case it allows us to track pressure, temperature and entropy of material over time. Particles are carried along flows and the hydrodynamic and other properties are then calculated at the

particle positions. The properties of a particle are calculated from a weighted average of other local particles, hence properties are smoothed over a finite volume of masses. The averaging of particles must be done using a smoothing Kernel W which must have a characteristic width h known as the smoothing length. The choice of W is important as it must meet a set of criteria: it must tend to a $\delta-$function as h tends to zero, needs to have a well defined derivative, and must be spherically symmetric so it only depends on r and h where r is the distance between two particles. As we can assume long range forces are negligible, we can set a condition that $W(r,h) = 0$ for $r/h > k$ for some constant k. The scaling of computational cost is then $\mathcal{O}(NN_{\rm neigh})$, where $N_{\rm neigh}$ is the number of neighbour particles within a sphere of radius $r = kh$. For GADGET-2, the Kernel used is

$$W(r,h) = \frac{8}{\pi h^3}\begin{cases} 1 - \frac{3}{2}x^2 + \frac{3}{4}x^3 & 0 \leq x \leq \frac{1}{2} \\ 2(1-x)^3 & \frac{1}{2} \leq x \leq 1 \\ 0 & x > 1 \end{cases} \tag{2.1}$$

where $x = r/h$. The smoothing lengths for each particle i, h_i, are determined by

$$\frac{4\pi}{3} h_i^3 \rho_i^{\rm sv} = N_{\rm neigh}\bar{m} = M_{\rm sv}, \tag{2.2}$$

where $\rho_i^{\rm sv}$ is the density inside the smoothing volume, $N_{\rm neigh}$ is the number of smoothing neighbours, $\bar{m}$ is the average mass per particle and $M_{\rm sv}$ is the mass within the smoothing volume. The mass contained within the smoothing volume remains constant in GADGET-2, hence the smoothing length will vary for each particle. The density estimate for each particle in GADGET-2 is calculated from

$$\rho_i = \sum_{j=1}^{N} m_j W(|\boldsymbol{r}_{ij}|, h_i), \tag{2.3}$$

where $\boldsymbol{r}_{ij} \equiv \boldsymbol{r}_i - \boldsymbol{r}_j$. Both the estimates for density and smoothing length must obey the condition set in equation 2.2.

With the above in mind, we can now construct the Lagrangian which will be in the form $L = T - V$, where T is the kinetic energy and V is the potential energy of the system. For GADGET-2, the Lagrangian is

$$L(\boldsymbol{q}, \dot{\boldsymbol{q}}) = \frac{1}{2}\sum_{i=1}^{N} m_i \dot{r}_i^2 - \frac{1}{1-\gamma}\sum_{i=1}^{N} m_i A_i \rho_i^{\gamma-1} \tag{2.4}$$

where $\boldsymbol{q} = (\boldsymbol{r_1}, ..., \boldsymbol{r_N}, h_1, ..., h_N)$. In a difference from standard SPH practice, GADGET-2 uses a pseudo-entropy term $A(s)$ instead of internal energy u as an independent variable. The

entropic function is defined as

$$P = A(s)\rho^{\gamma}, \tag{2.5}$$

where γ is the adiabatic index and A is dependent on the specific entropy s. Equation 2.2 gives us the holonomic constraints such that

$$\phi_i(\boldsymbol{q}) \equiv \frac{4\pi}{3} h_i^3 \rho_i - M_{\rm sph} = 0. \tag{2.6}$$

Now the equations of motion can be obtained via the Lagrange equations of the first kind. From which we find the equations of motion to be,

$$\frac{d\boldsymbol{v}_i}{dt} = -\sum_{j=1}^{N} m_j \left[f_i \frac{P_i}{\rho_i^2} \nabla_i W_{ij}(h_i) + f_j \frac{P_j}{\rho_j^2} \nabla_i W_{ij}(h_j) \right], \tag{2.7}$$

where f_i is defined as

$$f_i = \left(1 + \frac{h_i}{3\rho_i} \frac{\partial \rho_i}{\partial h_i} \right)^{-1}, \tag{2.8}$$

and $W_{ij}(h_i) = W(|\boldsymbol{r}_i - \boldsymbol{r}_j|, h_i)$. The equations above define a reversible fluid in SPH if there are no shocks or external sources of heat. For such a flow, A remains constant.

The above describes a polytropic flow, so does not capture the transfer of mechanical energy into heat energy correctly in transonic and supersonic flows. The issue is at a shock front, the properties of the flow, such as velocity, pressure, density and entropy, change very rapidly. These changes appear to be discontinuities on larger scales. In order to capture shocks within SPH, an artificial viscosity is needed. To account for viscosity, GADGET-2 uses a viscous force

$$\left. \frac{d\boldsymbol{v}_i}{dt} \right|_{\rm visc} = -\sum_{j=1}^{N} m_j \Pi_{ij} \nabla_i \overline{W}_{ij}, \tag{2.9}$$

where $\overline{W}_{ij}$ is the mean of the kernels for particles i and j such that $\overline{W}_{ij} = [W_{ij}(h_i) + W_{ij}(h_j)]/2$, and Π_{ij} is a tensor term which describes the strength of the artificial viscosity. GADGET-2 uses a slightly modified parametrisation of the viscosity from Monaghan (1997)

$$\Pi_{ij} = -\frac{\alpha}{2} \frac{\nu_{ij}^{\rm sig} \omega_{ij}}{\rho_{ij}}, \tag{2.10}$$

where $\nu_{ij}^{\rm sig}$ is the signal velocity and ρ_{ij} is the mean density between particles i and j. Here the signal velocity, $\nu^{\rm sig}$ can be estimated as

$$\nu_{ij}^{\rm sig} = c_i + c_j - 3\omega_{ij}, \tag{2.11}$$

where c_i is the sound speed at particle i and w_{ij} follows the condition

$$\omega_{ij} = \begin{cases} \frac{\boldsymbol{v}_{ij} \cdot \boldsymbol{r}_{ij}}{|\boldsymbol{r}_{ij}|} & \boldsymbol{v}_{ij} \cdot \boldsymbol{r}_{ij} < 0 \\ 0 & \text{otherwise} \end{cases}. \tag{2.12}$$

The sound speed for each particle is given by the equation of state that defines what material each particle represents. A detailed discussion on the equation of states used are in section 2.2.1b). We now move onto discuss how gravitational interactions are determined in the code.

a) Gravitational Algorithms

The particle nature of SPH code allows for N-body methods of solving for gravitational forces. A simple method would be a brute force calculation of the gravitational interaction between a particle and all the other particles, for all particles. This would become computationally expensive for a large amount of particles as the time would scale as $\mathcal{O}(N^2)$. GADGET-2 adopts a hybrid method called TreePM to calculate gravitational forces. TreePM allows the estimation of short range interactions to be determined from a hierarchical tree while long range interactions are determined from a particle mesh method. The split between short and long range interactions is determined from a set value r_s which spatial scale of the force split. In essence r_s sets the scale at which the tree is walked. The hybrid method takes advantage of the $\mathcal{O}(NlogN)$ scaling of hierarchical tree methods while keeping accuracy of long range forces from particle mesh methods. However, for our use case in simulating giant impacts we solely use the hierarchical tree method to calculate the gravitational forces as we are only interested in short-range interactions between particles within planetary bodies.

GADGET-2 uses the oct-tree method to build the hierarchical tree, the method is shown in Fig. 2.1. The total volume is repeatedly subdivided into 8 daughter nodes of equal length until each node only contains a single particle, these are known as 'leaf' nodes. The force on a particle is then estimated by walking the tree. To walk the tree, the top nodes will be tested against a set of opening criteria. The opening criteria determines the accuracy of the force calculation. If the node meets the opening criteria then an approximation of the force from all particles within the node can be used. Otherwise if the criteria is not met then the walk must proceed into the daughter nodes. The process repeats until the opening criteria is met or there are no more daughter nodes to move into. Hence, the gravitational force acting upon a particle i will be a summation of the force from each node that does not meet the opening criteria. For nodes that

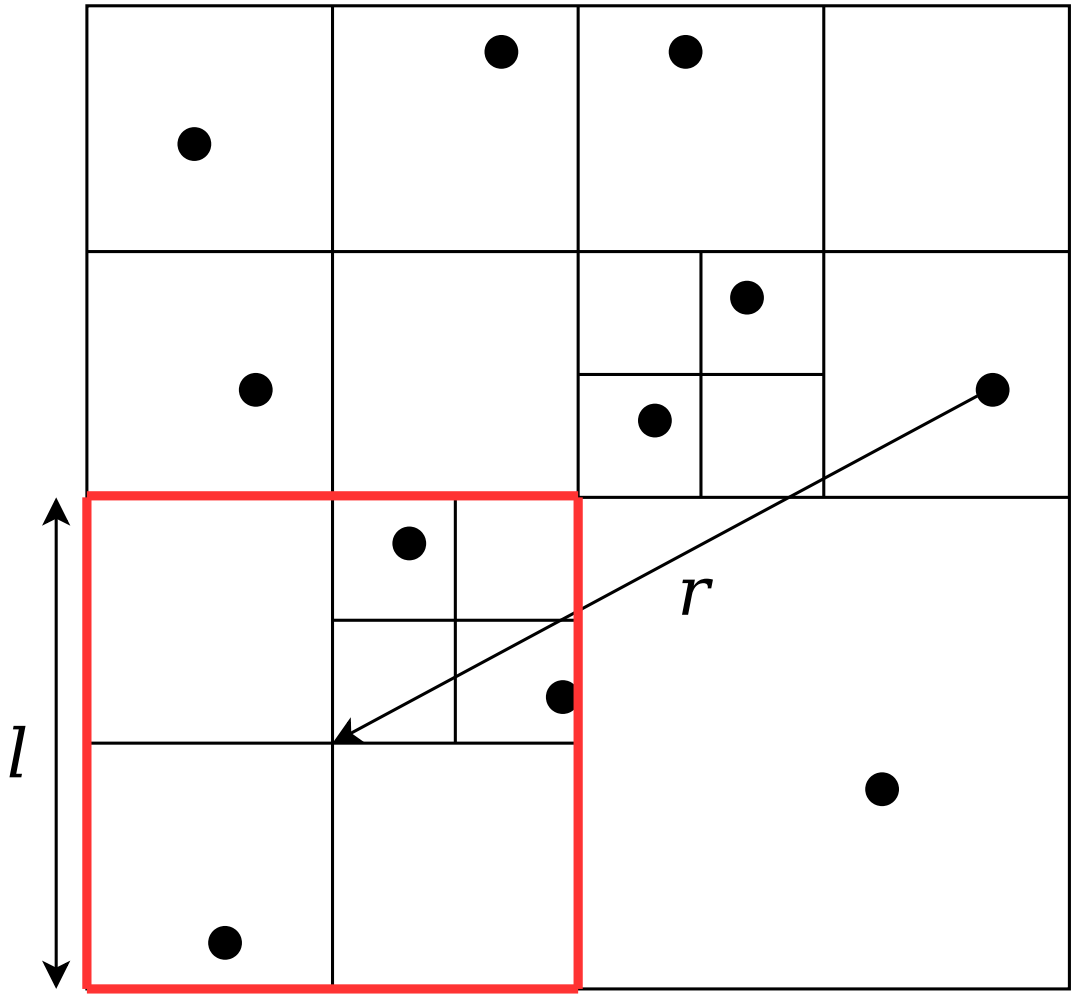

Figure 2.1: Diagram of the oct-tree used to determine gravitational forces in GADGET-2. Starting with an initial box, the box is split into 8 equal sized sub boxes. This repeats for each box until a box either contains one or zero particles. A particle with a distance r to the red box with extent l will be tested against the opening conditions stated in equations 2.13 and 2.14.

sit close to particle i, these will only contain a single particle so these particles are considered in full when calculating the force on particle i. Nodes further away will have multiple particles associated with them and hence an approximation is used where the distance to centre of mass of the node and the total mass in the node is used to calculate the force on particle i.

For GADGET-2, there are two sets of opening criteria. The first has to meet

$$\frac{GM}{r^2}\left(\frac{l}{r}\right)^2 \leq \alpha|\boldsymbol{a}|, \tag{2.13}$$

where M is the node mass, l is the extension of the node, r is the distance to the node, $|\boldsymbol{a}|$ is the total acceleration obtained in the last time step and α is a tolerance parameter. This criteria is chosen to keep the relative force error between particles roughly constant over the course of the simulation. Errors can become unbound at extremely small distances though, hence a second opening criteria is chosen,

$$|r_k - d_k| \geq 0.6l, \tag{2.14}$$

where $\boldsymbol{d} = (d_1, d_2, d_3)$ is the geometric centre of the node, $\boldsymbol{r}$ is the particle coordinate and the condition applies for each coordinate axis $k \in \{1, 2, 3\}$. Hence, equation 2.14 requires that the particles lies outside a box which is at least 20% larger than the tree node.

b) Tabulated Equations of State

The release version of GADGET-2 lacked the equations of state needed in order to model planetary embryos. The equations of state are complicated hence GADGET-2 was modified to use tabulated equations of state (details can be found in Marcus et al., 2009; Ćuk & Stewart, 2012). The model planetary embryos used iron and forsterite for the core and mantle respectively, with the equations of state being derived from ANEOS/MANEOS models (Melosh, 2007). Grids of tabulated values were generated from the models so when a value was needed it was interpolated from the grid. In order to resolve phase boundaries, the tables needed to be finely grided. This method was much quicker than calling on the model every time a value was needed. The tabulated ANEOS dataset can be found in Carter et al. (2019a).

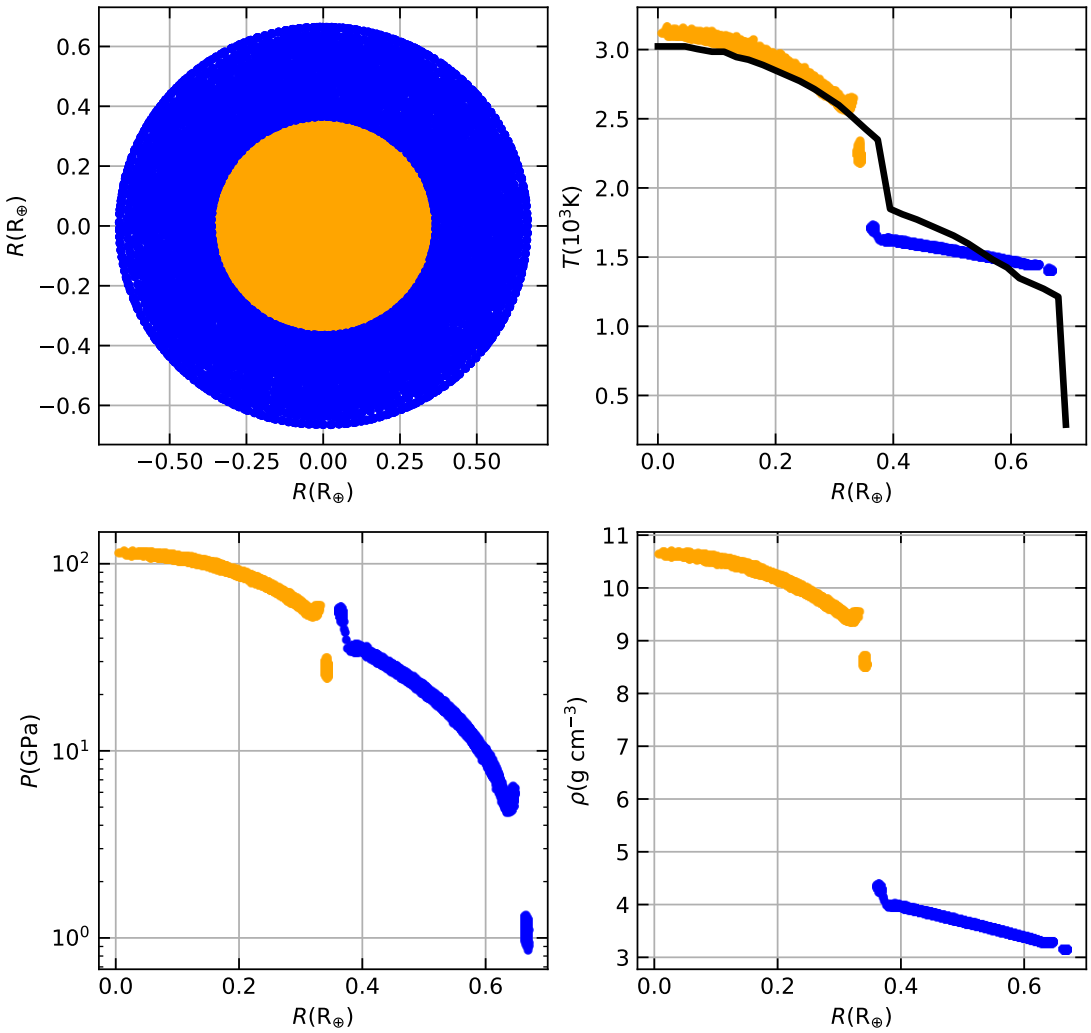

Figure 2.2: Example of an initialised and equilibrated planet with mass of 0.25 $M_\oplus$ and containing 285715 particles. Top left is a central slice of the completed initialisation. The rest of the plots are radius profiles of: temperature (top right), pressure (bottom left), and density (bottom right). Along with temperature is the initial temperature-radius profile provided in black. The colours represent the material used, with iron and forsterite being orange and blue respectively.

2.2.2 Simulation Setup

a) Planetary Embryo Formation

In order to set up a collision in GADGET-2, we need to form the individual planetary embryos. To model a planetary embryo, we need a starting point. We use tabulated temperature-radius profiles determined for Super-Earths from Fig. 4 of Valencia et al. (2006). From these tables we can scale from a given profile to create a profile for any size using the relations $T \propto M^{0.162}$ and $R \propto M^{0.263}$, where M and R are the mass and radius of the planetary embryo. The radial profiles are an initial input into our set-up code which also requires the number of particles, radii for the core and mantle surfaces, and estimated bulk density for each material. We do not change the materials or the estimated bulk densities between generated planetary embryos. We use iron and forsterite as core and mantle materials with bulk densities of $8\ \mathrm{g\ cm^{-3}}$ and $3\ \mathrm{g\ cm^{-3}}$ respectively. The core and mantle radii are determined from the temperature-radius profile. We vary the number of particle used in the planetary embryos from $\sim 10^4$ to $\sim 3 \times 10^5$.

From the bulk density estimates, an iterative process is used to generate a full density profile. The cumulative mass and gravity radial profiles are generated using the density estimates from the inside out. From the mass and density profiles, a pressure profile is generated from outside in. From the pressure and temperature radial profiles along with the equations of state a density profile is generated. The process is repeated with the new density profile until it no longer changes. Once the radial profiles have been obtained, the object can be split into radial shells. Particles are randomly placed in the radial shells, the number in each shell is dependent on the volume of the shell and the density at that point. The composition of the particles is determined by the shell location. All particles are set to have the same mass.

b) Equilibration

The random placement of particles in shells means that when we come to running a SPH simulation there maybe instabilities caused by overdensities or underdensities within the planetary embryo. An example of an equilibrated planet is shown in Fig.2.2. The instabilities caused by the random placement of particles mean particles will oscillate around a local minima, hence the planet looks like it is ”breathing”. Also, as the planetary embryo is not in a settled state the specific entropy of particles tends to increase with time causing nonphysical values. In order to correct for this we do an equilibration step for each planetary embryo before running an impact

simulation. To speed up the time for stabilisation we use two cooling methods, velocity damping and entropy forcing. Velocity damping is an applied multiplicative restitution factor to the velocities of each particle. The dampening of the velocities reduces the time it takes for particles to equalise to their final position in the planetary embryo from the initial placement in a shell. For the entropy forcing, the entropy of each particle was set to a constant value which depended on the material type. The values used for iron and forsterite were varied for each planetary embryo so the final temperature-radius profile approximately matched the input profile.

To check whether the planetary embryos had reached a stable equilibrium we checked the velocities, radius and bulk density. At equilibrium there is no bulk velocity attributed to a planetary embryo. At each time step a radius and bulk density were calculated. Both values over time will settle with equilibrium being determined when the rate of change of radius and bulk density reached a threshold value of 0.1%.

c) Collision Setup

A giant impact is defined by a few parameters: impact parameter b (0 to 0.8), impact velocity $v_{\rm imp}$ ($\sim$ 6 to $\sim$ 40 km s^{-1}), mass ratio γ (0.1 to 1) and the total mass $M_{\rm tot}$ ($\sim$ 0.2 to $\sim$ 2M$_\oplus$). Figure 2.3 shows a diagram of a typical giant impact, here $B = b(R_{\rm p} + R_{\rm t})$ where $R_{\rm p}$ and $R_{\rm t}$, are the radii of the projectile and target planetary embryos respectively. In the set up, the projectile and target were given a separation of between 1.1 and a few mutual radii. Small separations were chosen to keep the desired collision parameters. A large separation allows the for the gravitational interactions between the objects to change the point of collision. Larger separations need input values which need to be solved for in order to get the desired impact. Some collisions had a larger separation to test for tidal forces. The simulation run time was set so that the ratio between the gravitational dynamical time, $t_{\rm dyn}$, and the simulation time, t, was $t/t_{\rm dyn} > 10$. The gravitational dynamical time is an estimate for the time needed for gravitational resettling to occur and is defined as

$$t_{\rm dyn} = \sqrt{\frac{R^3}{GM_{\rm tot}}} \tag{2.15}$$

where $M_{\rm tot}$ is the total mass in the system and R is the initial separation set in the simulation. The 10 $t_{\rm dyn}$ time is sufficient for the mass of each bound remnant to stabilise.

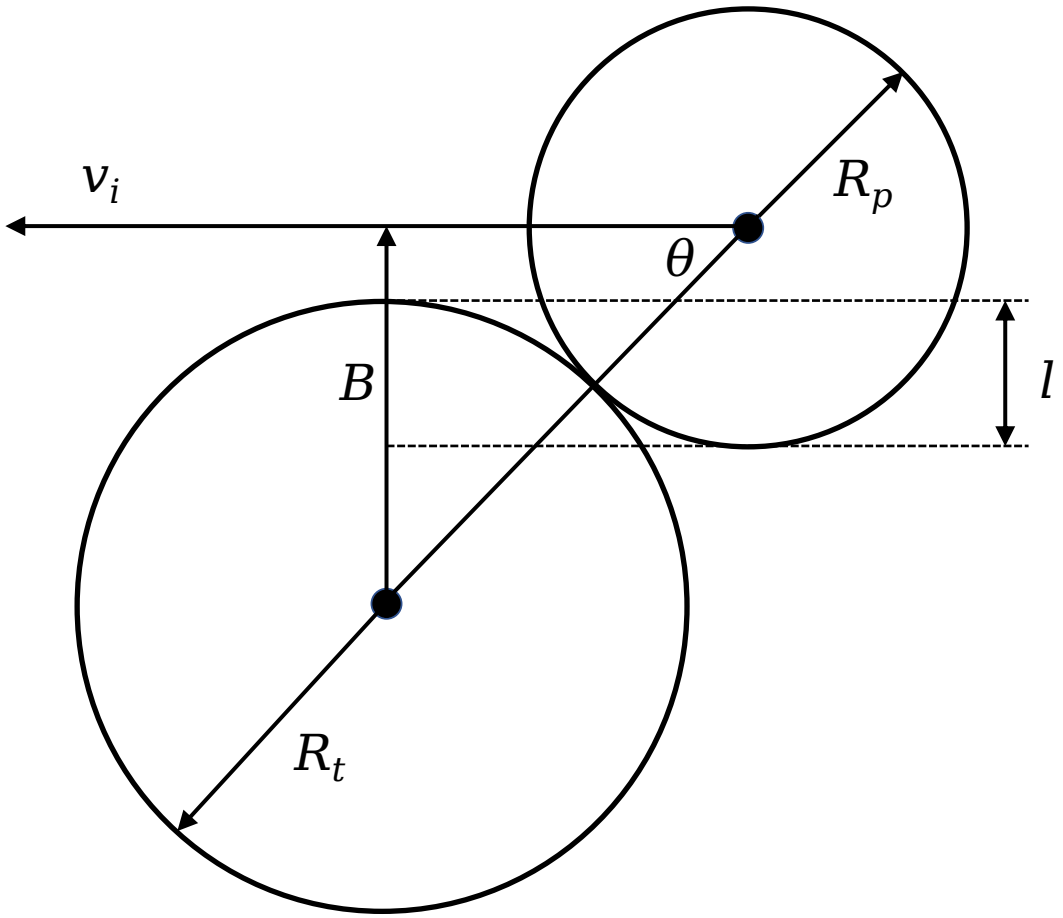

Figure 2.3: A diagram of an impact between two planetary embryos with the parameters used to describe them. Here v_i is the impact velocity, l is the interacting mass, θ is the impact angle, and $B = b(R_t + R_p)$ where $b = \sin\theta$ is the impact parameter.

2.2.3 Analysis Tools

a) Remnant Finder

To find the number and mass of bound objects and the unbound ejecta we used an iterative process that determined what particles are gravitationally bound together to form a remnant. The process begins with finding a seed particle. The seed particle is defined as the particle with the minimum potential energy when compared to all other particles,

$$V_j = -\sum_{i \neq j}^{N} \frac{G m_i m_j}{|\boldsymbol{r}_j - \boldsymbol{r}_i|}, \tag{2.16}$$

where V_j is the potential energy of particle j, m_i and m_j are the masses of particles i and j, $|\boldsymbol{r}_j - \boldsymbol{r}_i|$ is the distance between particles, and N is the number of particles in the simulation. The seed particle has the smallest V. Once a seed particle is chosen, other particles are then added to build up the remnant if

$$E_\mathrm{k} + E_\mathrm{p} < 0, \tag{2.17}$$

where E_k is

$$E_\mathrm{k} = \frac{1}{2} m_i v'^2 \tag{2.18}$$

and E_p is

$$E_\mathrm{p} = -\frac{G M_\mathrm{b} m_i}{r'}. \tag{2.19}$$

Here E_k and E_p are the kinetic and potential energies respectively for particle i in a reference frame centred on the remnant, with M_b being the remnant mass, $r' = |\boldsymbol{r}_i - \boldsymbol{r}_\mathrm{b}|$ and $v' = |\boldsymbol{v}_i - \boldsymbol{v}_\mathrm{b}|$; where $\boldsymbol{r}_\mathrm{b}$ and $\boldsymbol{v}_\mathrm{b}$ are the position and velocity vectors of the remnant. The process is iterated until the mass within the remnant stabilised. The process is repeated by selecting a new seed particle that is not part of a defined remnant. This continues until all remnants are found. In order to be defined as a remnant, the remnants need to meet a minimum number of particles associated with them. We did change this criteria between studies. We either set the minimum number at 5 particles or 500 particles. Any particles that did not meet this threshold were treated as unbound. The change in criteria would have had a negligible effect on what was concluded in chapter 3 as the mass change in the escaping vapour fraction would have been minimal. For 4 it was necessary to set a lower threshold to attempt to establish the larger mass planetesimals in the distribution. A 500 particle limit would have lead to very few planetesimals being resolved.

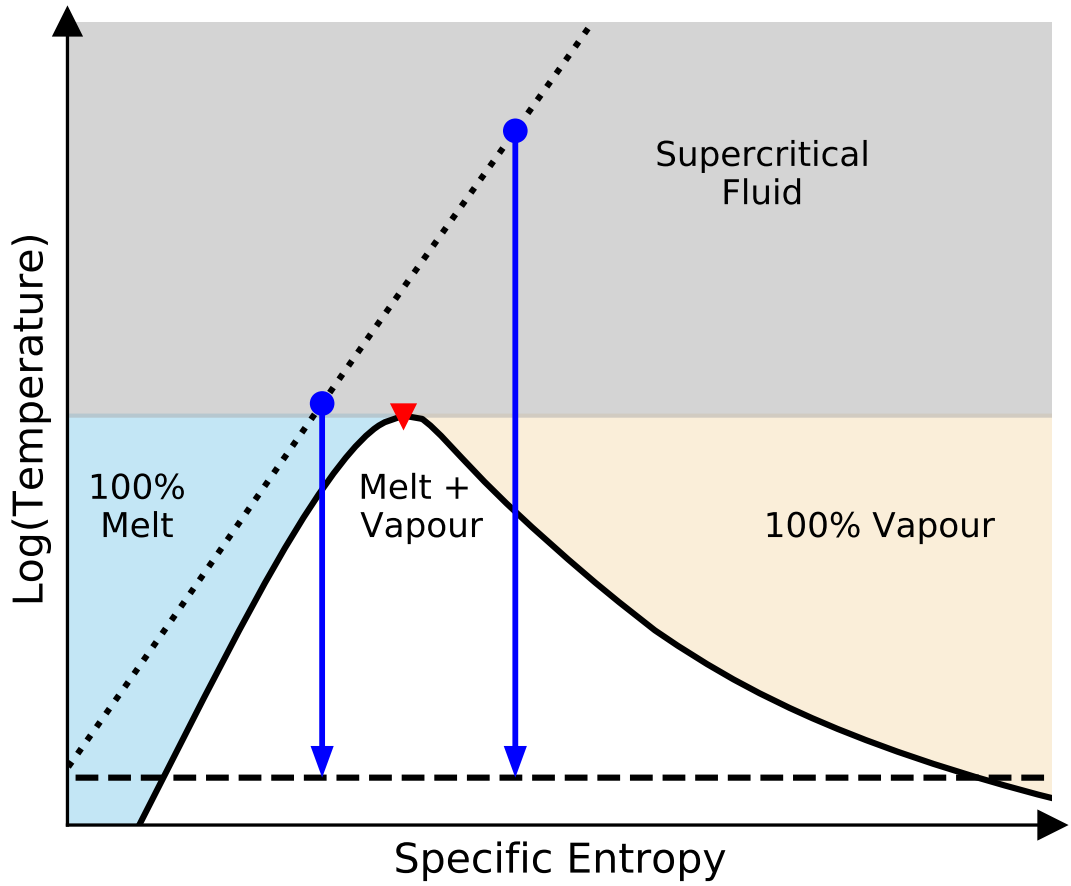

Figure 2.4: An example vapour dome from which vapour fraction of particles is determined. The solid line represents the phase boundary, the dotted line is the Hugoniot and the dashed line indicates the triple point temperature. The red triangle indicates the critical point which is the transition point from a supercritical fluid state. The blue dots indicate points along the Hugoniot with the blue arrows showing the resulting position of the blue dots on the triple point line after isentropically cooling. Vapour fraction is determined from where particles fall on the triple point line.

b) Vapour Fraction

A collision with sufficient energy will produce a shock through the colliding material. Shocked material jumps to a point on a Hugoniot curve, increasing in temperature, pressure and entropy. Vaporised and non-vaporised material will condense into different sized objects (Johnson & Melosh, 2012, 2014). In order to track these differences we need to know the state which each particle is in. We assume that all material cools isentropically from the Hugoniot curve when the shock has finished propagating. The particles will cool from a supercritical state into a pure melt state, a pure vapour state or into a vapour dome in which the particle will be a mixture of melt and vapour. Figure 2.4 shows an example vapour dome in log(temperature)-specific entropy space. The vapour dome for each material is determined from ANEOS. We assume all particles will condense at the triple point temperature, hence we measure the mix of liquid-vapour mix at the triple point temperature. The triple point temperature is $1890°\mathrm{C}$ and $2970°\mathrm{C}$ for forsterite (Nagahara et al., 1994) and iron (Liu, 1975) respectively. To evaluate the liquid-vapour mix we use a vapour dome in temperature-specific entropy space and the lever rule to find the vapour fraction which is defined as

$$f_{\mathrm{v}} = \frac{w - w_l}{w_v - w_l}, \tag{2.20}$$

where w is the specific entropy of a SPH particle, w_l is the specific entropy of the phase boundary between liquid and liquid+vapour at the triple point temperature, and w_v is the specific entropy of the liquid+vapour and vapour phase boundary.

2.3 N-body code

2.3.1 Multistep N-body

a) Particle Properties

In the SPH giant impact simulations, the number of particles classed as unbound tended to be only a small fraction of the total mass. We varied the resolution of the SPH simulations between 4×10^4 and 4×10^5. Hence the total number of unbound particles will vary with the resolution and collision parameters. If we spatially evolve the unbound material with a low particle number, the disk that forms will not track the true distribution. This is because each SPH particle contains a large amount of mass that will form multiple objects. For the vapour portion of each particle, we assume that grains form with sizes between cm and $\mu\mathrm{m}$. The

distribution of unbound particles needs to be smoothed out to fully track the spatial evolution of small grains. We, therefore, upscale the particle resolution to approximately 10^5 particles before simulating the spatial evolution in the N-body code. An approximate value is used here because the upscale method generates n particles per original particle. The number of particles that were to be generated was calculated by $10^5/N_{\rm sph}$, where $N_{\rm sph}$ is the number of escaping particles in the SPH simulation. As $10^5/N_{\rm sph}$ was not always an integer, we rounded to the nearest integer leading to the approximate number of particles upscaled. To generate the upscaled population we use the distribution of escaping particles from the final snapshot in each SPH simulation.

So n particles are generated around SPH particle i in a volume defined by the 5^{th} closest SPH neighbour. We chose the 5^{th} closest as within dense regions the local properties are represented around particle i for the upscaled particles as well as allowing the less dense particles to be smoothed out. All generated particles are given spatial coordinates defined by where they were generated around each original escaping particle. Next we need to assign velocities. The velocities are generated from a weighted average of the five closest SPH particles. The weights used are inverse distance weighted such that

$$w_i(\boldsymbol{x}) = \frac{1}{d(\boldsymbol{x}, \boldsymbol{x}_i)^p}, \tag{2.21}$$

where d is the distance between the two particles, $\boldsymbol{x}$ is the position generated particle and $\boldsymbol{x}_i$ is the position of the ith closest SPH particle. We choose $p = 3$ so the velocity is not smoothed over a wide volume. The overall velocty for the generated particle is then,

$$\boldsymbol{v} = \frac{\sum_i w_i \boldsymbol{v}_i}{\sum_i w_i}. \tag{2.22}$$

Mass for each particle is set as the total mass of escaping vapour, $M_{\rm vap}$, divided by the number of upscaled particles. After the particles have been generated, the distribution is centred on the location in which the giant impact took place around the star. The bulk velocity given to the generated particles will be equal to the progenitor orbit at the moment of impact. The velocities given to the generated particles will act as an velocity kick on the bulk velocity. The distribution of particles is also given an orientation around the z-axis. The orientations are shown in Fig. 2.5. The orientation changes the direction of the velocity kick for each particle. We choose orientation values of 0 and $\pi/2$ as these values coincide with the giant impact happening parallel to the orbital direction of the progenitor and perpendicular to the orbital direction respectively.

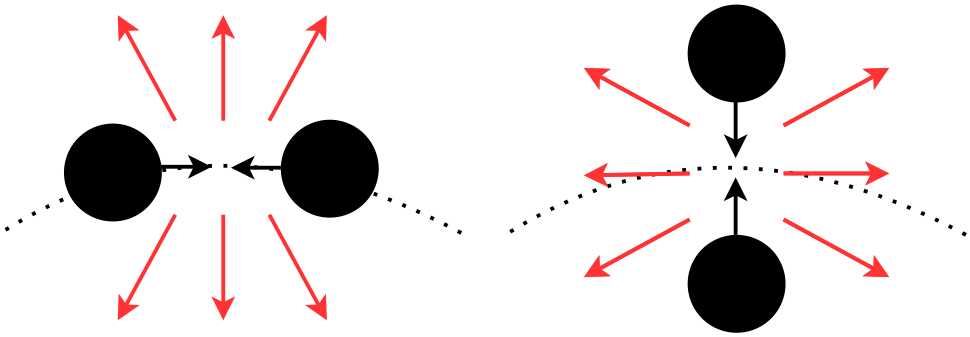

Figure 2.5: Diagram showing the two orientations used for giant impacts with respect to the progenitor orbit (dashed line). The orientations are shown for an example collision of a head-on impact being orientated 0° (left) and 90° (right) to the centre of mass orbit. The red arrows indicate the likely direction of ejecta.

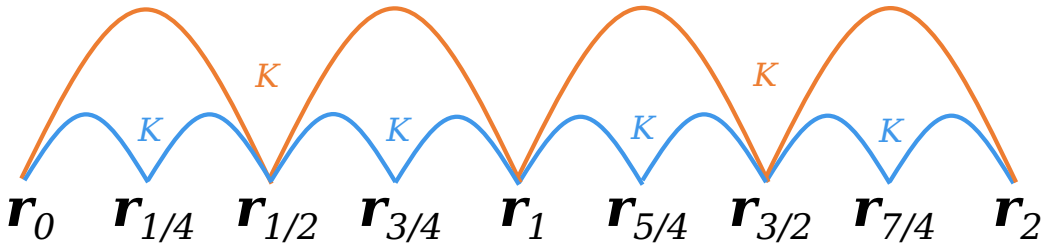

Figure 2.6: Diagram of the drift-kick-drift regime of leapfrog. It shows how a particle with an initial position $\boldsymbol{r}_0$ progresses with time. The lines show the drift of the particle between time steps. The orange lines represent the initial time step while the blue shows a subdivision of the time step, with K representing when the velocity updates occur.

b) Leapfrog Integrator

All dust particles in the N-body code are effectively massless as we assume their mass is small enough to ignore mutual gravitational interactions. The dust particles interact gravitationally with the central potential well which defines the star and designated "planet" particles which are the two largest remnants identified from the SPH simulation. The "planet" particles interact gravitationally with each other and the central potential well. As there are only a few bodies gravitationally active, gravitational force calculations are directly carried out for all particles.

The integrator uses the gravitational force calculations to solve for the equation of motion for all particles. We choose to use a second order leapfrog integrator. Leapfrog has the desired qualities of being sympletic and time-reversable when a constant time step is used. It is easily adaptable to have a variable time step as well. The leapfrog integrator is written as

$$\begin{aligned} \boldsymbol{r}_{i+1} &= \boldsymbol{r}_i + \boldsymbol{v}_{i+1/2}\delta t \\ \boldsymbol{v}_{i+3/2} &= \boldsymbol{v}_{i+1/2} + \boldsymbol{a}_{i+1}\delta t, \end{aligned} \tag{2.23}$$

where δt is the time step, $\boldsymbol{r}$ is the position vector, $\boldsymbol{v}$ is the velocity and $\boldsymbol{a}$ is the acceleration given to a particle. The acceleration is calculated by

$$\boldsymbol{a}(\boldsymbol{r}_i) = \frac{\boldsymbol{F}_i}{m_i}, \tag{2.24}$$

where $\boldsymbol{F}_i$ and m_i are the force acting on and mass of particle i respectfully. Typically, leapfrog integrators are not self starting with the first velocity kick needing to be found by some other means. For us the first kick is defined by the escape velocities of the escaping material in the SPH giant impact simulations meaning we do not have to solve for $\boldsymbol{v}_{1/2}$ by other means.

In equation 2.23 we have assumed we will update the position vector then a half step later the velocity vector. This is known as the drift-kick (DK) version of the leapfrog integrator. For the multistep N-body code, we use a drift-kick-drift (DKD) version. DKD allows for the synchronisation of the particle position and velocity. Fig. 2.6 shows a diagram of how DKD works. DKD takes the form

$$\begin{aligned} \boldsymbol{r}_{i+1/2} &= \boldsymbol{r}_i + \frac{1}{2}\boldsymbol{v}_n\delta t \\ \boldsymbol{v}_{i+1} &= \boldsymbol{v}_i + \boldsymbol{a}_{i+1/2}\delta t \\ \boldsymbol{r}_{i+1} &= \boldsymbol{r}_{i+1/2} + \frac{1}{2}\boldsymbol{v}_{i+1}\delta t. \end{aligned} \tag{2.25}$$

Adaptive stepping is used to resolve close encounters between a particle and a gravitating body. While it resolves the issue of potentially nonphysical acceleration of particles, using

adaptive stepping means the integrator is no longer sympletic. For long integrations the orbits can drift away from the true orbit as the energy is no longer bound. Our focus is on the early spatial evolution of vapour condensate post-giant impact, so long integrations are not a worry. Particles are selected for adaptive stepping if the time step t they are assigned falls into the criteria of $t > P_*/20$ or $t > P_{\rm rem}$ where P is the period it takes to orbit an object, i.e. the time step is required to take at least 20 steps in order to orbit the star/remnant if it was on a circular orbit at its current location. A particle only checks if $t > P_{\rm rem}$ if the particle is inside one hill radius of the remnant. All particles start with a time step of $t = P_*/2000$ with P_* being determined by the location of the impact.

c) Gravity

The velocity update depends on the acceleration the particle is under. In all simulations, particles undergo acceleration via gravitational interactions with the star and any remnants. The acceleration is calculated,

$$\boldsymbol{a}_i = G\left(\frac{M_*}{r^2} + \sum_{j=0}^{N_{\rm rem}} \frac{m_j}{r_{ji}^2}\right) \tag{2.26}$$

where G is the gravitational constant, r is the distance from the origin (where the star is located), M_* is the stellar mass, m_j is the mass of remnant j and $\boldsymbol{r}_{ji} = \boldsymbol{r}_j - \boldsymbol{r}_i$ is the relative distance between remnant j and particle i. We limit the number of remnants in all simulations to 2 as the majority of the mass will be within the two largest bodies, and hence any gravitational interactions will be dominated by these two objects. Therefore all gravitational calculations are brute forced as it will only scale with the number of particles on order $O(3N)$. The remnants do gravitationally interact with one another, to account for the inter-remnant interactions the number of remnants summed over is reduced by one in eqn. 2.26.

d) Removal of Particles

To be physical, we allow the remnants within the disk to reaccrete material even though on the timescale we are focused on it will not be an efficient removal method. The particles have to meet two conditions in order to be accreted; the particle must be within the hill radius of the remnant, and the particle must have a velocity slower than the escape velocity in the remnant's reference frame. If these conditions are met, then the mass of the particle is added to the mass

of the remnant and the particle is flagged to be deleted. Once all particles have been checked, all flagged particles are removed from the simulation.

e) Data

The multistep N-body code is used to simulate the spatial evolution of the escaping vapour condensate from giant impacts. It is used to explore the parameter space in terms of orientation of the giant impact and distance from the star. We simulate each disk for 20 orbits of the progenitor with a small time step to precisely resolve the orbits of each tracer particle. With each time step, we output the positions, velocities and mass of each particle with which we are able to compare between disks how they evolve. We can also use these results to estimate the flux from a simulated disk by passing them onto RADMC3D (section 2.4).

2.3.2 Rebound

Rebound is a general use N-body code that is open source Rein & Liu (2012). While Rebound allows the choice of different integrators, we choose a simple leapfrog integrator as particles will be stepped linearly. This is important when we discuss collision detection in section 2.3.2 a). Rebound does not allow for adaptive stepping meaning the simulations are sympletic and time-reversible. Rebound uses the DK regime. The choice to switch to Rebound to simulate the spatial evolution of larger bodies in the ejecta of giant impacts was down to the collision detection algorithm LINETREE. As we needed a way to track collisions between the large bodies to track the creation of small debris.

All simulations use an oct-tree to determine the gravity of each particle. The acceleration on particle i is calculated by,

$$\boldsymbol{a}_i = \sum_{j=0}^{N_{\rm active}-1} \frac{Gm_j}{(r_{ji}^2 + b^2)^{\frac{3}{2}}} \hat{\boldsymbol{r}}_{ji}, \tag{2.27}$$

where G is the gravitational constant, m_j is the mass of particle j, and $\boldsymbol{r}_{ji}$ is the relative distance between the two particles. The parameter b is the gravitational softening parameter which is set as a finite value to deal with close interactions that can result in nonphysical accelerations. In our simulations, we set $b = 0$ so eqn. 2.27 becomes the standard equation for gravity between two objects. The use of an oct-tree means we must define a box for every simulation. We set the box size to be 50 au. Any particle that leaves the box is removed from the simulation.

a) Collision Detection

LINETREE uses an oct-tree to find groups of particles which could have overlapped during the last time step. As we use an oct-tree for the gravity calculations, Rebound does not require a new tree to be built for LINETREE. It not only checks to see if particles are overlapping at the end of the time step but also if they overlapped during the duration of the last time step.

First LINETREE calculates the max drift of any particle within the last time step. The max drift defines whether leaf nodes will need to be opened. Before any leaf nodes are opened, a collision check is done within the cell containing the particle being checked against all other particles in the cell. The collision check starts with calculating the start and end positions and velocities of both particles being checked. Assuming the path taken is linear then it is possible to check for the time within the last time step when the two particles had the closest approach. The distance between the two particles at the closest approach is then checked against the sum of the radii of the two particles, if the distance is smaller then a collision is recorded.

If no collisions have occurred within the cell for a given particle, leaf cells are then opened according to the opening criteria. The opening criteria is defined as

$$d_{pc} < r_p + \delta t_{i-1}|\boldsymbol{v}|_p + d_{\max} + 0.87 l_c, \tag{2.28}$$

where d_{pc} is the distance from the particle to the cell, r_p is the particle radius, δt_{i-1} is the time step used before the current step i, $|\boldsymbol{v}|_p$ is the current velocity of the particle, $d_{\max}$ is the max drift, and l_c is the length of the cell being checked. The collision check moves down the tree until either no cells meet the requirement and no collision is recorded for the particle or a collision is detected and recorded. The process then loops over all other particles that have not been involved in a collision until all particles have been checked.

b) Collision Outcomes

Once the collisions have been detected, they have to be resolved. The outcome of the collision will be function of the impact velocity, total mass, mass ratio and impact angle. The collisions are therefore measured using the ratio between the impact velocity and the catastrophic impact velocity, v_i/V^*, where the catastrophic impact velocity is the impact velocity needed to remove 50% of the mass from the impact. With each collision not being simulated up to the point of contact, we assume all collisions are head-on which eliminates impact angle as a parameter we

have to track. Assuming all impacts are head-on will reduce the value of V^*, and so collisions are going to be more destructive on average.

To determine V^* for each collision we use methods outlined in Leinhardt & Stewart (2012). First we define a radius, R_{C1}, of the combined bodies using the total mass of the impact and a density $\rho_1 = 1000\ \mathrm{kg\ m^{-3}}$. Using R_{C1} we calculate the critical impact velocity with mass ratio $\gamma = 1$,

$$V^*_{\gamma=1} = \left(\frac{32\pi c^* \rho_1 G}{5}\right)^{1/2} R_{C1} \tag{2.29}$$

,

where c^* is the material parameter. We set $c^* = 5$ which is the value determined for small bodies. From $V^*_{\gamma=1}$, we can calculate V^* by

$$V^* = \left[\frac{1}{4}\frac{(\gamma+1)^2}{\gamma}\right]^{1/(3\bar{\mu})} V^*_{\gamma=1}, \tag{2.30}$$

where $\bar{\mu}$ is a dimensionless material parameter. We set $\bar{\mu} = 0.37$ the value found to be the best fit for small bodies (Leinhardt & Stewart, 2012).

We cannot simulate every impact individually in a disk of planetesimals to determine the mass lost from the impact. Hence, we simplify the outcomes of the impacts into three different categories: mergers, bouncing, and completely destroyed. The outcome is determined by the v_i/V^* ratio: perfect mergers occur when $v_i/V^* < 0.1$, bouncing occurs when $0.1 \leq v_i/V^* < 2$, and complete destruction is when $v_i/V^* \geq 2$. Mergers and bouncing collisions are dealt with using inbuilt functions in Rebound. Perfect mergers will follow the trajectory of the combined velocity vectors with momentum conserved. Bouncing collisions are assumed to be completely elastic, again with momentum conserved. Completely destructive collisions results in both bodies being destroyed. The positions, velocities, and mass of each body is recorded along with the time of the collision. Both bodies then have their masses and radii set to 0, hence can not be in another collision.

c) Time Step Selection

The time step selection is important as it will vary the number of collisions we record as well as the initial distribution of particles in the simulation. All particles are launched from the same location hence will be heavily influenced by the gravitational interactions with remnant(s) in the first few steps. A suitably small time step must then be chosen. We choose to set the time step

to be $P/2000$, where P is the period of the progenitor orbit. The choice to scale the time step with period means we keep a consistent number of steps per orbit of the progenitor. This allows us to compare disks placed at different positions around the star as the number of steps per orbit is kept the same, hence the number of collision checks remains the same. The choice of $P/2000$ allows for accurate measurement of forces on particles near to the remnant(s) and the star.

d) Planetesimal Properties

The planetesimals used to simulate the evolution of a boulder population are generated from the final snapshot of a giant impact SPH simulation. The largest planetesimals are defined as remnants with 100 or more particles in the SPH simulation using methods for detecting gravitationlly bound objects outlined in section 2.3.1a). The largest remnant (and second largest dependent on the mass ratio, $M_{\rm lr}/M_{\rm slr} > 0.2$) are treated separately to the planetesimal population. These remnants make up the largest in a size distribution, with the rest being generated from the unbound escaping mass in the SPH simulation.

We assume that planetesimals forming from the unbound SPH particles will only form from particles with a vapour fraction of $< 10\%$. We call this mass the boulder mass. The melt mass in higher vapour fraction particles is assumed to be inhibited at growing large planetesimals by large bubbles of expanding vapour. The boulder mass is used to generate a size distribution of planetesimals starting from the smallest remnant found in the SPH simulation. We assume that the size distribution takes the form of $dN \propto d^{-3}$. We choose a value of -3 instead of the standard value of -3.5 for a debris disk as we wanted more of the boulder mass occupied by the smaller planetesimals hence increasing the number of particles used in each Rebound simulation.

The planetesimals are each set vectors in terms of spherical polar coordinates with values for absolute velocity, $|v|$, and the direction being determined from angles ϕ and θ. The polar angle ϕ is defined in the plane of the collision. The values for $|v|$, ϕ, and θ are randomly drawn from distributions set by the unbound particles in the SPH simulation. A log-normal is used to set the distribution for $|v|$, while the two distributions for ϕ and θ are more complicated so are fit from binned distributions. All coordinates are converted to Cartesian coordinates and are evolved for a short time (between 0.1 and 30 hours) before being placed into Rebound. The planetesimals are given a bulk velocity which matches the velocity of the progenitor orbit. An orientation is given to the planetesimal population which represents the collision orientation. The orientation

changes the direction of the kicks given to the planetesimals.

2.4 Radiative Transfer code: RADMC3D

RADMC3D is a radiative transfer code that solves the radiative transfer equation for complex systems using a Monte-Carlo solver developed by Dullemond et al. (2012). The inputs needed in order to model a system are a dust density grid, dust opacities, and a source of radiation. Throughout our work we use a Solar-like blackbody as the source of radiation placed at the origin of the grid for all models. In sections 2.4.1 and 2.4.2 I give a detailed breakdown how RADMC3D calculates radiative transfer processes. In section 2.4.3 I discuss the use of the opacity tool developed to determine the DIANA standard opacities (Woitke et al., 2016; Toon & Ackerman, 1981) which gives us the dust species used to determine the flux from a disk. Finally, in section 2.4.4 I outline the process in which RADMC3D produces lightcurves from synthetic data.

2.4.1 Dust Temperature

RADMC3D uses methods outlined in Bjorkman & Wood (2001) to calculate the temperature of the dust. These are outlined below. The source luminosity is divided into N_ν discrete photon packets. These photon packets are emitted over a time internal, Δt, so have an energy per packet, E_ν as

$$E_\nu = \frac{L\Delta t}{N_\nu}. \tag{2.31}$$

A frequency for the photon packet is chosen randomly from the SED of the source. The frequency will determine the absorptive and scattering opacities of the dust, $\kappa_\nu^{\rm abs}$ and $\kappa_\nu^{\rm scat}$. The environment the photon packet is emitted into is divided into spatial grid cells with each cell having a volume V_i, where i is the cell index. Anytime a photon packet enters a cell, the temperature is increased. Note, this differs from Bjorkman & Wood (2001) which only increases the temperature if a discrete absorption event has taken place. The number of photon packets entering a cell is counted, N_i. Therefore, the total energy to enter each cell is

$$E_i^{\rm enter} = N_i E_\nu. \tag{2.32}$$

It is assumed that the dust is in local thermodynamic equilibrium (LTE). The approximation holds as usually the dust cooling/heating timescales are much shorter than any time-dependent

dynamics of the system. A single temperature is also adopted for the dust. As the dust is in thermal equilibrium, any energy absorbed must then be re-emitted. The dust has a thermal emissivity of $j_\nu = \kappa_\nu \rho B_\nu(T)$, where ρ is the density of the dust in the cell and $B_\nu(T)$ is the Planck function at a temperature T. The energy emitted is then

$$E_i^{\rm em} = 4\pi\Delta t \int dV_i \int \rho\kappa_\nu B_\nu(T) d\nu = 4\pi\Delta t \int \rho\kappa_\rho(T) B(T) dV_i \tag{2.33}$$

where $\kappa_\rho = \int \kappa_\nu B_\nu d\nu / B$ is the Planck mean opacity and $B = \sigma T^4/\pi$ is the frequency integrated Planck function. If we adopt a constant temperature, T_i, in the cell then equation 2.33 becomes

$$E_i^{\rm em} = 4\pi\Delta t \kappa_\rho(T_i) B(T_i) m_i, \tag{2.34}$$

where m_i is the mass of the cell. Now as the dust is in LTE, we can equate equation 2.32 and 2.34 and find the temperature after N_i packets have entered a cell via

$$\sigma T^4 = \frac{N_i L}{4 N_\nu \kappa_\rho(T_i) m_i}. \tag{2.35}$$

Equation 2.35 is an implicit equation for T. As κ_ρ is a slow varying function of T, a solution can be found using an iterative process.

With the temperature increase, the emitted packets previous were emitted with the incorrect frequency. The previous emissivity is $j'_\nu = \kappa_\nu B_\nu(T_i - \Delta T)$, where ΔT is the increase in temperature caused by the most recent packet to enter the cell. The total energy being emitted should now have an emissivity of j_ν at the new temperature T_i. So, the additional energy needed to be carried away is given by

$$\Delta j_\nu = j_\nu - j'_\nu = \kappa_\nu [B_\nu(T_i) - B_\nu(T_i - \Delta T)]. \tag{2.36}$$

As long as the energy per packet, E_ν is small, the change in temperature is small, hence equation 2.36 can be approximated to

$$\Delta j_\nu \approx \kappa_\nu \Delta T (dB_\nu/dT). \tag{2.37}$$

To correct the previously emitted spectrum, the packet is re-emitted instantaneously with a chosen frequency from the shape of Δj_ν. The distribution is normalised to give the temperature correction probability distribution

$$\frac{dP_i}{d\nu} = \frac{\kappa_\nu}{K} \left(\frac{dB_\nu}{dT} \right)_{T=T_i}, \tag{2.38}$$

the probability of reemitting a packet between frequencies ν and $\nu + d\nu$, with $K = \int_0^\infty \kappa_\nu (dB_\nu/dT) d\nu$ being the normalisation constant.

The temperature is calculated as follows. Each photon packet is released one at a time from the source. The packet will move through the medium, changing direction when scattered or absorbed/re-emitted. Each time a packet enters a cell, the temperature in the cell increases. Once the packet leaves the defined box of the model, the next photon packet is launched. This continues up until all photon packets, N_ν have been launched. Initially for the first few photon packets, the initial temperature in all cells will be zero, meaning that the initial temperature change will not be small which is required by equation 2.37. However, this poses no issues as the number of packets that produce the initial temperature are on order of the number of spatial grids. Also, these packets are re-emitted at such long wavelengths they will not be observed.

2.4.2 Dust Scattering

Dust scattering plays an important role when tracing a photon packet through the medium. RADMC3D allows multiple different scattering configurations, we choose anisotropic scattering using Henyey-Greenstein approximation. The transfer equation along each ray is defined as

$$\frac{dI_\nu}{ds} = j_\nu^{\rm therm} + j_\nu^{\rm scat} - (\alpha_\nu^{\rm abs} + \alpha_\nu^{\rm scat}) I_\nu, \tag{2.39}$$

where I_ν is the intensity at a frequency ν, and s is the path length of the ray. By assuming that there is only one dust species with a density distribution ρ, absorption opacity $\kappa_\nu^{\rm abs}$ and scattering opacity $\kappa_\nu^{\rm scat}$ then

$$\begin{aligned} \alpha_\nu^{\rm abs} &\equiv \rho \kappa_\nu^{\rm abs} \\ \alpha_\nu^{\rm scat} &\equiv \rho \kappa_\nu^{\rm scat} \\ j_\nu^{\rm therm} &= \alpha_\nu^{\rm abs} B_\nu(T). \end{aligned} \tag{2.40}$$

In an isotropic scattering regime, the scattering source function is

$$j_\nu^{\rm scat} = \frac{\alpha_\nu^{\rm scat}}{4\pi} \oint I_\nu d\Omega. \tag{2.41}$$

In the isotropic case, $j_\nu^{\rm scat}$ does not depend on the solid angle. To account for anisotropic scattering a scattering phase function, $\Phi(\boldsymbol{n}_{\rm in}, \boldsymbol{n}_{\rm out})$, is introduced where $\boldsymbol{n}_{\rm in}$ is the unit vector for the scattered radiation and $\boldsymbol{n}_{\rm out}$ is the unit vector for the scattered radiation. The scattering phase function is normalised to unity so that

$$\frac{1}{4\pi} \oint \Phi(\boldsymbol{n}_{\rm in}, \boldsymbol{n}_{\rm out}) d\Omega_{\rm in} = \frac{1}{4\pi} \oint \Phi(\boldsymbol{n}_{\rm in}, \boldsymbol{n}_{\rm out}) d\Omega_{\rm out} = 1. \tag{2.42}$$

The scattering source function then becomes

$$j_\nu^{\rm scat}(\boldsymbol{n}_{\rm out}) = \frac{\alpha_\nu^{\rm scat}}{4\pi} \oint I_\nu(\boldsymbol{n}_{\rm in})\Phi(\boldsymbol{n}_{\rm in},\boldsymbol{n}_{\rm out})d\Omega_{\rm in}, \tag{2.43}$$

which is now angle dependent. If polarisation is not included and it is assumed that the particles are randomly orientated, then the scattering phase function only depends on the scattering angle θ where

$$\cos\theta \equiv \mu = \boldsymbol{n}_{\rm in}\cdot\boldsymbol{n}_{\rm out}. \tag{2.44}$$

The scattering source function now is normalised as

$$\frac{1}{2}\int_{-1}^{1}\Phi(\mu)d\mu = 1. \tag{2.45}$$

The scattering phase function can be approximated using the Henyey-Greenstein function,

$$\Phi(\mu) = \frac{1-g^2}{(1+g^2-2g\mu)^{3/2}}, \tag{2.46}$$

where g is the anisotropy parameter which is set by the opacity file given for the dust parameters.

2.4.3 Opacity Tool

The dust opacities and the anisotropy parameter are determined from the Opacity tool developed to determine the DIANA standard opacities (Woitke et al., 2016; Toon & Ackerman, 1981). The DIANA project (the European FP7 project DiscAnalysis) was a project that brought together different aspects of dust and gas modelling, and multiwavelength datasets to agree on a set of agreed physical assumptions to be implemented in all modelling software. To calculate the dust opacities, a mixture of silicates (Dorschner et al., 1995) and amorphous carbon (Zubko et al., 1996) is used. The mixture used for the dust grains is 60% silicate, 15% amorphous carbon, and 25% porosity. The size distribution used for the dust grains is $n(d) \propto d^{-3.5}$. The minimum size used for the grains was $0.5\ \mu$m and the maximum size was 1 mm. The output gives wavelength bins ranging from $0.05\ \mu$m to 500μm with each bin having a corresponding $\kappa_\nu^{\rm abs}$, $\kappa_\nu^{\rm scat}$, and g values.

2.4.4 Creating Images

Creating an image for a given angle and wavelength is a multistep process. First the dust temperature must be determined, second the dust scattering must be determined, and finally ray-tracing to the camera.

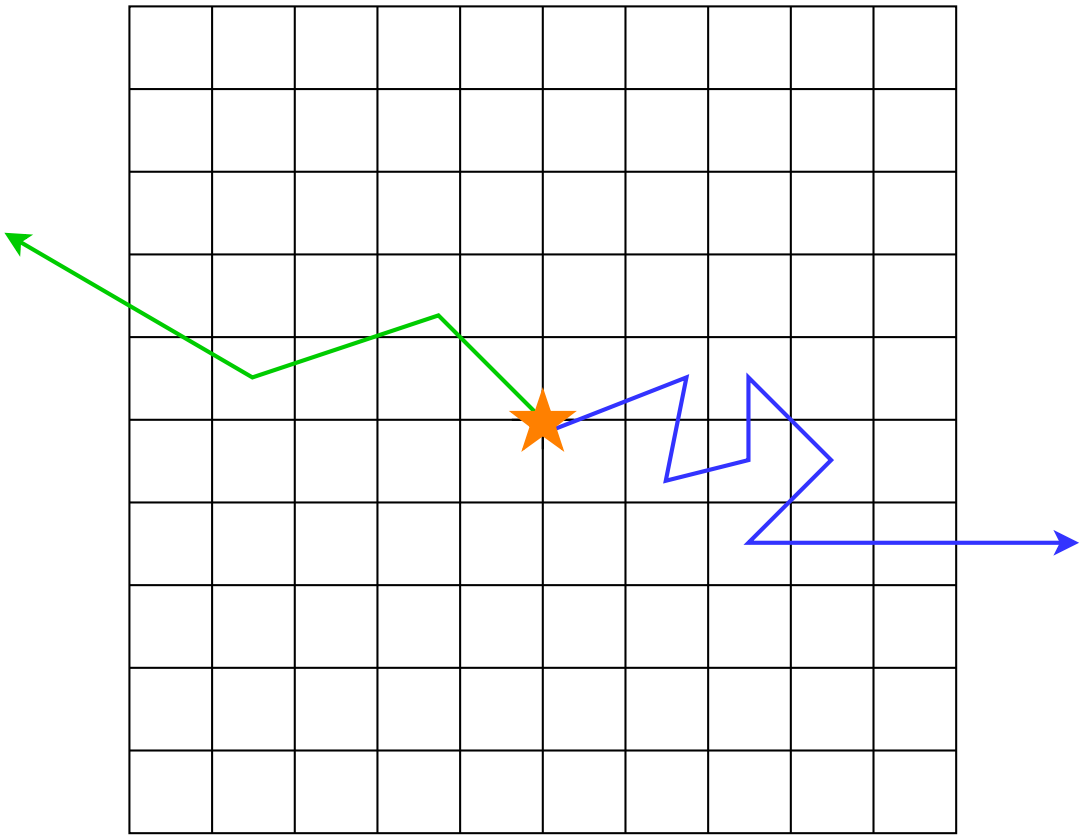

Figure 2.7: Diagram of the Monte-Carlo method used in RADMC3D. The grid represents the cells determined from the dust species used and the density grids provided. Photon packets are emitted from the star one at a time. The blue line represents a photon packet which undergoes many absorption/emission and scattering events due to passing through a dense area of material. The green line represents a photon packet passing through a low dense region. Photon packets are removed when leaving the grid, allowing another photon packet to be emitted from the star.

The dust temperature is calculated from a dust density grid of points using a Monte-Carlo method and the recipe outlined in section 2.4.1. Fig. 2.7 demonstrates how the Monte-Carlo method works for RADMC3D. We split the grid into 301^3 bins spanning 3 times the semi-major axis of the progenitor orbit in all three Cartesian planes. We use a Sun-like blackbody with a peak temperature of 5800 K for the star in the system. The star is placed at the origin. The dust temperature was calculated from 10^5 photon packets. The photon packets were released from the source one at a time, and only removed when the photon left the spatial grid. This was repeated until all photon packets had been released and removed.

In order to create an image, we need to specify the wavelengths we observe at. We chose $3.6\ \mu\mathrm{m},\ 4.5\ \mu\mathrm{m},\ 10\ \mu\mathrm{m}$, and $24\ \mu\mathrm{m}$. We also need to specify the camera position, we set to only observe each disk face-on. For each wavelength and camera position, another Monte-Carlo run is needed to calculate the emissivity, j_ν^{scat}, and extinction, $\alpha_\nu^{\mathrm{scat}}$, from dust scattering. For the scattering run 10^4 photon packets were used. Once the scattering run has completed then ray-tracing is used to calculate the flux for the given camera position and wavelengths.

RADMC3D uses first-order integration of the transfer equation across the ray. In each cell it is assumed that the emissivity function j_ν and the extinction function α_ν are constant. The integration proceeds over each cell with

$$I_{\mathrm{result}} = I_{\mathrm{start}} e^{-\tau} + (1 - e^{-\tau}) S, \tag{2.47}$$

where $S = j_\nu / \alpha_\nu$ is the source function, $\tau = \alpha \Delta s$ is the optical depth of the ray through the cell and I_{start} is the intensity of the ray when entering the cell. Fig. 2.8 shows a representation of the first order integration of the transfer equation across a ray that passes through the grid. As extreme debris disks are not currently spatially resolved, we sum each pixel in the generated images to get the total spectral radiance from the disk at a given time step. A lightcurve is then determined from the disk by the variation in the spectral radiance over time. Typically we want to display the lightcurves as excess flux at given wavelengths in units of Jy, RADMC3D returns images with units of $\mathrm{erg\ s^{-1}\ cm^{-2}\ Hz^{-1}\ \Omega^{-1}}$. To convert between spectral radiance and flux, we assume the system is placed at a distance of 80 pc away with the area of the image being known hence giving an angular size and then use a conversion factor of 10^{23} to get the flux in Jy.

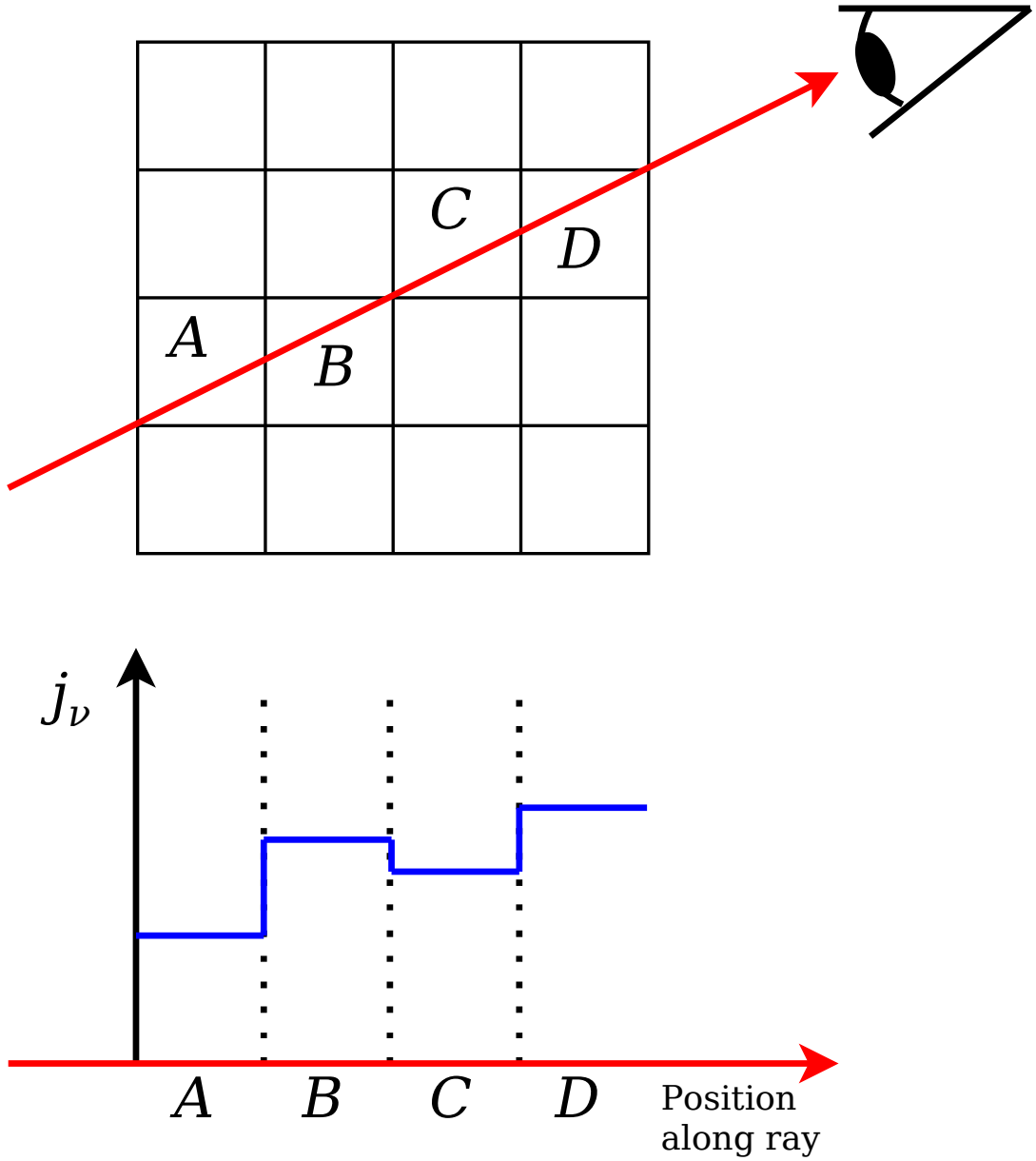

Figure 2.8: Representation of the first-order integration of the transfer equation. The red line represents the ray which passes through cells A, B, C, and D in the grid. The bottom diagram shows the assumed integrands for the cells. The emissivity function j_ν and the extinction function α_ν are constant across each cell, and hence constant across each ray segment.

3

Planetary Embryo Collisions and the Wiggly Nature of Extreme Debris Disks

This chapter is adapted from a paper published in MNRAS (Watt et al., 2021).

Abstract

In this chapter, we present results from a multi-stage numerical campaign to begin to explain and determine why extreme debris disk detections are rare, what types of impacts will result in extreme debris disks and what we can learn about the parameters of the collision from the extreme debris disks. We begin by simulating many giant impacts using a smoothed particle hydrodynamical code with tabulated equations of state and track the escaping vapour from the collision. Using an N-body code, we simulate the spatial evolution of the vapour generated dust post-impact.

We show that impacts release vapour anisotropically not isotropically as has been assumed previously and that the distribution of the resulting generated dust is dependent on the mass ratio and impact angle of the collision. In addition, we show that the anisotropic distribution of post-collision dust can cause the formation or lack of formation of the short-term variation in flux depending on the orientation of the collision with respect to the orbit around the central star. Finally, our results suggest that there is a narrow region of semi-major axis where a vapour generated disk would be observable for any significant amount of time implying that giant impacts where most of the escaping mass is in vapour would not be observed often but this does

not mean that the collisions are not occurring.

3.1 Introduction

It was discussed in chapter 1 the potential link between giant impacts between planetary embryos and extreme debris disks. We need to understand how different giant impacts change the observed extreme debris disk or even if we do observe an extreme debris disk. The detection rate of observing extreme debris disks does not match the rate that is required to explain the frequency of terrestrial planets (Meng et al., 2015), with hot dust only being found around 1% of young Sun-like, FGK, stars (Kennedy & Wyatt, 2013). This points towards one of two possibilities: 1) that large embryo-embryo collisions are not as prominent in the planet formation process as models predict or 2) the post-collision escaping material does not survive and is thus not observable for as long as predicted.

Previous work has been able to explain some of the general flux behaviour (Jackson & Wyatt, 2012; Jackson et al., 2014; Kral et al., 2015) and the oscillatory behaviour shown in some disks (Su et al., 2019) by assuming that the escaping material after a giant collision is isotropically distributed. However, the timescale that a clump shears out due to its Keplerian motion is dependent on the initial velocity distribution of escaping debris, meaning an isotropic distribution may not be realistic. The asymmetry in a given collision can have a profound effect on the resulting debris disk. In this chapter we have conducted a wide range of giant impacts to better understand how the distribution of escaping vapour will differ between various impact parameters with the goal of understanding the effects of said impacts on detection rate of extreme debris disks. We also look at the initial evolution of the escaping material for the whole suite of giant impact simulations to find what causes the very short term oscillatory behaviour in some extreme debris disks. Our methods are outlined in section 3.2, which explains each step of our numerical investigation from the simulations of giant impacts using smoothed particle hydrocode (SPH), to the evolving of the dust produced using a basic N-body integrator, and finally to the radiative transfer calculations of the debris emission by RADMC3D. In section 3.3, we discuss the observability of extreme debris disks and how it will vary with differing parameters. Section 3.4 outlines the limitations of our study. We conclude our results in section 3.5.

3.2 Methods

Our numerical method is divided into three steps: 1) direct SPH simulations of giant impacts; 2) N-body simulations of escaping post-collision vapour; and 3) radiative transfer and production of a synthetic observation.

3.2.1 Step 1: Giant Impacts (SPH)

We model planetary embryo-embryo collisions using a modified version of the SPH code GADGET-2 (Springel, 2005; Marcus et al., 2009). A more detailed description of how GADGET-2 was used is presented in section 2.2. The planetary embryos are modelled as a composite of iron (core) and forsterite (mantle) with a mass ratio of 3:7 and given initial temperature profiles from Valencia et al. (2006). Both core and mantle use the ANEOS equations of state (Melosh, 2007; Marcus et al., 2009; Carter et al., 2019a) and are initialised and equilibrated similar to previous work (Carter et al., 2018; Denman et al., 2020).

A summary of all collision simulations presented in this work is shown in Tables A.1 and A.2 in the Appendix. In these simulations impact speeds are varied from $\sim 6\ \mathrm{km\ s^{-1}}$ (just below the velocity needed to vaporise forsterite, Davies et al. (2020)) to few v_{esc} ($\sim 40\ \mathrm{km\ s^{-1}}$), where

$$v_{\mathrm{esc}} = \sqrt{\frac{2G\left(M_{\mathrm{targ}} + M_{\mathrm{proj}}\right)}{R_{\mathrm{targ}} + R_{\mathrm{proj}}}}, \tag{3.1}$$

is the mutual escape speed and M_{targ}, M_{proj}, R_{targ}, and R_{proj} are the masses and radii of the target and projectile respectively. Note, the maximum speeds of simulations at higher impact angle were extended to $\sim 5v_{esc}$. The range of impact speeds were chosen to be fast enough to produce some vapour but slow enough to result in either embryo growth or a hit-and-run event as informed by results from numerical simulations of planet formation (for example, Carter et al., 2019b). Three different impact parameters of $b = 0,\ 0.4,\ \mathrm{and}\ 0.8$ (where $b = \sin\theta$ and θ is the impact angle) ranging from head-on to grazing were used to test how the initial impact parameter influences the observability of the escaping material. Mass ratio ($\mu = \mathrm{M_{proj}/M_{targ}}$) is varied from 0.09 to 1 to understand if differing masses between the target and the projectile will have a large effect on the distribution of escaping material. The particle resolution used for the planetary embryos was between 2×10^4 and 2×10^5. This resolution allows for a large range of simulations to be run in reasonable time and is sufficient for determining the mass and distribution of the escaping vapour.

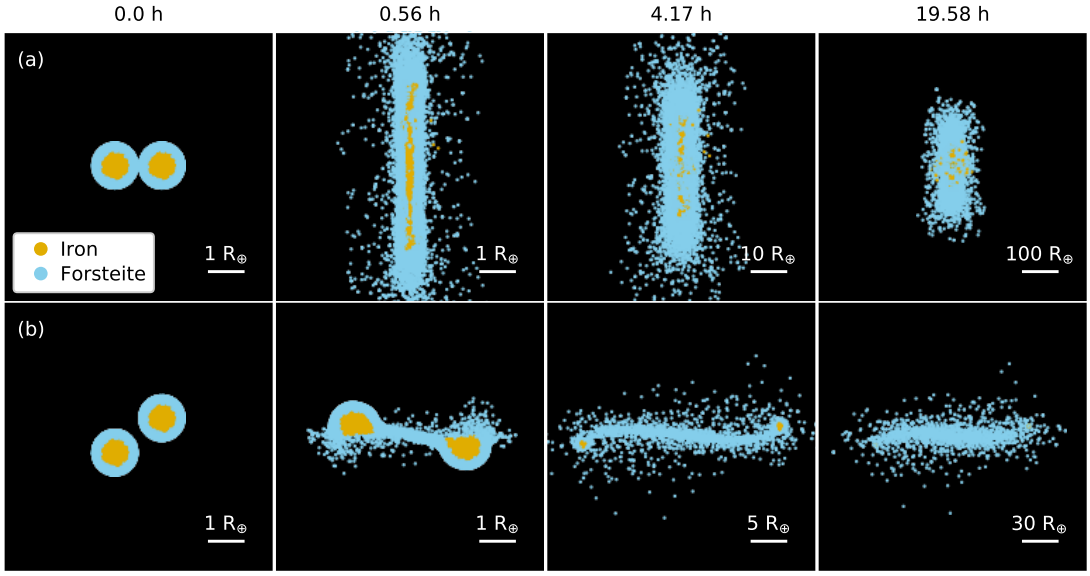

Figure 3.1: A hemispherical view of a giant impact between two planetary embryos of $0.1\mathrm{M}_{\oplus}$ at $10\mathrm{km\ s}^{-1}$ over 4 snapshots ranging in time from the initial collision to 19.58 hours post collision. A head-on impact (sim. 8, Table A.1) is shown in (a) and a hit-and-run grazing collision (sim. 88, Table A.2) is shown in (b). Material type is indicated by colour: forsterite mantle in blue and iron core in yellow. Images scale with distribution size with scale bar shown in bottom right hand corner of each subfigure. The impact in (a) results in material mostly being ejected perpendicular to the impact velocity vector with the remnant forming in the centre of the image. In (b) material is mostly ejected parallel to the impact velocity vector and trails the two remnants which are placed at either extremes in the image at 19.58 hours.

Even the relatively narrow range of collision parameters chosen for this work produce a large variety of collision outcomes. Figure 3.1 shows four snapshots of two isolated giant impacts at $10\ \mathrm{km\ s^{-1}}$ (1.99 v_{esc}) between equal mass 0.1 $\mathrm{M}_{\oplus}$ embryos at two different impact parameters: (a) head-on ($b = 0$, sim 8 in Table A.1) and (b) grazing collision ($b = 0.8$, sim 88 in Table A.1). Both collisions show non-isotropic distribution of material after the impact and continues past $\sim$19 hours of simulation time. In simulation 8 one significant largest remnant is produced with a mass of $1.45 \times 10^{-1}\mathrm{M}_{\oplus}$ and an escaping mass of $4.54 \times 10^{-2}\mathrm{M}_{\oplus}$. About 13.8% of the escaping material is in the form of vapour. The grazing collision shows an example of a hit-and-run collision with two largest remnants of equal size ($M_{\mathrm{lr}} = 9.56 \times 10^{-2}\mathrm{M}_{\oplus}$, roughly the initial mass of the targets). The amount of escaping mass is much less than the head on collision ($M_{\mathrm{unb}} = 7.18 \times 10^{-3}\mathrm{M}_{\oplus}$) and only 5.28% of the escaping material is vapour. We would expect these two collisions to look very different observationally. Just how different is something we investigate in the rest of chapter. The simulation outcomes are determined by methods laid out in the next subsection.

3.2.2 Step 2: Post-collision Dust Evolution (N-body)

To determine the observability of the vapour generated dust we need to constrain the dynamical behaviour and lifetime of the observable dust post-collision, which are governed by two parameters: the mass of the largest remnant(s) and the spatial and velocity distributions of the escaping material. In order to do this we developed a N-body code using a leapfrog integrator with adaptive timestepping which is described in detail in section 2.3.1. The collision outcomes from our isolated SPH simulations become input for our N-body code.

It is possible that some extreme debris disks actually show flux contributions from both the quickly generated and short lived vapour condensed dust and a secondary traditional debris disk generated by the boulder-sized giant impact remnants. We explore the latter possibility in chapter 4. In this chapter we will only focus on the early vapour generated dust disk. In future work we will include the background boulder population and investigate the possible interaction between the two dust populations.

a) Determining the Largest Remnant

The first step in determining how much vapour escapes from a given giant impact is to determine the mass of the largest post-collision remnant. In this work an iterative process is used starting

with the last snapshot (between 19 and 28 hours post collision). Each particle in the simulation is labelled as part of a resolved remnant, unresolved remnant, or identify it as unbound. The process begins by finding a seed particle. The seed particle is defined as the particle with the minimum potential energy when compared to all other particles. The process to define the largest remnant is outlined in section 2.2.3.a). Using the remnant finder process, we find a population of remnants and unbound particles. Remnants are defined only when the bound object found in remnant finder contains 500 particles or more in this study.

b) Finding the Vapour Fraction

The decay in infrared flux on a yearly timescale is present in ID8 and P1121 (multiple instances demonstrated in the case of ID8). This decay cannot be attributed to the blow-out of small grains (too quick), or the loss of mass through a typical steady-state cascade of km-sized planetesimals (too slow). Currently the most likely hypothesis is that the excess flux is caused by vapour condensate which is created by a giant impact between planetary embryos. The vapour quickly condenses into grain sizes that can range from microns to mm/cm (Meng et al., 2014, 2015; Su et al., 2019). The small characteristic size allows for a short collisional evolution. Therefore, for us to be able to simulate the early evolution of extreme debris disks, we need to know how much vapour is created in each impact and how it is distributed. We determine the vapour mass from vapour domes produced from ANEOS for iron and forsterite. The lever rule is used to obtain the vapour fraction within the vapour dome of each material. The detailed method is outlined in section 2.2.3.b). We are only focusing on vapour condensates in this study so we ignore melt mass as we assume melt mass will play no part in the instantaneous visibility of a varying extreme debris disk.

c) Dynamical Evolution

After identifying the largest remnants and the vapour fraction mass we hand off the data to a N-body code. The N-body code uses a multistep leapfrog integrator in a drift-kick-drift configuration. The details of the N-body code used in this chapter is outlined in section 2.3.1 The system now needs to be evolved in time. In the N-body simulations, the star (1 $M_{\odot}$) is at the origin. The centre of the dust distribution and the largest post-collision remnants are placed at the collision point, where the centre of the distribution is defined as the centre of mass of the largest remnant(s) of the isolated SPH simulation. The collision point is a variable parameter. For this

study, most collisions are positioned at 1 au, with an eccentricity of zero putting the impact on a circular orbit. For a select few impacts the semi-major axis is varied. The post-impact debris is given a bulk motion velocity, $v = \sqrt{GM_*/r}$, where M_* is the mass of the central star and r is the set semi-major axis, which would have been the orbital velocity of the progenitor planet prior to the impact. We note that a few impact velocities exceed or are comparable to the Keplerian velocity at 1 au which would be highly unlikely. However, these impacts are useful when considering extreme scenarios.

In the N-body code the condensate dust particles are treated like test particles and have no gravitational influence on each other. The largest remnant(s) gravitationally interact with each other and the dust. At the moment only the two largest post-collision remnants from the SPH simulations are used in the N-body code as most collisions will only produce one or two bodies that is massive enough to significantly influence the dust gravitationally. The input for the dust is obtained from the unbound particles found in the SPH simulations. As the number of unbound particles can be low, we upscale the SPH unbound particle distribution using methods outlined in section 2.3.1.a). The reference frame of the SPH giant impacts is centred on the centre of mass between the target and the projectile. The SPH simulation does not take into account any wider system information. The orientation of the impact with respect to the progenitor orbit is therefore unknown. To account for this we use two different orientations: 1) parallel to the progenitor orbit and; 2) perpendicular to the progenitor orbit. These two orientations are the most extreme we can set, hence if orientation plays a role in disk evolution we will see the most change between these two orientations.

3.2.3 Step 3: Synthetic Images (radiative transfer)

To model the flux seen from a collision we use RADMC3D (Dullemond et al., 2012), a general-purpose package for modelling radiative transfer in three spatial dimensions using Monte-Carlo methods. The model requires inputs for dust density and structure, dust opacity and a source. The dust density and structure are determined from our N-body outputs, and the source is a Sun-like blackbody emitter of 5800 K. The dust opacities are determined from the opacity tool developed to determine the DIANA standard opacities (Toon & Ackerman, 1981; Woitke et al., 2016; Min et al., 2005; Dorschner et al., 1995). A more detailed outline of how RADMC3D is used in this chapter is found in section 2.4. We sample the sepctral radiance at specified wavelengths which can then be converted to a flux from a system at a given distance away

from the observer. We produce images at 24 microns. The spectral radiance is sampled every 0.1 orbits to produce a lightcurve. The dust temperature is recalculated every step, there is no information passed between steps hence each image is produced in isolation.

3.3 Observability

Many factors will affect the observability of an extreme debris disk such as the position of the collision around the central star, the parameters of the collision, and distribution of escaping material post-collision. The first factor we consider is the escaping vapour mass produced in embryo-embryo collisions and its lifetime.

3.3.1 Vapour Production

As stated in section 3.2, we are focusing on the first observable debris disk produced by a giant impact created by the vapour condensate which forms small particles almost instantly post collision. To produce vapour, our collisions need to be super-sonic and shock-inducing which means impact speeds needed are dependent on material type. For our modelled planetary embryos with the mantle made of forsterite, the impact speed needed is $\geq 6\ \mathrm{km\ s^{-1}}$. (Davies et al., 2019, 2020). Collisions that are slower than this value will likely be fully dominated by melt material which form larger objects. Melt objects will collisionally evolve slowly as part of the background boulder population forming a traditional debris disk (Johnson & Melosh, 2014). We remove the melt mass as the focus of this chapter is the early evolution of extreme debris disks which are dominated by vapour condensates formed directly from the giant impact.

Figure 3.2 shows the vapour productions from all of the SPH impact simulations summarised in Table A.1 and A.2 over a range of mass ratio and impact parameter. As expected we find that as impact energy is increased the fraction of vapour produced by the impact increases. To zeroth-order the relationship between specific impact energy (Q_{R}) and vapour mass appears linear and independent of collision parameters such as μ and b with the data we have used. Using a least-squares fit to the data, we find the linear relation to be $M_{\mathrm{vap}}/M_{\mathrm{tot}} = 12.5 \pm 0.5 \times 10^{-2}\, Q_{\mathrm{R}}/Q^{*}_{\mathrm{RD}} + 0.4 \pm 0.2 \times 10^{-2}$ (black dashed line in Fig. 3.2), with errors indicating the level of scatter to 1 standard deviation in the data, where Q^{*}_{RD} is the catastrophic disruption threshold which is the energy needed to disrupt half the mass in a collision. At high b values there is some indication that the collision outcomes might deviate from the linear fit at $\gtrsim 1\ Q_{\mathrm{R}}/Q^{*}_{\mathrm{RD}}$,

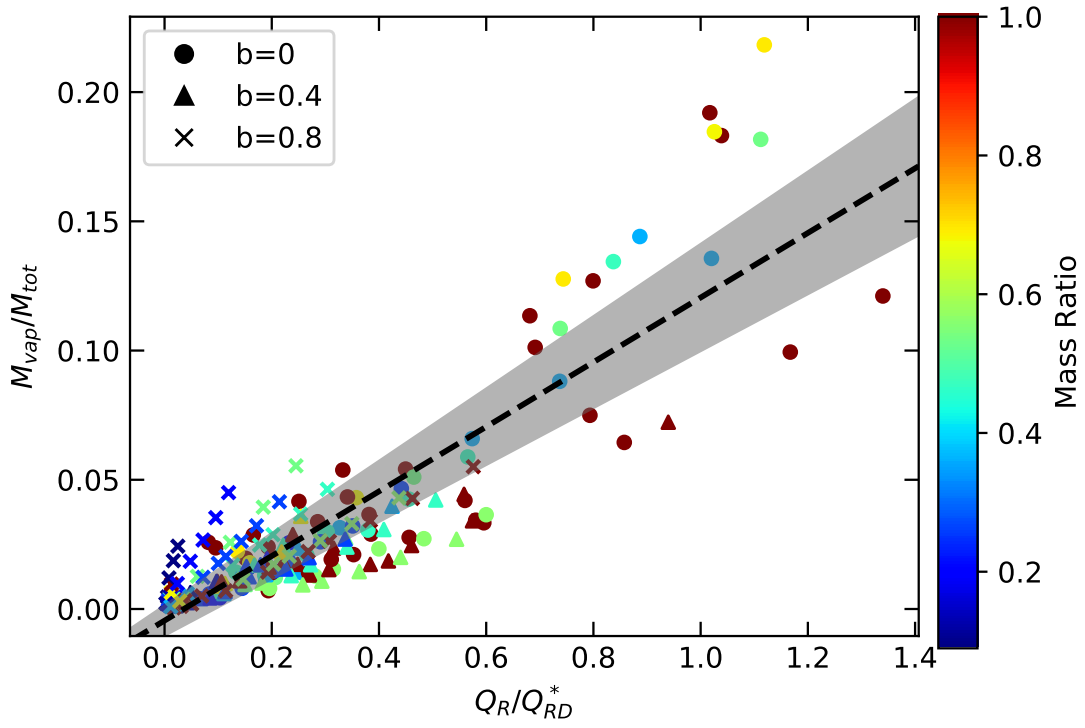

Figure 3.2: The mass of vapour ($M_{\rm vap}$) in units of total mass ($M_{\rm tot}$) produced in a given impact as a function of specific impact energy ($Q_{\rm R}$) in units of catastrophic disruption threshold ($Q^*_{\rm RD}$, the specific energy needed to permanently remove 50% of the system mass). Normalising using $Q^*_{\rm RD}$ allows us to know how destructive each collision was. Shape indicates impact parameter b, colour indicates mass ratio μ. The dashed line shows the zeroth order linear fit to the data with the grey area showing a 3 sigma deviation away from the fit.

however such collisions would require an extreme impact velocity which would be unlikely in most orbital configurations. Further study is needed to determine the relationship between between low μ, high b collisions and escaping vapour mass produced.

The vast majority of escaping vapour in our simulated giant impacts is from mantle material. The linear fit shown in Fig. 3.2 may break down at larger, more disruptive collisions when the core starts to make a significant contribution to the escaping vapour mass. This is because the position of the vapour dome for iron in temperature-specific energy space is different to that of forsterite. Iron has a larger triple-point temperature than forsterite, as a result, we might expect to see a discontinuity when a significant amount of the core vapourises. However, the simulations presented in this work extend from just above vapour production speed to 1.4 $Q_{\rm R}/Q^*_{\rm RD}$ (Carter et al., 2015), thus we cannot predict how the vapour production mass will scale with impact energy for very energetic giant impacts.

Although the amount of mass in vapour is relatively independent of b and μ there is a strong dependence on these parameters when determining which body (target or projectile) the vapour comes from (Fig. 3.3). As expected for equal mass impacts, the vapour mass is produced equally from both the target and projectile, which is true for all impact angles (parameter b). However, as μ decreases, the fraction of vapour production from the projectile is higher than that of the target. This behavior is also sensitive to the impact angles as shown in Fig. 3.3.

3.3.2 Initial Vapour Velocity Distribution

Planetary embryo impacts produce a variety of post-collision dust distributions, none are isotropic as has been assumed in previous work (e.g. Jackson & Wyatt, 2012; Jackson et al., 2014; Wyatt et al., 2017). To be able to compare different distributions, we need to characterise the anisotropic nature of the collisionally generated dust. We separate the velocity of each escaping particle into two velocity components, the velocity parallel ($v_{\parallel}$) and perpendicular ($v_{\perp}$) to the direction of the impact. For example, the direction of the impact is the same (along the x-axis) for the two collisions shown in Figure 3.1. To understand and compare different distributions of particles, we choose to take the range between the 16% and 84% percentiles to compute the velocity dispersion for both velocity components in each collision ($\Delta v_{\parallel}$ and $\Delta v_{\perp}$). This allows us to compare the velocity distribution of different distributions without assuming a given distribution for any collision. We choose to take the 16% and 84% percentiles as this would be comparable to taking the 1σ values either side of the mean of a normal distribution.

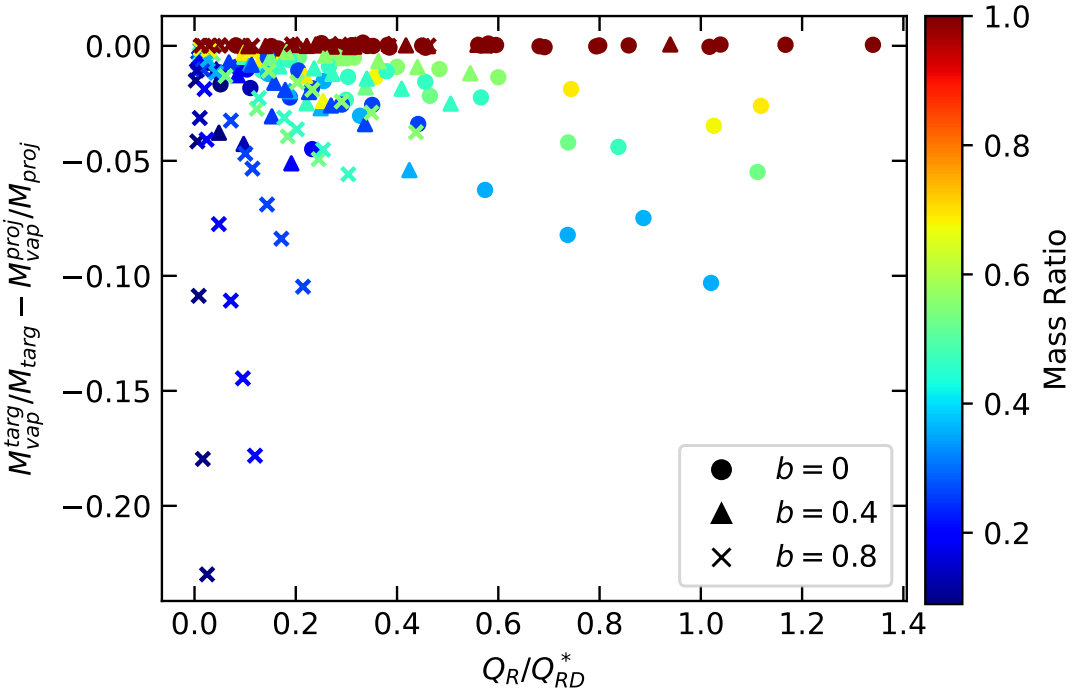

Figure 3.3: The difference between the escaping mass from the projectile normalised by projectile mass and the escaping vapour mass from the target normalised by the target mass versus the specific energy of the collision normalised by the catastrophic disruption criteria. Symbols and colour bar are same as in Fig. 3.2. As the mass ratio decreases, a greater proportion of the projectile is vapourised compared to the target with more energetic impacts. The deviation is enhanced with an increasing impact parameter.

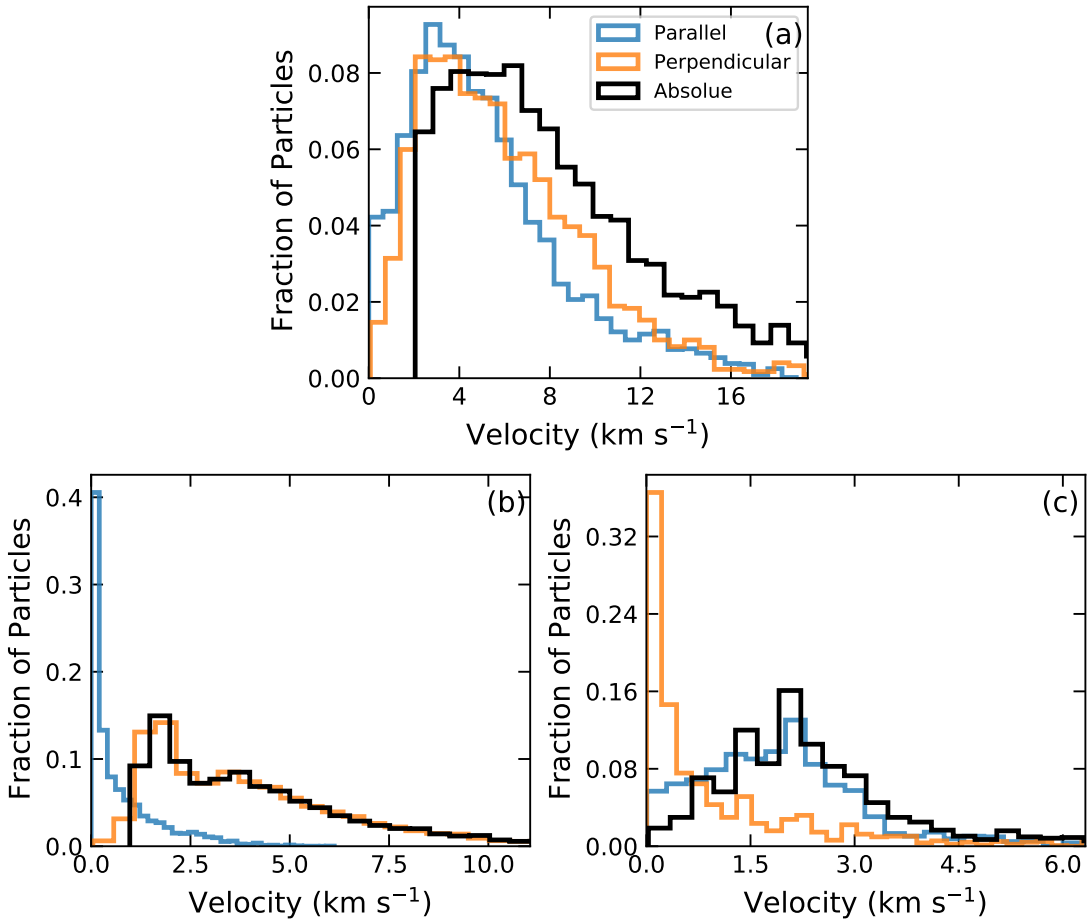

Figure 3.4: The absolute distribution of the launch velocities of vapour condensates with blue, orange, and black showing the parallel, perpendicular, and absolute velocity distributions respectively. (a) shows the distribution for sim 168, an impact between a 1.11 $M_\oplus$ and 0.1 $M_\oplus$ embryos with an impact velocity of 15 $\mathrm{km\ s^{-1}}$ at $b = 0.4$, an impact condition similar to the canonical Moon forming impact. (b) shows the distribution for sim 8, an head-on impact between two 0.1 $M_\oplus$ embryos with an impact velocity of 10 $\mathrm{km\ s^{-1}}$ and $b = 0$. (c) shows the distribution for sim 88, impact between two 0.1 $M_\oplus$ embryos with an impact velocity of 10 $\mathrm{km\ s^{-1}}$ and $b = 0.8$.

In Fig. 3.4 we show the absolute velocity distributions of vapour condensates parallel (blue) and perpendicular (orange) to the direction of the collision and absolute velocity (black) for three different giant impacts. Fig. 3.4(a) shows sim 168, a collision between 1.11 $\mathrm{M}_{\oplus}$ and 0.1 $\mathrm{M}_{\oplus}$ at 15 $\mathrm{km\,s^{-1}}$ and $b = 0.4$. We choose to show sim 168 as it is the closest simulated impact we have to the Moon-forming impact. Comparing to the Moon-forming pact in Fig. 1 of Jackson & Wyatt (2012), we have an overall similar distribution of absolute velocities and we find only a small difference between the direction vapour condensates are launched (close to isotropic). Fig. 3.4(b) shows sim 8, a collision between two 0.1 $\mathrm{M}_{\oplus}$ at 10 $\mathrm{km\,s^{-1}}$ and $b = 0$. Fig. 3.4(c) shows sim 88, a collision between two 0.1 $\mathrm{M}_{\oplus}$ at 10 $\mathrm{km\,s^{-1}}$ and $b = 0.8$. There is a stark difference between the direction vapour condensates are launched in sim 8 & 88 compared to sim 168. By only using a truncated Guassian to fit to the absolute velocities, therefore assuming isotropic distribution, we would lose a lot of information of how vapour condensates are distributed in the highly anisotropic giant impacts. Due to the anisotropic nature of giant impacts, the orientation of the impact with respect to the orbit of the centre of mass has a surprising effect on the structure of the debris disk (see Section 3.3.3).

Figure 3.5 shows the ratio between the velocity dispersion perpendicular and parallel to each impact against the specific energy of the impact normalised by the catastrophic disruption threshold. We can see the impacts are separated into three distinct groups defined by their impact parameter. Figure 3.6 shows the surface area covered by the particle velocity vectors when projected onto a sphere versus specific energy of the impact normalised by the catastrophic disruption threshold. Isotropic distributions will have a value close to 1, while a value close to 0 will mean a very anisotropic distribution. Collisions will likely kick particles in all directions, but a low area covered fraction will indicate clumping of velocity vectors in one or more directions. This difference in distribution of velocity will have an effect on the initial visibility of the dust which we will discuss in section 3.3.3.

For head-on impacts, $b = 0$, the majority of the impact debris is distributed toward the direction that is perpendicular to the impact direction, i.e., $\Delta v_{\perp}$ dominates for most $Q_{\mathrm{R}}/Q^{*}_{\mathrm{RD}}$ values. Mass ratio does not influence $\Delta v_{\perp}/\Delta v_{\parallel}$, and the ratio is a function of specific impact energy as the higher energy impact gives a larger ratio . Near 0.8 $Q_{\mathrm{R}}/Q^{*}_{\mathrm{RD}}$ the increase in $v_{\perp}/\Delta v_{\parallel}$ becomes shallower and potentially may plateau; however this needs to be confirmed by future simulations with more impacts at larger $Q_{\mathrm{R}}/Q^{*}_{\mathrm{RD}}$. The increase in $\Delta v_{\perp}/\Delta v_{\parallel}$ with $Q_{\mathrm{R}}/Q^{*}_{\mathrm{RD}}$ can be explained by looking at strip (a) in Fig.3.1. Impacts colliding head-on "pancake", pushing

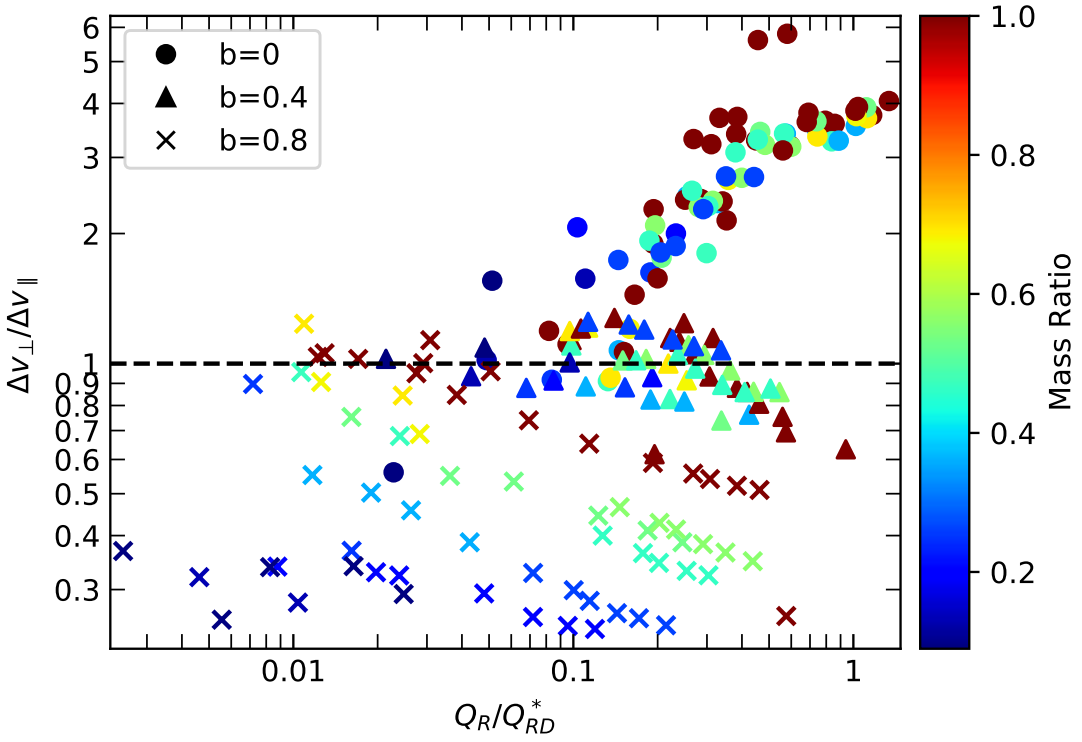

Figure 3.5: The ratio between the velocity dispersion perpendicular to the collision ($\Delta v_\perp$) and parallel to the collision ($\Delta v_\parallel$) versus the specific impact energy (Q_R) in units of catastrophic disruption threshold (Q^*_RD). Values above $1 \Delta v_\perp/\Delta v_\parallel$ indicates that more particles are ejected perpendicular rather than parallel to the impact velocity vector and values below one indicate the reverse. Shape indicates impact parameter b, colour indicates mass ratio $\mu = M_\mathrm{proj}/M_\mathrm{targ}$. Dashed line shows velocity dispersion ratio of 1.

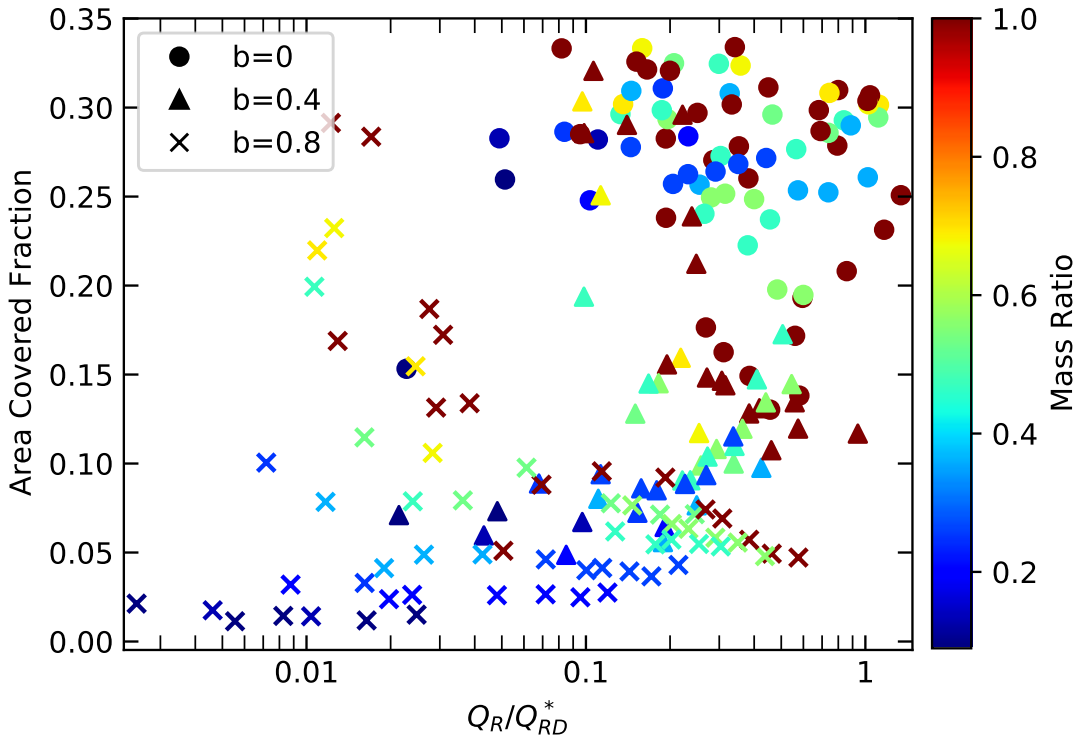

Figure 3.6: Anisotropy of collisions. The surface area covered by the particle velocity vectors projected onto the surface of a sphere for each collision. An isotropic distribution will have a value close to 1, a very anisotropic distribution will have a value close to 0. Shape indicates impact parameter b, colour indicates mass ratio $\mu = M_{\rm proj}/M_{\rm targ}$.

material perpendicular to the direction of the collision. Some material will be released parallel when material collapses back down, re-shocking the material. The area covering fraction of head-on impacts in Fig. 3.6 mostly fall between 0.25 and 0.35. This is expected as material is preferentially kicked perpendicular to the collision, but we see no variation across different $Q_{\rm R}/Q^*_{\rm RD}$ or mass ratio values. So for larger $Q_{\rm R}/Q^*_{\rm RD}$, the ratio of debris kicked perpendicular to parallel stays the same but debris kicked perpendicular will have a wider velocity distribution.

For impacts at $b = 0.4$, $\Delta v_\perp/\Delta v_\parallel$ stays around a value of 1 with a slight decrease at larger $Q_{\rm R}/Q^*_{\rm RD}$. Similarly, there is no variation with mass ratio. This suggests the $b = 0.4$ collisions might be isotropic, but Fig. 3.5 is misleading in isolation. If we consider the results shown in Fig. 3.6 we see that the $b = 0.4$ collisions are not isotropic as most of these impacts lie between 0.05 and 0.15 area covering fraction indicating that these collisions are very anisotropic, more so than the head-on impacts. There also seems to be a relationship between mass ratio and area covered, with lower mass ratios typically having a lower area covering fraction. So for these impacts to have a value roughly close to $\Delta v_\perp/\Delta v_\parallel = 1$ means debris must be preferentially launched close to 45° to the impact. At larger $Q_{\rm R}/Q^*_{\rm RD}$, we see a decline in $\Delta v_\perp/\Delta v_\parallel$ which might be caused by the projectile not fully interacting with the target, meaning a proportion of material is ejected in the direction of the collision. There also might be a mass ratio dependence. In Fig. 3.6, the area covering fraction seems to decrease with larger $Q_{\rm R}/Q^*_{\rm RD}$ for impacts with mass ratios close to 1, while mass ratios close to 0.1 show no variation. This suggests that impacts with mass ratios close to 1 become more anisotropic with increasing $Q_{\rm R}/Q^*_{\rm RD}$. One explanation for this is these impacts change in how debris is launched, though more impacts above 1 $Q_{\rm R}/Q^*_{\rm RD}$ are needed at different mass ratios to test this.

High impact angle, grazing impacts ($b = 0.8$) show behaviour which varies with the mass ratio of the impact. For large mass ratios (close to 1), the interacting mass fraction between the target and the projectile means both will survive the collision creating two remnants of similar masses, with some mass ejected parallel to the collision, giving small $\Delta v_\perp/\Delta v_\parallel$. The area covering fraction of most $b = 0.8$ impacts is small compared to $b = 0$ and $b = 0.4$ impacts, further suggesting the distribution is jet-like. At lower mass ratios, the projectile is preferentially disrupted over the target leading to material being ejected in the direction the projectile was moving in. This is backed up by the smaller area covering fractions for low mass ratio impacts. At low $Q_{\rm R}/Q^*_{\rm RD}$, $b = 0.8$ impacts seem to have a large area covered for larger mass ratio impacts. These impacts may not follow the jet-like distribution we would expect from

a high impact angle collision. While this is interesting, this might be caused by small number statistics because only a small number of particles escape in these low energy, high impact angle collisions.

3.3.3 Orientation

As we have discussed, post-collision velocity distributions are anisotropic and this has a profound effect on the early architecture of the extreme debris disk in determining both the spatial and flux evolution of the dust.

a) Spatial Evolution

Due to the anisotropy of the dust post-collision, a collision between two embryos with the same collision parameters but different orientations with respect to the progenitor orbit can produce debris disks which do not look alike. Figures 3.7 and 3.8 show time series of the vapour generated dust (increasing in time from left to right) from a head-on, equal-mass impact (sim 8) and a grazing equal-mass impact (sim 88) for two different collision orientations. The orientation of the impact is indicated in the upper right of frame (a). The top row in blue shows the dust distribution for an impact that occurs along the orbit whereas the orange time series in the second row shows the distribution resulting from an impact perpendicular to the orbit.

We find the overall disk evolution to be similar to that found in Jackson & Wyatt (2012) and Jackson et al. (2014), with the initial dust clump quickly transitioning into a spiral arm feature within 1 to 2 orbital phases. The spiral arm winds up over the subsequent orbital phases, forming concentric rings. However, there are some interesting differences in the details of the evolution of the four simulations. In Fig. 3.7, the orange disk, where the impact is perpendicular to the progenitor orbit, transitions from the spiral arm phase into the concentric ring phase quicker than the corresponding blue disk, where the impact was oriented along the orbit. The rings in the orange disk are more frequent and expand over a wider range of semi-major axis.

We see similar behaviour for sim 88 shown in Fig. 3.8. Equal mass, hit-and-run collisions preferentially launch vapour condensates along the direction of the collision rather than perpendicular like equal mass, head-on collisions (Fig. 3.1 and Fig. 3.5). Fig. 3.8 also shows four snapshots between the same two objects at the same speed as in Fig. 3.7 but now at $b = 0.8$ (sim 88) instead of $b = 0$ (sim 8). We see that sim 88 shows similar structures to that of sim 8, though for opposite orientations (blue in Fig. 3.7 is similar to orange in Fig. 3.8 and vice versa).

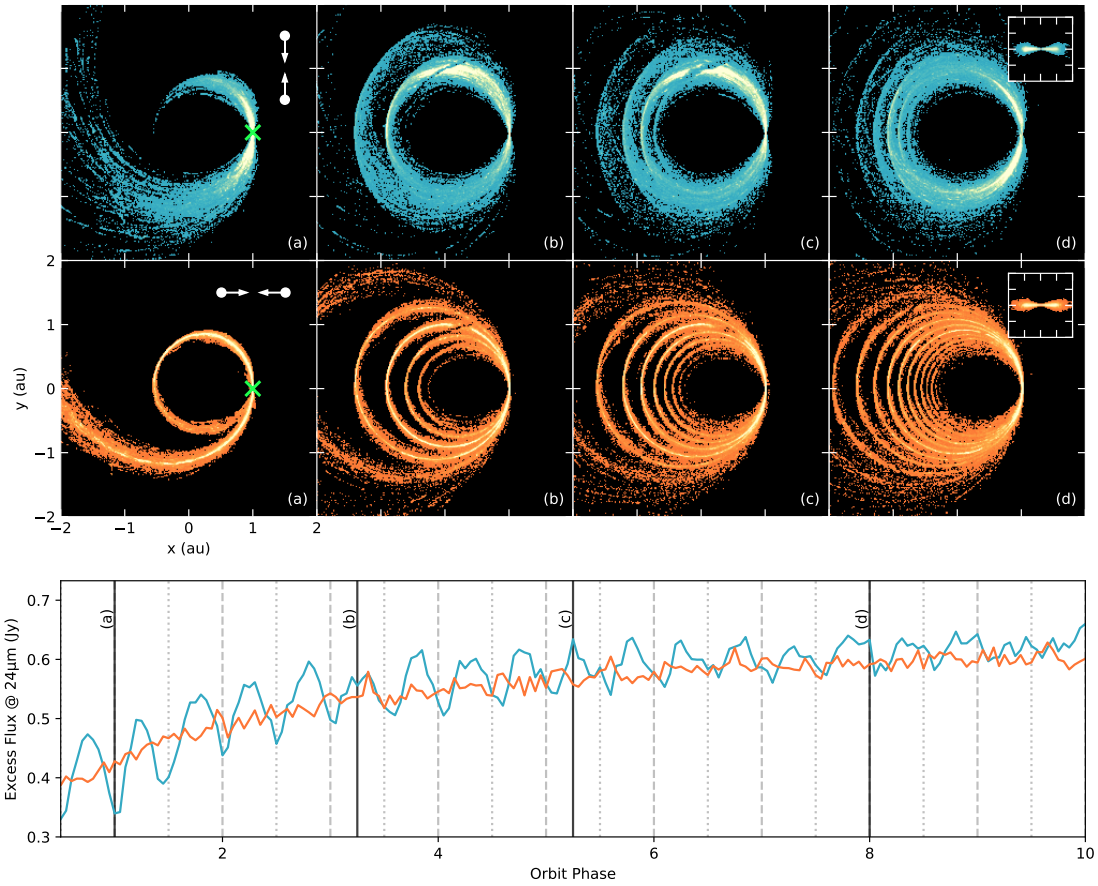

Figure 3.7: The time evolution of the dust clump released at 1 au from a head-on collision between two 0.1 $M_\oplus$ embryos at 10 km s^{-1}. The top panel shows four snapshots of the post-collision dust for two different orientations rotated by 90° as illustrated by the white dots with arrows signifying the orientation of the collision with respect to the progenitor orbit at the launch position located in the (a) panels. The green cross denotes the collision point. The bottom panel shows the flux evolution at 24 μm as the clump evolves assuming a face-on view of each disk with the line colours matching the snapshot colours above. Snapshots represent the number density of particles with the maximum showing 30 particles to show the structure of the disk. The snapshot times are shown in the flux plot by black solid lines with notations which relate back to the correct snapshot below. The greyed dashed and dotted lines show the expected orbit phase position of dips in flux occurring from the collision point and anti-collision line respectively. The inserts in the (d) panels show the edge-on (y–z) view of the disk with the collision point in the centre.

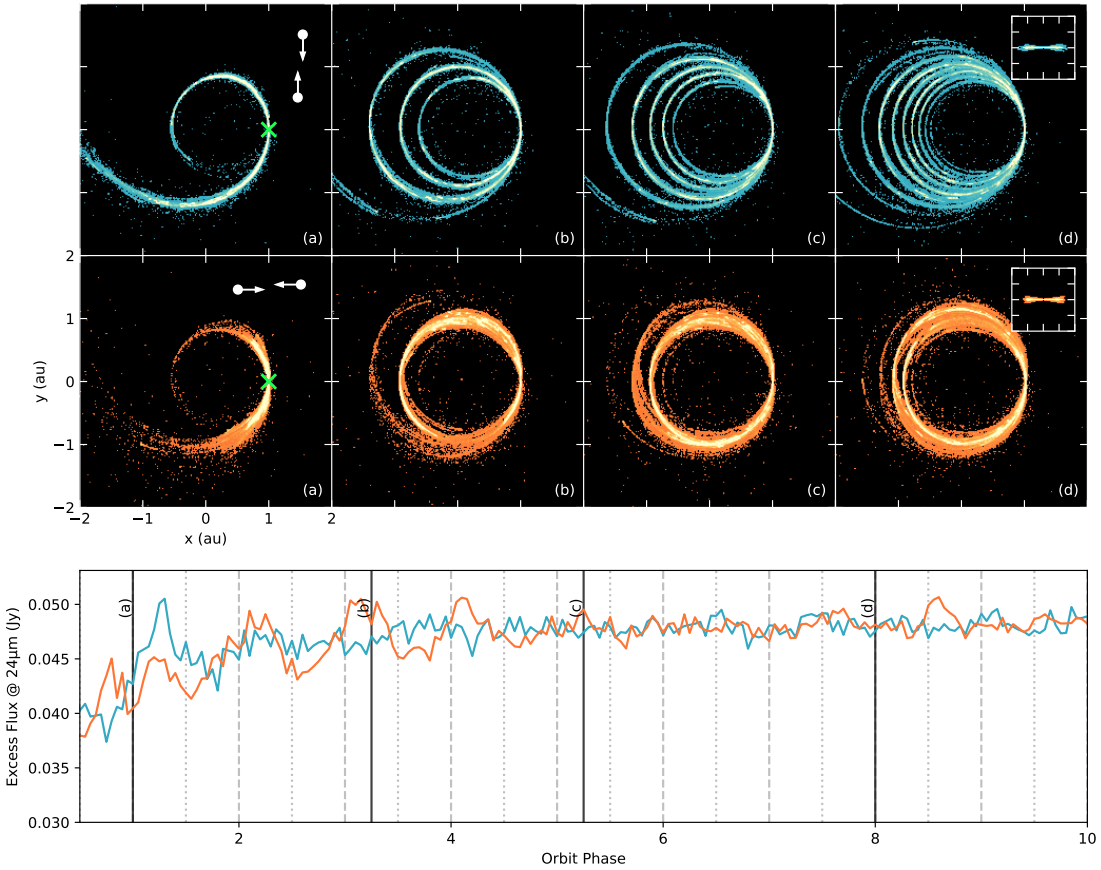

Figure 3.8: Same as in Fig. 3.7 but now with sim 90 in table A.1 which is a collision between two $0.1\mathrm{M}_\oplus$ embryos at 10 $\mathrm{km\ s^{-1}}$ with an impact parameter of 0.8. The flux is by a factor of ~ 10 as the vapour mass ejected is $1.9 \times 10^{-3}\mathrm{M}_\oplus$ instead of $3.34 \times 10^{-2}\mathrm{M}_\oplus$.

For sim 88, the distribution of vapour parallel to the remnants post-collision mean the velocity kicks will mostly align with the initial progenitor velocity vector with the opposite orientation to sim 8. This is why we see similar structures but for opposite orientations for the simulated disks shown in Fig. 3.7 and Fig. 3.8.

Figure 3.9 shows the initial semi-major axis distributions for the different orientations in both Fig. 3.7 and Fig. 3.8. The semi-major axis of particles are determined at $t = 0$ in the N-body code, and are derived from adding the velocity kick (determined from the pass over of data between the SPH simulations and N-body code) to the circular orbit of the progenitor. A clear difference is observed in the distributions of vapour condensates between the different orientations, and is present in both examples of sim 8 and 88. When we look at Fig. 3.1 and Fig. 3.5, we can see that the vapour is not distributed isotropically for sim 8 and 88, but the vapour. is ejected in a preferred direction(s). The distribution of velocity kicks cause this anisotropic distribution of vapour. Therefore, the orientation of the collision will determine the direction(s) of where the majority of vapour will be given velocity kicks. The direction and magnitude of a velocity kick will determine how much the new orbit of a vapour condensate will differ from the circular orbit of the progenitor orbit. For a given magnitude of velocity kick, the largest change in semi-major axis happens when the direction of the velocity kick is parallel with the initial velocity and when the initial velocity is at the maximum, hence at the perigee (any position in on a circular orbit). Jackson et al. (2014) goes into detail in how orientation of the velocity kick will influence the resulting orbit. For sim 8, the orientation shown in the orange disk of Fig. 3.7 means vapour condensates are preferentially launched along a direction that is parallel to the velocity of the progenitor. Vapour condensates are launched perpendicular to the progenitor velocity in the blue disk.

b) Flux Evolution

The total flux evolution of the disks is shown below the snapshots in both Fig 3.7 and 3.8. The colour of the flux evolution matches the snapshot colour (blue for the impact oriented along the orbit and orange for the impact oriented perpendicular to the orbit). At $24\mu\mathrm{m}$, we find a similar overall flux for the different orientations of the same collision. The disks generated from different orientations of the same collision contain the same vapour condensate mass, therefore similar overall flux levels are to be expected.

For the head-on equal-mass impact orientated parallel to the orbit (blue line) shown in Fig.

3.7, we find short term variation (wiggles) up to ~ 10 orbits after the collision. This short-term variation is similar to that seen in extreme debris disks like ID8 and P1121 (Meng et al., 2015; Su et al., 2019). However, the short-term variation does not appear when the impact is rotated perpendicular to the orbit (orange line). Again the difference in behaviour between the two collision orientations is due to the difference in spatial distribution. The distribution of orbital parameters (semi-major axis, eccentricity, inclination, etc) for vapour condensates is smaller in the blue disk compared to the orange disk. In the blue disk, the distribution of orbital parameters leads to the disk being optically thick at the collision point and anti-collision line for many orbits, reducing the flux when the progenitor was expected to pass through these points. For the orange disk, the distribution of orbital parameters means the disk shears out quickly and the disk is not optically thick at the collision point/anti-collision line after 1-2 orbits.

In comparison we see no sustained short-term variation in the flux evolution of the equal-mass grazing collision shown in Fig. 3.8. If we only consider the spatial distribution, we would expect to see the orange disk shown in Fig. 3.8 to behave similarly to the blue disk shown in Fig. 3.7 but this is not the case. The difference is the total mass ejected as vapour. For sim 88 shown in Fig. 3.8, the escaping vapour mass was $3.79 \times 10^{-4} \mathrm{M}_{\oplus}$. For sim 8 shown in Fig. 3.7, the escaping vapour mass was $6.64 \times 10^{-3} \mathrm{M}_{\oplus}$. Optical thickness of the disk is dependent on how dense the disk is. The reduced mass released from sim 88 due to the projectile only partially colliding with the target means that at 1 au, the resulting disk becomes optically thin quickly after the collision has taken place and a maximum flux ($\sim$10 times less) is reached by two orbital phases.

c) Producing Wiggles

It is possible for sim 88 to show short-term variation if placed closer to the star because this will lead to a reduction in the distribution of the orbital parameters (Fig. 3.9 and 3.10) and therefore increase the optical thickness of the disk, causing the debris at the collision point and anti-collision line to be optically thick for more orbits. However, if this collision occurred much closer to the star, the relative difference between the optical thickness of material passing through the collision point/anti-collision line is reduced and wiggles will not appear. Though this is for face-on disks, for inclined disks wiggles can still arise from material passing through the disk ansae. There will be a defined range of orbital parameters and orientations for each collision where the short-term variation in the flux evolution can occur.

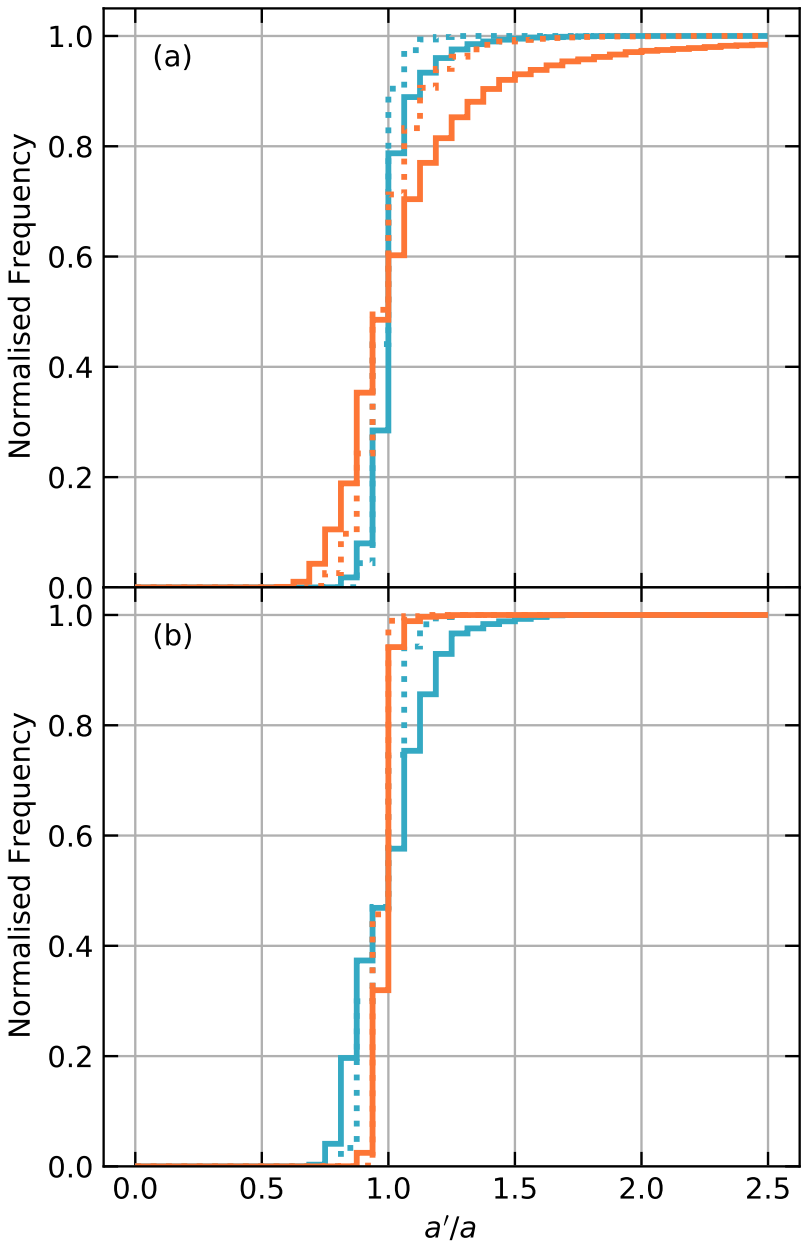

Figure 3.9: Cumulative histograms showing the distribution of semi-major axis values for dust post-collision for a collision between two 0.1 $M_\oplus$ embryos at 10 $\mathrm{km\,s^{-1}}$ at (a) $b = 0$ (sim 8) and (b) $b = 0.8$ (sim 88), normalised by the semi-major axis of the progenitor. The colour denotes the rotation of the collision, same as in Fig. 3.7 and 3.8. Collisions at 1 au are solid lines while dotted lines are collisions at 0.3 au. The orientation will change the distribution of orbital parameters. For a given collision, distance from the star will also dictate the distribution of dust, with larger range of semi-major axis values available at larger distances.

There are a few other ways to increase the optical thickness of the disk so that a grazing impact like sim 88 could produce sustained wiggles in the orange flux shown in Fig. 3.8 similar to the blue flux in Fig. 3.7: 1) reduction in the impact velocity which will reduce the range of velocity kicks; 2) or an increase in total mass involved in the collision. We have to be mindful though that escaping vapour mass and the velocity dispersion of the escaping vapour are not independent from each other. Increasing the impact velocity will increase the escaping vapour mass but will also increase the velocity dispersion. Because high b collisions are inefficient producers of escaping vapour mass, to produce the oscillations in the flux similar to that seen in Fig. 3.7, the distance at which the collision can take place from the star is more limited than head-on collisions.

Head-on collisions are the most efficient producers of escaping vapour, therefore, can have a wider range of impact velocities and hence distances from the star which the short-term variation in the flux evolution can occur. One way to increase the escaping vapour mass but keep the impact velocity the same is to increase the mass involved in the collision. But increasing the mass involved in the collision increases the mutual escape speed of the collision. The impact velocity needs to be greater than the mutual escape speed in order to eject vapour condensates and place the dust on orbits that are not bound to the collision remnants.

This will also limit the distance from the star at which giant impacts can occur at and reproduce the short-term variation seen in the flux from the resulting disk. A coherent clump of material will not be formed if a giant impact takes place where the mutual escape speed is greater than or equal to the Keplerian velocity at that position as material ejected will be placed onto extremely wide distributions of eccentricity and semi-major axis values (Wyatt et al., 2017), with a portion of the material ejected from the stellar system.

Collisions closer to the star will be more likely to produce the short-term variation in the flux evolution. Nevertheless, the evolution of impact-produced debris closer to the star will evolve much quicker than a disk further out. Therefore, it becomes increasingly difficult to observe such oscillation behaviour if the impact-produced debris disperses after a few tens of orbits. There is a sweet spot between all the parameters we have discussed, with the observability of oscillatory behaviour arising in disks formed from giant impacts decreasing as we move away from this sweet spot.

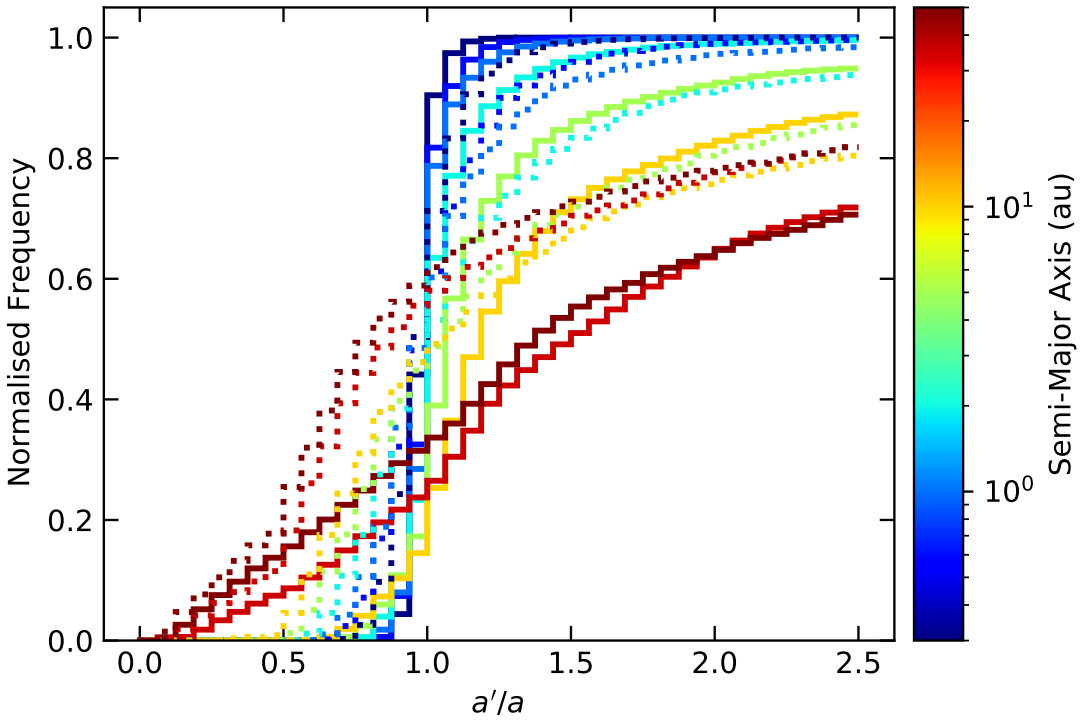

Figure 3.10: Cumulative histograms of the semi-major axis distributions of the initial vapour condensates from a head-on collision between two $0.1\ \mathrm{M}_{\oplus}$ embryos at $10\ \mathrm{km\ s}^{-1}$ (sim 8) normalised by the semi-major axis of the progenitor. The colour of the line denotes the semi-major axis of the progenitor. Solid dotted lines show the collision orientated parallel and perpendicular with the velocity vector of the progenitor respectively.

3.4 Discussion

In this chapter, we have demonstrated how short term variations ("wiggles") in the flux evolution can be expressed or suppressed in an extreme debris disk formed from a specific giant impact.

3.4.1 Progenitor Position

For a given collision, the radial position of the progenitor orbit will also affect the orbits of the escaping material and thus the production or suppression of "wiggles". For example, a collision that takes place further from the host star will have a wider range of parameter space to fill because the effect of the gravitational potential well is reduced (Fig. 3.10). In other words, we find that impacts that occur close to the host star result in the escaping dust being placed onto a narrow range of semi-major axis about the progenitor's semi-major axis. While impacts that occur at larger stellocentric distances have escaping debris in a wider range of semi-major axis. (Note that Fig. 3.10 was constructed under the same impact velocity at different stellocentric distances; therefore the result does not take into account the likelihood of such an impact at that location due to its orbital Keplerian velocity). The widening of the semi-major axis distribution as the collision moves further away from the star leads to the reduction and eventual disappearance of any "wiggles" in the flux evolution. This is because that the "wiggles" rely on the vapour condensates being a coherent clump as it passes through the collision point and anti-collision line, meaning that oscillations only happen when the there is a narrow distribution of dust in the semi-major axis.

If the distribution of eccentricities in the impact-produced debris is too wide, and therefore the semi-major axis range is large, the dust will Keplerian shear out on a timescale before oscillations can be observed. At large distances from the host star, we find the impact orientation becomes more influential because the semi-major axis distribution is broader. This is because the velocity kick of the vapour condensates only changes direction while the Keplerian orbital velocity becomes smaller. If the material is optically thin, the broader semi-major axis distributions would then display a variety of dust temperatures. A change in orientation the could lead to a change in the dust temperatures as seen, for example, by the red solid and dashed lines in Fig. 3.10. As the observed flux is sensitive to the dust temperature, the same collision but with different orientations could look very different when observed. For collisions occurring at large semi-major axis, this effect would be very pronounced.

3.4.2 Orientation Probability

Wiggle behaviour is also sensitive to the orientation of the impact relative to the progenitor orbit. The effect of varying the orientation is dependent on the initial vapour velocity distribution of the impact. We have shown in Fig. 3.5 how the initial vapour velocity distribution for many impacts varies with impact parameter and mass ratio. For an impact which creates enough escaping vapour and occurs close enough to the star so the Keplerian speed is large compared to the velocity dispersion (a coherent clump can form), and all orientations are equally likely then there will be an orientation for a given impact that will produce "wiggles". However, if the orientation probability distribution is skewed (for example, impacts parallel to the progenitor orbit are more likely than perpendicular to the progenitor orbit for some dynamical reason) then depending on what orientations are favoured, wiggles will be expressed or suppressed (Fig. 3.7 and 3.8). Oblique impacts are more likely to occur than head-on collisions (Shoemaker, 1962), hence if the orientation distribution is skewed to favour forming "wiggles" from ejecta launched perpendicular to a collision (head-on collisions) then "wiggles" are less likely to occur.

3.4.3 Dust Survivability

The observability of an extreme debris disk is dependent on both how bright it is and how long the dust within the system survives. Up to this point we have focused solely on the initial disk made from vapour condensate and have ignored dust generated by the intermediate boulder population, but in order to discuss lifetime we must consider all of the mass available to generate observable dust. As a reminder to the reader we are considering a single energetic giant impact between two planetary embryos. This impact has occurred as a result of planet formation and is a growth generating impact. For simplicity let us consider a head-on impact like simulation 8. This impact results in one significant remnant, some vapour ejected in a disk perpendicular to the impact, and non-vapour debris and melt. It is this non-vapour ejecta that we will call the boulder population. Initially, the vapour, the boulder population, and the largest post-collision remnant are all on similar orbits, however, the vapour and the boulders do have velocity perturbations as a result of the impact that place them on slightly different orbits.

In this work we assume that the vapour condenses into a small characteristic size immediately. Because of the small condensate size the vapour population is observationally visible immediately with very little, if any, collisional evolution. This means that the dust generated by

the vapour becomes visible to the observer while it is still on similar orbits to the largest remnant - the vapour generated dust appears while it is still in a "clump". The boulder population, however, is most likely not visible immediately. Although we do not have the resolution in our SPH simulations to confidently determine the full size distribution of the non-vapour post-collision remnants we do have the resolution to identify the second (and third) largest remnants. In simulation 8 the second largest remnant is about 100 km and previous work on asteroid families indicates a size distribution with a 3.5 index power-law. This means that the majority of the mass will be in the larger end of the power-law. Assuming that a traditional collisional cascade is initiated by orbit crossing between the boulders it will take some time for enough collisions to occur to generate an observable dust population. Thus, we assume that by the time the orbits of the boulder population have spread out and started crossing they will no longer be in an identifiable clump. Using this logic we have come up with a simplified model to estimate the lifetime and observability of debris produced by the giant impact modeled in simulation 8.

We can make an estimate of how long we would expect escaping material from an isolated giant impact to last by assuming the escaping debris forms a debris disk fed by a quasi-steady state collisional cascade. Using equation 15 from Wyatt (2008),

$$f/M_{\rm tot} = 0.37 r^{-2} D_{\rm bl}^{-0.5} D_c^{-0.5}, \tag{3.2}$$

we can find the fractional luminosity f (the luminosity of the debris disk divided by the luminosity of the host star), where $M_{\rm tot}$ is the total escaping mass, r is the position of the disk in au, D_c is the size of the largest object in km, $D_{\rm bl}$ is the blowout size in μm. In following this method we have made the following simplifications/assumptions: 1) the debris disk is an axisymmetric narrow ring; 2) there is an underlying population with the largest size bin set at D_c; 3) the disk follows the typical size distribution of a normal debris disk/collisional cascade ($dN \propto a^{-3.5}$), and 4) material is instantly lost once below the blow-out size of the star and no longer contributes to the flux.

If we assume $f = 0.01$ is required to produce an observable debris disk and calculate $M_{\rm tot}$ for a traditional debris disk taking reasonable values of 60 km and 0.8 μm for D_c and $D_{\rm bl}$ respectively, then at 1 au, around a solar-type star, equation 3.2 gives us a mass of $1.87 \times 10^{-1} {\rm M}_{\oplus}$. This result means that a giant impact would need to release at least a Mars mass amount of material into the surrounding environment to form a detectable extreme debris disk. Assuming a standard collisional cascade, the size of the largest boulders sets the lifetime of the debris disk, the larger the largest objects the longer the disk will last. We have shown in

Fig. 3.2 that giant impacts between planetary embryos will generally lose between a few to 10% of their mass as escaping vapour. If we instead assume that the escaping vapour mass is solely responsible for the debris disk (assuming no underlying km-scale boulders) and thus fix $D_c = 100\mu\mathrm{m}$ then the total mass to create $f = 0.01$ at 1 au becomes 7.64×10^{-6} $\mathrm{M}_\oplus$. If we assume a more conservative size distribution for the condensed dust between mm-cm the mass needed might be as large as 2.42×10^{-3} $\mathrm{M}_\oplus$. However, the lifetime of a disk populated by small vapour condensates would be much less than a traditional debris disk because there is no significant reservoir with which to resupply the dust. So although an extreme debris disk may be created almost instantaneously from a giant impact it may be fleeting and thus difficult to detected.

As mentioned in the first paragraph of this section we would expect a combination of a vapour condensate debris disk and a traditional debris disk formed from the grinding of the km-scale boulders produced in the impact. We would expect the vapour condensate debris disk to be brightest almost immediately after the impact because the maximum condensate size is small while we would expect the boulder debris disk to take many orbits to evolve into a steady state collisional cascade. This idea is expressed in Fig. 3.11 which shows how the fractional luminosity varies with time for a compound debris disk produced by sim 8 (Table A.1) for two values of the initial vapour condensate D_c, 100 $\mu\mathrm{m}$ and 100 mm, and maximum boulder size of 100km for a range of radial locations from 0.1 au to 10 au. In this model we assume that the visible vapour condensate debris disk is formed immediately while the traditional boulder generated debris disk takes 100 dynamical times/orbits to develop and create a quasi-steady state collisional cascade. In addition, we are assuming for simplicity, that the two dust populations do not interact with each other.

To construct figure 3.11 we begin with the total escaping mass from the result of the SPH simulation. In sim 8, the escaping vapour mass is $6.64 \times 10^{-3}\mathrm{M}_\oplus$ and the escaping non-vapour/boulder mass is $4.5 \times 10^{-2}\mathrm{M}_\oplus$ (Tab. A.1). Each curve is calculated by using eqn. 3.2, with the mass varying with time as:

$$M_{\mathrm{tot}}(t) = M_{\mathrm{tot}}(0)/[1 + (t - t_{\mathrm{stir}})/t_c] \tag{3.3}$$

from Wyatt (2008), where,

$$t_c = 1.4 \times 10^{-9} r^{13/3} (dr/r) D_c Q_D^{*5/6} e^{-5/3} M_*^{-4/3} M_{\mathrm{tot}}^{-1}, \tag{3.4}$$

dr/r is the width of the disk which is set to 0.5, Q_D^* is the planetesimal strength assumed

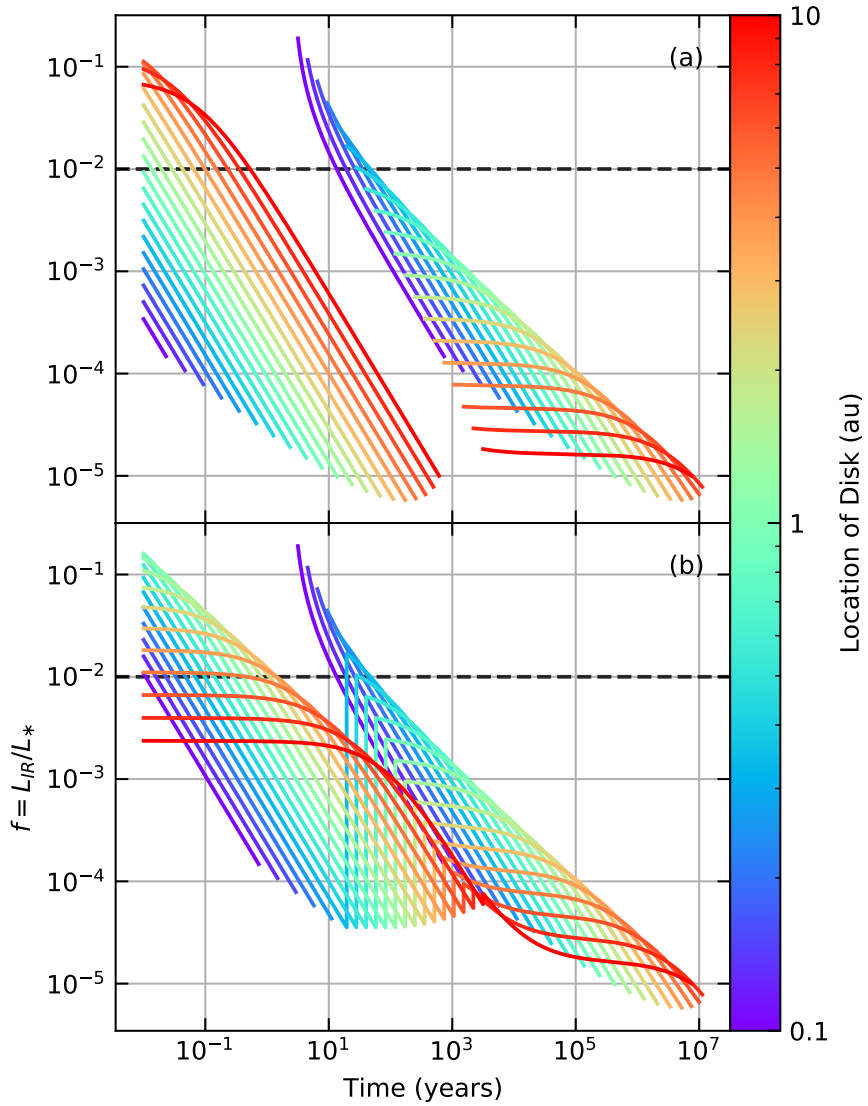

Figure 3.11: Evolution of fractional luminosities of compound debris disks with maximum initial grain sizes of: (a) 100 μm, and (b) 100 mm at t=0. Each sub-figure shows the time evolution for disk locations varying from 0.1 au to 10 au. Lines are plotted up to the detection limit at 24 μm (comparison of wavelength dependent limits shown in Fig. 3.12). The mass of each disk is determined from a head-on collision between two 0.1 $M_\oplus$ embryos at 10 km s^{-1}. Initially the debris disk is assumed to be formed entirely from vapour condensate. After 100 orbits dust contributions from the rest of the unbound post collision mass is added to the flux. The black dashed line, $f = 0.01$, is the minimum fractional luminosity limit for extreme debris disks. This shows us that the vapour and boulder populated disks will only have a short-time period where they would be classed as extreme debris disks.

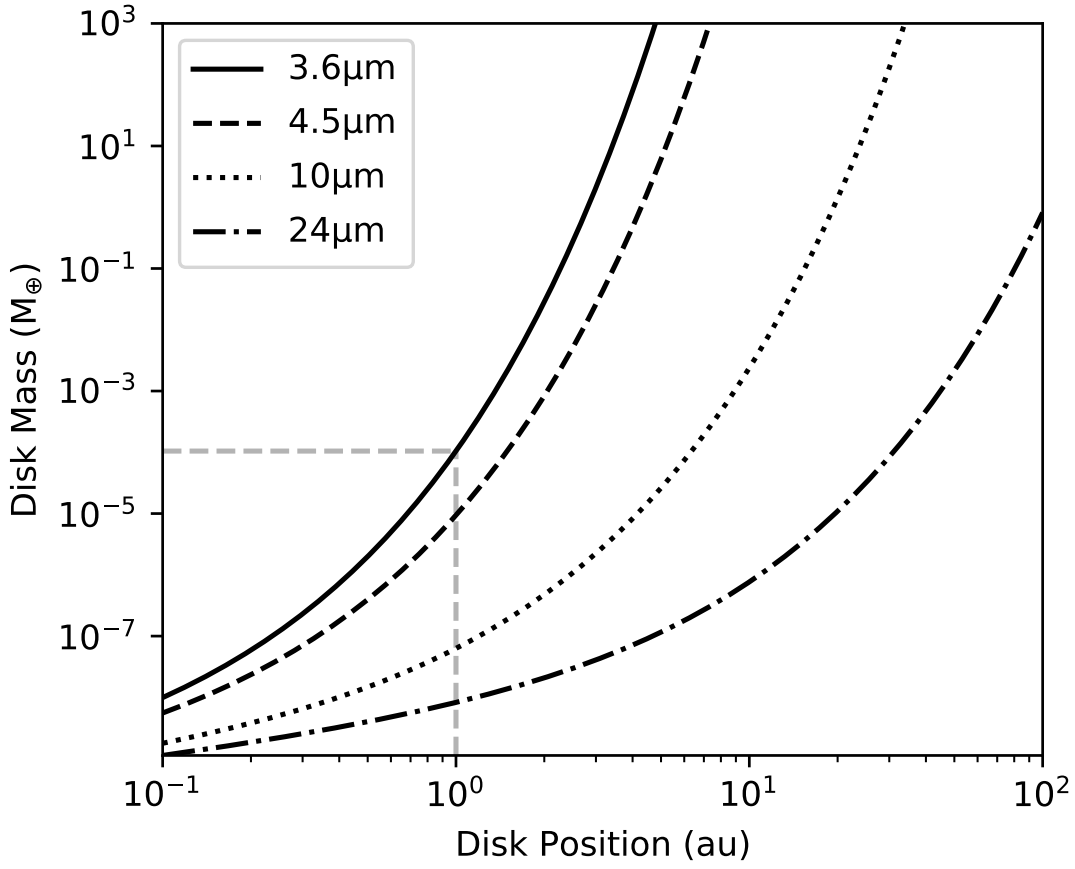

Figure 3.12: The minimum disk mass needed to observe a debris disk around a Solar-like star at varying disk positions. The lines correspond to different wavelengths of calibration limited fractional luminosity calculated assuming an excess ratio, $R_v = F_{v\mathrm{disk}}/F_{v*}$, of 0.03 (Wyatt, 2008). Disk masses assume a maximum size of 100 μm in the disk. The gray dashed lines intersect the 3.6 μm line to show the minimum mass needed to observe a debris disk at 1 au. For Spitzer missions which observe at 3.6 μm and 4.5 μm, dust created from embryo collisions is unlikely to be observed past 3 au as a substantial amount of mass will be needed.

to be 150 J kg^{-1}, e is the mean planetesimal eccentricity determined from the eccentricity of the vapour condensates, and M_*, the central star mass, is one solar mass. The timescale of mass loss (t_c) starts when the destructive collisions occur which is determined by t_{stir}. For the vapour generated disks we assume destructive collisions between vapour condensates occur immediately $t_{stir} = 0$, while the boulder population has $t_{stir} = 100$ dynamical times. For $t < 100$ dynamical times we assume that the boulder population does not contribute significantly to the flux. The initial mass ($M_{\mathrm{tot}}(0)$) is the total vapour condensate/boulder mass bound to the star, any vapour condensate/boulder particle unbound ($e > 1$) is removed from the total mass.

Each curve is plotted until the fractional luminosity falls below the calibration limit needed to be observed at 24 μm for a given semi-major axis (Fig. 3.12). The calibration limit is set so that the excess flux, $R_v = F_{v\mathrm{disk}}/F_{v*}$ where $F_{v\mathrm{disk}}$ and F_{v*} are the flux from the debris disk and star respectively, has to be above 0.03. Using equation 11 from Wyatt (2008) we can determine the fractional luminosity detection limit, f_{det} for a debris disk at a given wavelength, λ, via,

$$f_{\mathrm{det}} = 6 \times 10^9 R_v r^{-2} L_* T_*^{-4} B_v(\lambda, T_*)[B_v(\lambda, T)]^{-1} X_\lambda, \tag{3.5}$$

where r is the distance to the disk from the star, L_* is the luminosity of the star, T_* is the blackbody temperature of the star, T is the temperature of the disk, B_v is the blackbody emission, and X_λ is a factor included to take account of the falloff in the emission spectrum at large wavelengths but it's 1 for 24μm. Figure 3.12 shows how f_{det} varies with disk mass and position for four different wavelengths: 3.5, 4.5, 10, and 24 μm. As radial distance increases the disk mass needed for detection increases as does the amount of escaping material that is unbound. This creates the positive inflection in the limiting f_{det} in fig. 3.11.

Now if we consider the results shown in fig. 3.11 starting first with the impact close to the star, we see that it results in an initially brief and faint vapour condensate disk followed by a break and a bright but quickly fading traditionally formed debris disk. In this case only the second boulder generated debris disk would be briefly considered an extreme debris disk ($f > 0.01$). If instead the collision occurred further from the central star at 10 au the situation is effectively reversed (red curves). The vapour generated disk is initially bright and in the case of 100 μm observationally classed as an extreme debris disk for a few years but fades three orders of magnitude in flux over the next 100 dynamical times or so until the slowly evolving boulder population produces a faint traditional debris disk that lasts for millions of years. Impacts that occur in the terrestrial region result in an intermediate outcome, resulting in initial disks that only last a few years at most. The boulder disks will appear afterwards. Increasing the initial

condensate size from 100 μm to 100 mm results in vapour disks that are observable for longer (due to a modest reservoir) with more vapour disks being classed initially as extreme debris disks. In addition, the disconnect between the vapour and boulder disks is removed except disks placed closer than $\sim$0.4 au to the star.

Note the results presented in fig. 3.11 do not allow any interactions between the two disks though the total flux from each of the vapour produced disk and the traditional boulder debris disk are included, however, the dust from the vapour disk does not interact with the boulder population dynamically. In addition, the debris disks produced from sim 8 do not stay bright for extended periods of time and although this is primarily due to the small amount of escaping mass available for the debris disk the simplifying assumptions discussed at the beginning of this section will also lead to the most efficient removal of dust. Namely, the dust is assumed to be in a fully formed axisymmetric disk, with an evenly distributed removal of material around the disk. But we know that this is not entirely accurate. After a giant impact, the initial escaping debris clumps will be asymmetric with collisions between debris more likely at the collision point and anti-collision line (Jackson et al., 2014; Kral et al., 2017). This asymmetry will make the evolution of the disk significantly faster than a axisymmetric disk. Therefore, we would expect the lifetime of the boulder population to be shorter than that seen in Fig. 3.11. However, we expect it still takes many interactions for the boulder population to grind down and produce a detectable amount of small grains, thus, we should still see a period of time between the vapour disk declining in flux and the boulder disk then increasing in flux. The asymmetry will also affect the vapour disk but because we have used a strength value, Q^*_D, an order of 1-2 magnitudes lower than what is expected for small grains (Benz & Asphaug, 1999), the lifetime of the vapour disks should largely stay the same.

In this model, the vapour disk has a lifetime which is not consistent with observed extreme debris disks. The disk around ID8 is expected to be approximately at 0.4 au and has a fractional luminosity above 1% for a time much longer than what the model expects in Fig. 3.11. We know this mass cannot be sustained by a large reservoir of boulders due to the sharp decline in flux in 2013 and 2015 following a large increase in flux in 2012 and 2014 (Su et al., 2019). Therefore, there must be a mechanism which sustains the small vapour grains which we are not accounting for. One way to allow the vapour disk to survive for longer is to have a mechanism which will protect grains at, and smaller than, the blow-out size. Future work is needed to understand what this mechanism could be.

In presenting this idea of a compound debris disk we are making the assumption that the two components of the flux excess are expected to behave differently dynamically. The traditional boulder debris disk forms from an azimuthally distributed collisional cascade not by a single large event that results in some orbital coherence of the debris at particular locations in the disk. Thus, we would expect any observed short term variations like the "wiggles" seen in extreme debris disks ID8 and P1121 are most likely produced by the vapour condensate disk only. However, it is possible that under some particularly active scenarios the boulder population may also be able to produce short term variations.

In this section we have only presented the flux versus time of one collision (sim 8), however, Table A.1 and A.2 show the collision outcomes are diverse. An increase or decrease in the debris mass, which we have found to vary between 1×10^{-4} to one Earth mass in our simulated collisions, will lead to an decrease/increase in the initial fractional luminosity but overall the evolution of the disks will be similar. Decreasing the mass (vapour/boulder or both) will lead to some disks at large orbital distances in Fig. 3.11 becoming unobservable as there is not enough mass in the disk. Meaning that some of these giant impacts would not be observable at 24 μm but it would not mean that the giant impacts did not occur. Note that disks at large orbital distances are observed at longer wavelengths. This changes the observability threshold and might mean disks that are not detectable at 24 μm are detectable at longer wavelengths.

3.5 Conclusions

This study focused on the early behaviour of extreme debris disks formed from giant impacts between planetary embryos. The goal was to numerically model the formation of a vapour condensate debris disk along with any short-term variations or "wiggles" which could be linked to observations of variable extreme debris disks such as ID8 and P1121. We constructed a hybridised numerical model using SPH (modified version GADGET-2) to calculate the energetic impact between planetary embryos and determine the distribution of impact induced vapour. We then simulated the global evolution of the vapour condensed dust using an N-body code.

From the giant impact simulations we determined the dependence of vapour mass on impact energy creating a first-order scaling law that can be used in future work instead of the computationally costly numerical impact simulations. We also showed that a greater percentage of

vapour mass is ejected from the projectile than the target as you move towards lower mass ratios and larger impact parameter values, with the difference becoming more profound at larger $Q_{\rm R}/Q^*_{\rm RD}$. The material that escapes from the giant impact is preferentially launched from an impact and varies with mass ratio and impact parameter. Material is more likely to be launched perpendicular to the impact direction at larger $Q_{\rm R}/Q^*_{\rm RD}$ if the impact is head-on ($b = 0$) with no variation with mass ratio, while for grazing impacts with large impact parameter ($b = 0.8$) material is launched parallel to the impact direction, with the preference to launch parallel becoming larger as the mass ratio becomes smaller. For intermediate impact parameter values ($b = 0.4$) material is launched in all directions.

Orientation of a giant impact and the subsequent vapour distribution with respect to the progenitor orbit plays a large role in whether short-term variation is seen in extreme debris disks or not. We can remove the short-term variation seen on one of our extreme debris disks through orientating the impact differently so that the vapour condensates have a wider distribution of eccentricites and semi-major axis values. This leads to material shearing out more quickly, meaning there is no coherent clump of material that is optically thick at the collision point and anti-collision line after 1-2 orbits.

Finally, we discussed the lifetime of giant-impact induced disks. We modeled giant impact induced disk as a compound disk made of two distinct populations, vapour condensate and dust created by grinding boulders produced in the original impact. The evolution was calculated through semi-analytical means following Wyatt (2008). In our simple evolution model we assumed that the vapour condensate disk was produced immediately and that the traditional boulder debris disk took 100 dynamical times to develop. With these parameters we found that vapour production alone would not guarantee a classification as an extreme debris disk. In fact depending on the location of the impact, the disk formed from the grinding of the boulder population was the only component that would be observationally characterised as an extreme debris disk. In addition, it was clear that in most cases the disks were only visible for very short periods of time, making observational detection difficult and strongly dependent on the nature of the impact and the amount of vapour and boulder mass produced.

This work suggests that giant impacts produce a complex compound debris disk that is in most cases variable and transient. The current small numbers of detections of young extreme debris disks do not mean that giant impacts are not occurring but that we have been incorrect about their observability.

4

Post-Giant Impact Planetesimals Sustaining Extreme Debris Disks

Abstract

Extreme debris disks can show short term behaviour through the evolution and clearing of small grains produced in giant impacts, and potentially a longer period of variability caused by a boulder population made up of planetesimals formed from giant impact ejecta. In this chapter, we present results of numerical simulations to explain how a boulder populated disk can supply an observed extreme debris disk with small grains. We simulated a sample of giant impacts from which we form a boulder population. We then use N-body code REBOUND to evolve the planetesimals spatially and collisionally. We adopt a simplistic collision criteria in which we set destructive collisions between planetesimals to only need to exceed $2V^*$ (where V^* is the catastrophic impact velocity), with merging collision occurring when the impact velocity falls below $0.1V^*$ and bouncing impacts occurring in between these values. We find that for some configurations, a boulder populated disk can produce a substantial amount of dust to sustain the observed disk. We show how the collision rate evolution is consistent across all parameters varied. We find that the semi-major axis changes the mass added to the observed disk substantially with the orientation of the impact varying the mass less so.

4.1 Introduction

Most giant impacts produce a considerable amount escaping material (most giant impacts are not perfect merging events; Leinhardt & Stewart (2012); Genda et al. (2017)). It is common in these large impacts for a significant amount of the escaping mass to be vaporised (Carter et al., 2020; Gabriel & Allen-Sutter, 2021). Vaporised mass is favoured to explain EDD systems as vapour can quickly condense into small fragments/spherules ranging from microns to centimetres in size (Johnson & Melosh, 2012). Vapour condensate can explain how a disk can go from a quiescent state to an active state extremely fast as observable material is formed almost instantaneously after an impact. If the make up of post-impact debris is mostly small grains initially, it can also explain how a disk can then quickly transition back into a quiescent state as most of the condensate will be lost through radiation processes by the star on short-timescales (Su et al., 2019). Many EDDs exist around stars with ages within the terrestrial planet formation age, 10-200 Myr (Meng et al., 2015, 2017; Moór et al., 2021). The overlap in timescale supports the giant impact explanation as the main cause for EDDs. However, it should be noted that a few EDDs exist around older stars (Melis et al., 2021). Explanations for such systems include a potential late stage instability, causing late time giant impacts. Another possible explanation is a wide binary causing instabilities in the system (Zuckerman, 2015; Moór et al., 2021).

If the initial EDD is observable mostly through small grains formed from vapour as we saw in chapter 3, the question then becomes how are these disks sustained. Current debris disk models suggest that a disk made of just small grains would dissipate on timescales shorter than their observed lifetimes (Wyatt, 2008). Current models do not support shielding of grains smaller than the blowout size in optically thick clumps, which would increase the lifetime of the disk even when the geometry of giant impact produced debris results in an increase in collisional activity (Jackson et al., 2014). Another hypothesis is that two debris populations are formed by a giant impact: one population being mostly small grains formed from vapour condensate, and the other population being larger boulder objects formed from the escaping melt material. If the melt material formed a significant background population of boulders, these objects can then form the top end of a collisional cascade which can supply the disk with small grains over time. ID8 would suit such a scenario, as after multiple peaks and dips in its light curve, after 2017 there is a steady rise in excess flux suggesting a gradual release of small grains into the system (Su et al., 2019).

The goal of this chapter is to further understand the two population model of small grain production after a giant impact has occurred. Our focus will be on the boulder population made up of large planetesimals formed post-impact, and its collisional evolution in the stellar system. In section 4.2 we outline how the simulations were set up for giant impacts using a smoothed particle hydrodynamical (SPH) code, and the N-body set up for spatially and collisionally evolving the disk post-giant impact. In section 4.3 we present the results of our simulations through exploring the parameter space to see how the evolution of the boulder population varies. Section 4.4 discusses how our results affect the observability of an EDD as well as the limitations of our study. We summarise our conclusions in section 4.5.

4.2 Methods

Below we summarise the SPH simulations we conducted, how fragments post-collision are determined, and how the N-body simulations were set up from the planetesimal population derived from the SPH simulations.

4.2.1 GADGET-2 Simulations

Extreme debris disks can be formed from the debris of giant impacts. Since extreme debris disks are usually located around the terrestrial region of young stars (Moór et al., 2021), we focus on simulating impacts between rocky embryos. We again used GADGET-2 to simulate the giant impacts with details of the simulation setup outlined in section 2.2. Each embryo was equilibrated using velocity damping and locked to a set specific entropy and then each embryo was allowed to equilibrate without any restrictions. The values for each embryo are given in Table B.1.

In this study, we need to know to a reasonable accuracy the number of planetesimals formed post-impact in order to ascertain the mass in the planetesimal disk. Within the SPH simulations, we find a number of gravitationally bound groupings of escaping particles. The number of groupings will depend on the particle number resolution. We assume these groupings will form planetesimal sized objects. The planetesimals defined from groupings of SPH particles will fill the large mass end of the total planetesimal mass distribution. The number of smaller planetesimals is estimated from the combined mass of the non-grouped escaping particles. In order to resolve a significant number of planetesimals forming in our chosen simulations, we

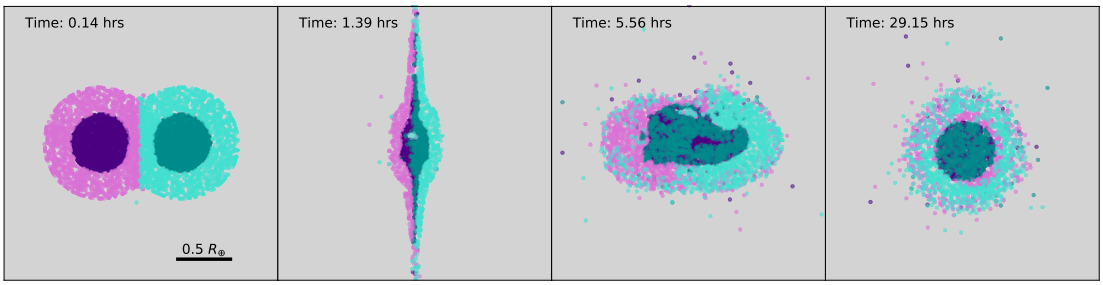

Figure 4.1: Four snapshots of giant impact 1 from Table 4.1 with a cut in the z-direction to observe a midplane slice. The head-on impact is between two $0.1\ \mathrm{M}_\oplus$ planetary embryos at $10\ \mathrm{km\ s^{-1}}$. Time for each snapshot is given in the top left corner of each subplot. Core material is shown in darker colours while mantle material is shown in lighter colours. The core and mantle are iron and forsterite respectively.

simulate two giant impacts with a total particle number of 4×10^5 and one giant impact with a total particle number of 4×10^4. We chose three unique giant impacts in order to understand how different impacts effect the outcome of extreme debris disks. The simulated impacts are listed in Table 4.1 with the collision parameters and outcomes. Fig. 4.1 shows the evolution of giant impact 1. From these impacts we determine a population of escaping planetesimals that will feed the observed disk over time.

4.2.2 Determining Planetesimal Distribution

The focus of this chapter is to understand the effect that planetesimals formed from giant-impacts have on the evolution of an extreme debris disk. In order to do so, we first must determine the planetesimals/fragments that form from the post-impact debris. The largest planetesimals will be resolved as bound clumps of particles in the SPH simulations. Using the method outlined in section 2.2.1 of Watt et al. (2021) and in section 2.2.3.a) we recursively find gravitationally bound groupings of five particles or more. This gives us a list of large remnants found post-giant impact which will also include planetary embryo(s) if the collision was not super-catastrophic. Once we have identified a remnant list from the SPH simulation, we can then define the planetesimal distribution generated from the giant impact. The planetesimal population is determined from methods outlined in section 2.3.2.d). In short, from the remnant list we define all but the largest remnant(s) as planetesimals and generate smaller planetesimals (non-grouped planetesimals) from the total mass of the non-grouped escaping SPH particles. We assume that planetesimals will only form from the total mass found in SPH particles with a vapour fraction of $< 10\%$. Any particle with a vapour fraction above 10 per cent we assume will form into smaller sized objects as the expanding vapour will limit the gravitational in-fall and reaccumulation of material and therefore ignore in this study.

After the total mass of non-grouped planetesimals has been defined, a size distribution must be set in order to generate a population of planetesimals. Debris disks typically have a size distribution of $n(D) \propto D^q$ (Wyatt, 2008), with q being determined to have a value between -3 and -4. A smaller value of q will lead to more mass being placed in larger planetesimals. Here we choose $q = -3$, instead of the typical value $q = -3.5$, as it will increase the number of planetesimals generated. Using a density of $3\,\mathrm{g\,cm^{-3}}$, the non-grouped planetesimal mass is used to generate a distribution of planetesimals according to the set size distribution, and an upper size set by the smallest planetesimal found as a well-resolved group. Overall, we have three

Table 4.1: Summary of giant impact set up and results from SPH simulations. $\mathrm{M_{tot}}-$ total mass in impact in Earth masses; $\mathrm{M_{proj}/M_{targ}}-$ mass ratio of projectile to target mass; $\mathrm{N}-$ number of particles used in the simulation; v_i- impact velocity in $\mathrm{km\ s^{-1}}$; $b-$ the impact parameter; $\mathrm{M_{lr}/M_{tot}}-$ mass ratio of the largest remnant to total mass in the simulation; $\mathrm{M_{sr}/M_{tot}}-$ mass ratio of the second largest remnant to the total mass in the simulation; $M_{\mathrm{plan}}-$ planetesimal mass formed in Earth masses.

Index	$\mathrm{M_{tot}}$	$\mathrm{M_{proj}/M_{targ}}$	N	v_i	b	$\mathrm{M_{lr}/M_{tot}}$	$\mathrm{M_{sr}/M_{tot}}$	M_{plan}
–	($\mathrm{M_\oplus}$)	–	(10^4)	($\mathrm{km\ s^{-1}}$)	–	–	–	($\mathrm{M_\oplus}$)
1	2.37e-01	1.00	40	10.0	0.00	0.697	0.007	5.82e-02
2	3.71e-01	0.47	40	11.4	0.42	0.654	0.195	4.13e-02
3	1.99e-01	1.00	4	15.0	0.00	0.376	0.000	5.83e-02

populations of bodies: 1) largest remnant (plus second largest remnant if the criterion is met), 2) large planetesimals defined from groupings of escaping particles in the SPH output ('resolved' planetesimals), and 3) the smaller ('unresolved') planetesimals which have an assumed power law size distribution with the total mass derived from the SPH output.

Finally, velocity kicks are given to the planetesimals. For the resolved planetesimals, the velocity kick is calculated from the SPH simulation by tracking the centre of mass velocity magnitude and direction. The method for generating the velocity kicks is outlined in section 2.3.2.d). Fig. 4.2 shows the distribution of v, ϕ and θ for the overall planetesimal (resolved and unresolved) in black and the escaping SPH particles of giant impact 1 in orchid. We find the distribution of ϕ and θ to match well but we note there is a slight difference in the velocity distribution. The difference is down to the unbound escaping SPH particles not having a symmetric log-normal distribution. Hence, while the mean of both distributions are the same, the median values are slightly different, with our generated planetesimals having a slightly smaller median value. For our study, the differences between the velocity distributions will have a minuscule effect on the overall result as the direction of the kick is what drives a large difference.

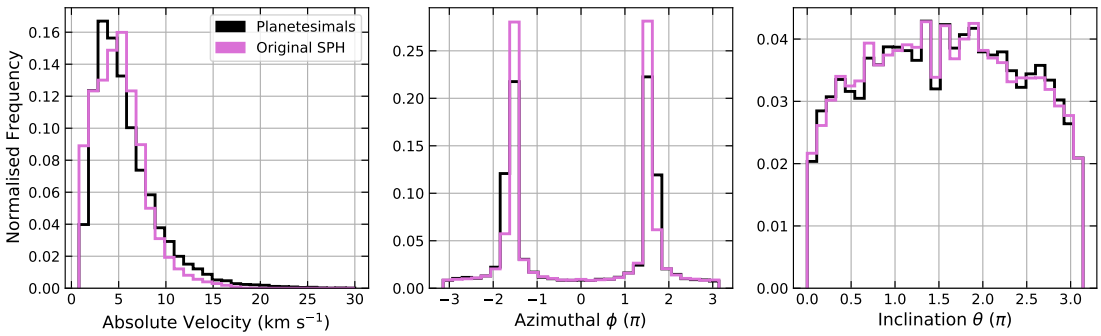

Figure 4.2: The distribution of absolute velocities (left), azimuthal ϕ (middle), and inclination (right) of the distribution of particles in the giant impact frame of reference. The escaping particles in the SPH giant impact simulation are shown in orchid and the planetesimals formed from the escaping particles are shown in black. The escaping particles and planetesimals shown are from giant impact 1 in Table 4.1.

4.2.3 N-body

To evolve the post-impact planetesimals, we used REBOUND (Rein & Liu, 2012), an all-purpose N-body code which allows for collision detection. Details for how REBOUND was used please see section 2.3.2. In our N-body simulations we vary the initial giant impact position between 0.3 au and 2 au around a star of 1 $M_{\odot}$, with the progenitor orbit (the orbit of the target planet in the giant impact) set to always be circular. The time-step we used between steps was 1/2000 of the orbital period of the progenitor orbit as at early times in the simulations all the planetesimals are clumped around the embryo remnant(s). A larger timestep would lead to an inaccuracy with the step calculation near the beginning of the simulation. We also found an insufficiently small timestep would lead to the collision point widening on shorter timescales leading to fewer collisions occurring.

The planetesimals are evolved for 10^4 orbits of the progenitor orbit with each simulation having a particle number resolution defined by the resolved planetesimals and unresolved planetesimal mass from the SPH simulations. The complete set of N-body simulations can be found in Table B.2. We assume that the planetesimals are non-gravitating, meaning the planetesimals only interact gravitationally with the central star and the planetary embryo remnant(s). For the larger planetesimals, gravitational focusing may play a role in expanding their collision cross-section therefore our assumption might lower the overall collision rate. Though the inaccuracy should only be an issue at late times, as the planetesimals will need time to self-stir to greatly alter any orbital parameters. Hence, at early times gravitational interactions between planetesimals can be neglected without significant loss of accuracy.

Once a collision is detected the catastrophic impact velocity, V^*, is calculated. We set a simplified collision outcome criteria dependent on v_i/V^*. The collision outcome criteria : 1) $v_i/V^* < 0.1$ the planetesimals merge, 2) $0.1 \leq v_i/V^* < 2$ results in a bouncing collision, and 3) $v_i/V^* \geq 2$ the collision is completely destructive and both planetesimals are destroyed. We allow the clump to initially evolve for 0.25 orbits before allowing collisions. The outcome criteria is described in full in section 2.3.2.b).

Our study focuses on the visible debris formed from planetesimal collisions post-giant impact. Tracking the most destructive collisions means that we are tracking the quickest path that the planetesimal mass has on influencing the debris disk formed after a giant impact. However, we will miss mass from partially erosive collisions over time so only tracking the most destructive collisions will lead to an underestimate of the mass which will grow over time. The

collision outcome does not take into account impact angle, hence all collisions are assumed to be head-on. The result of this assumption means greater numbers of destructive impacts than would otherwise occur. As steps are taken in straight lines, along with collision detection, the impact angle will differ from a more complicated integrator. Since the impact angle will vary from its true value, we decided to take the most extreme assumption with head-on collisions. The reasoning being that if an observable disk is not formed through this favourable set-up, then impact angle will not matter. The planetesimals are usually large with the smallest planetesimal in disk 13 having a radius of 49.6 km, meaning they are well within the gravity regime and not the strength regime (Holsapple, 1994; Ahrens & Love, 1996). Therefore, using the collisional outcome criteria we have set and adopting the catastrophic impact velocity from Leinhardt & Stewart (2012) is justified.

4.3 Results

An extreme debris disk formed from the escaping debris of a giant impact will vary depending on many factors. The initial dust formed from vaporised material is only expected to survive for a few orbits before being ejected through radiation pressure or other means (Su et al., 2019). Though we find that extreme debris disks can be observable for many orbits after a supposed giant impact has occurred. We showed in Watt et al. (2021) (chapter 3) that the vapour condensate formed initially after a giant impact can reproduce behavior and the flux increase in EDDs. Su et al. (2019) suggested that ID8 in 2017 had a steady increase in the excess flux associated with a collisionally active boulder/planetesimal population. In this work we aim to understand the collisional evolution of planetesimals formed after the giant impact to explain the extended lifetimes of EDDs. Here we focus on how a planetesimal population formed from the escaping ejecta of a giant impact can sustain an EDD through a collisional cascade. Our work is split into two sections, first we focus on modelling giant impacts through SPH simulations in section 4.3.1 and then we see how the planetesimal population collisionally evolves over time through N-body simulations in section 4.3.2.

4.3.1 SPH

In order to estimate the effect a collisional cascade of planetesimals on an EDD, we need to know the amount of escaping material that will form planetesimals post-giant impact. While there can

be many different configurations, we focus on just three different giant impacts. These giant impacts are outlined in table 4.1. These impacts were chosen as they produce a substantial amount of vaporised material to form an initial EDD, as well as having masses that would typically match planetary embryos in the early Solar System. An example impact is shown in Fig. 4.1.

We use two different methods to define a planetesimal population from the escaping ejecta: 1) particles that were found to be gravitationally bound together at the end of the simulation, and 2) estimating a planetesimal population from particles not found to be bound to any other well-resolved particle group. We outlined how we determine both these populations in section 4.2.2. The total mass for each giant impact is listed in Table 4.1. The main differences between each planetesimal population will be the distribution of velocity kicks. We discussed in Watt et al. (2021) (chapter 3) how the distribution of velocity kick directions differ between different giant impacts. The velocity kick distribution for impacts 1 and 3 are similar which is to be expected as the only difference between them is the resolution used and the impact velocity. Impact 2 differs more significantly in velocity kick distribution compared to impacts 1 and 3. We showed in Watt et al. (2021) and in chapter 3 how differing anisotropic distributions would affect the resulting EDD. We would expect the behaviour of the collisional cascade caused by impact 2 to differ from that of impact 1.

4.3.2 N-body

We simulated a total of 64 collisionally active disks for 3 different giant impacts. Most disks simulated focus on giant impact 1, with the other two impacts offering an insight into another parameter space. Fig. 4.3 shows four snapshots of a planetesimal disk placed at 0.5 au formed from giant impact 1. The evolution of the disk is similar to that seen in Jackson & Wyatt (2012); Jackson et al. (2014); Watt et al. (2021). It is expected that the distribution shown in fig 4.3 is similar to what is seen in Watt et al. (2021) (chapter 3) as most planetesimals have velocity kicks defined from the escaping ejecta the same as for the escaping vapour condensates.

To collisionally evolve the disk we assume collision outcomes between planetesimals divide into three categories: 1) merging collisions where one object is formed, 2) bouncing collisions where no material is accreted or ejected from either body, and 3) destructive collisions where both bodies are completely destroyed and all mass goes into ejecta. The collision outcome is dependent on the ratio between the impact speed and the catastrophic impact speed. From the

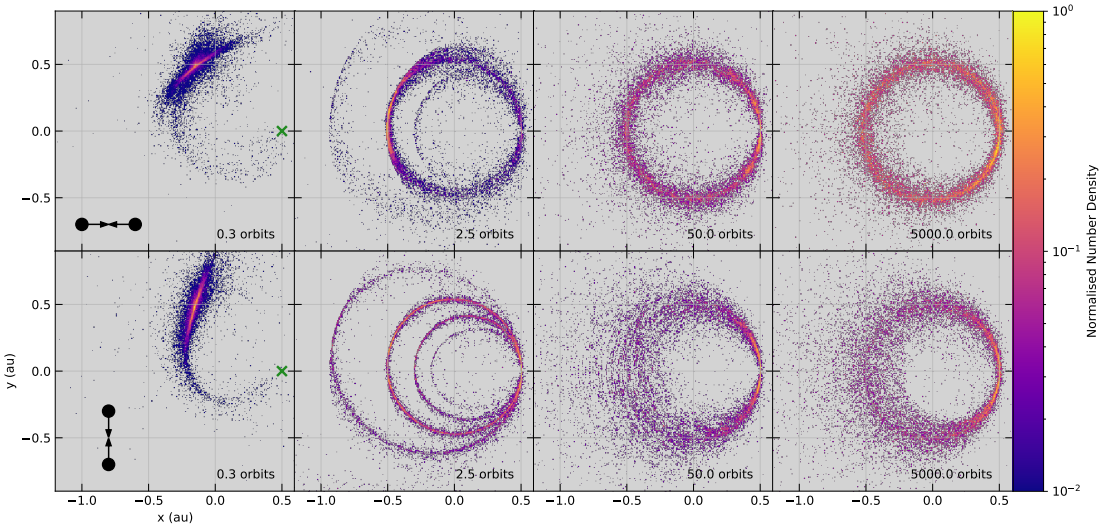

Figure 4.3: Evolution of disks 3 (top) and 13 (bottom) from Table B.2 with four snapshots after 0.3, 2.5, 50, and 5000 orbits of the progenitor orbit post-giant impact. Both disks formed from giant impact 1 from Table 4.1. The green cross marks the location of the giant impact in the first panel. The diagram in the bottom left shows the orientation of the giant impact. The colour denotes the normalised number density in each panel. Note: the maximum number density value in each panel differs.

collision outcome criteria, we are able to estimate the amount of mass that will be passed down to the small grain mass in the disk through the complete mutual destruction of planetesimals through high-speed impacts.

a) Impact Velocity Distribution

In our simplified collisional outcome prescription, the mass which is destroyed in planetesimal-planetesimal collisions is the mass that will form into a range of grain sizes that are observable. The complete destruction of planetesimals requires $v_i > 2V^*$. In Fig. 4.4 we show the normalised frequency of the impact velocities in planetesimal-planetesimal collisions normalised by the catastrophic impact velocity for 40 simulated disks formed from giant impact 1 with the impact having an orientation of 0.5π at 0.5 au. How the orientation of a giant impact can vary the disk structure is shown in fig. 4.3, the orientation refers to the direction of impact with respect to the progenitor orbit. An impact with 0π orientation has the impact occur in the same direction as the progenitor orbital velocity vector. The black line in fig. 4.4 shows the median distribution. For the median distribution, we find that 73 per cent collisions are destructive with the value ranging from 63 per cent to 84 per cent in individual runs. The range in the number of destructive collisions is caused by the random sampling of velocities when creating the distribution of planetesimals from the escaping ejecta in the giant impact. The difference seen between the percentage of destructive impacts can be explained by V^* having a mass and mass ratio dependence. More massive planetesimals will require either a faster impact speed and/or to impact into a more similarly sized planetesimal.

The mass of the planetesimals is set by the size distribution, therefore, there are far more lower mass planetesimals of similar sizes than larger planetesimals. With smaller planetesimals being more numerous and requiring less energy in the impact to be disrupted, there is a greater chance that smaller planetesimals are destroyed in the simulations. Fig. 4.5 shows the stacked distribution of all collisions recorded in each of the 40 simulations for giant impact 1 with orientation of 0.5π at 0.5 au. The stacked histogram splits the collision type for each planetesimal-planetesimal impact, and remnant-planetesimal impacts are always merging due the remnant being much more massive. We find that most impacts between planetesimals are relatively fast, above $3\ \mathrm{km\ s^{-1}}$, which can destroy two planetesimals with the same size of ~ 680 km. We do not see a uniform distribution however, the distribution looks to be more bimodal. The peak between $3 - 4\ \mathrm{km\ s^{-1}}$ is caused by collisions within the first orbit after the

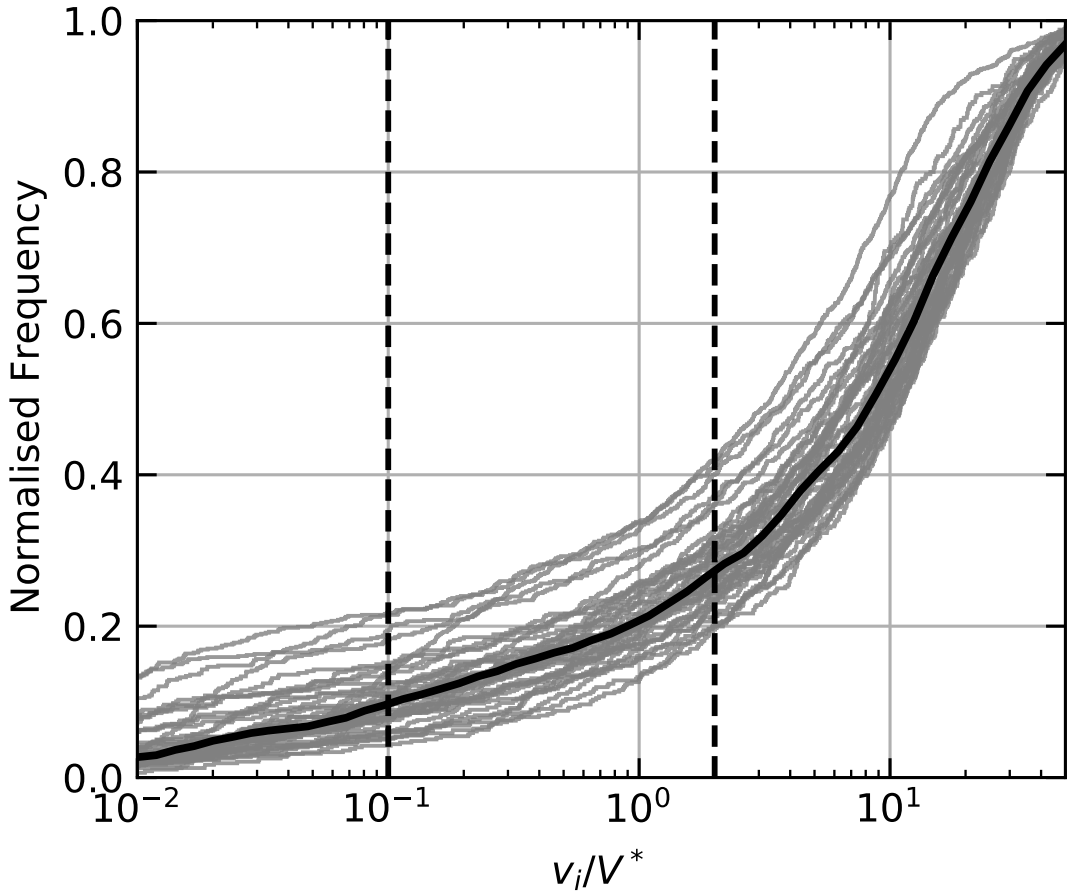

Figure 4.4: The cumulative distribution of v_i/V^* for disks 13 to 52 in Table B.2. The black line shows the median interpolated distribution. The black dashed lines separate the collisions which meet different outcomes; the left section is perfect merging, middle is elastic bouncing collisions, and right is fully disrupted.

giant impact, while 85.4 per cent collisions occur at the collision point after one orbit. The dip in planetesimal-planetesimal collisions occurs at the expected escape velocity of the remnant. The link between the escape velocity and the bimodal distribution can be down to the velocity kicks given to the planetesimals not being sufficient to clear the area around the remnant before reaching 0.25 orbits when collisions start to be resolved in the simulations.

b) Collisions and Mass

The number of collisions in a simulation will indicate how active each disk is. In Fig. 4.6 we show the cumulative number of destructive collisions over time in orbits for disks 13 to 52 in Table B.2 in grey and the median cumulative count in black. We see an initial flurry of destructive collisions early on before moving into a steadier increase in destructive collisions over time. We find that there are two different causes of collisions between planetesimals: the early time collisions, which mostly take place soon after collisions are switched on in the simulations (0.25 orbits), and collisions that take place around the collision point. The collision point is defined as the location where the initial giant impact occurred. For collisions taking place at the collision point, we find the total number of collisions varies over time as

$$N_{\rm tot}(t) = a + b\log_{10}\left(c + \frac{t}{t_p}\right), \tag{4.1}$$

where t_p is the turning point, with a, b, and c being constants. Fig. 4.7 like Fig. 4.6 shows the destructive collision count but only for an azimuthal slice of $|\phi| < \pi/10$ around the collision point. The increase in destructive collision count at the collision point over time is more uniform than when accounting for all the impacts. The less uniform distribution in Fig 4.6 suggests that the randomness of the planetesimal setup can cause large differences in collision outcomes within the first few orbits away from the collision point.

The collision count as a function of time relation in equation 4.1 means we should expect the collision rate to vary over time as

$$R_{\rm col}(t) = \frac{1}{\ln 10}\frac{b}{ct_p + t}. \tag{4.2}$$

The mean collision rate is shown in Fig. 4.8. The grey bins are the destructive collision counts around the collision point and the grey line is the collision rate calculated through dividing the collision count in each bin by the bin width. The blue bins and line represent the collision count and collision rate for collisions away from the collision point. The black dashed line

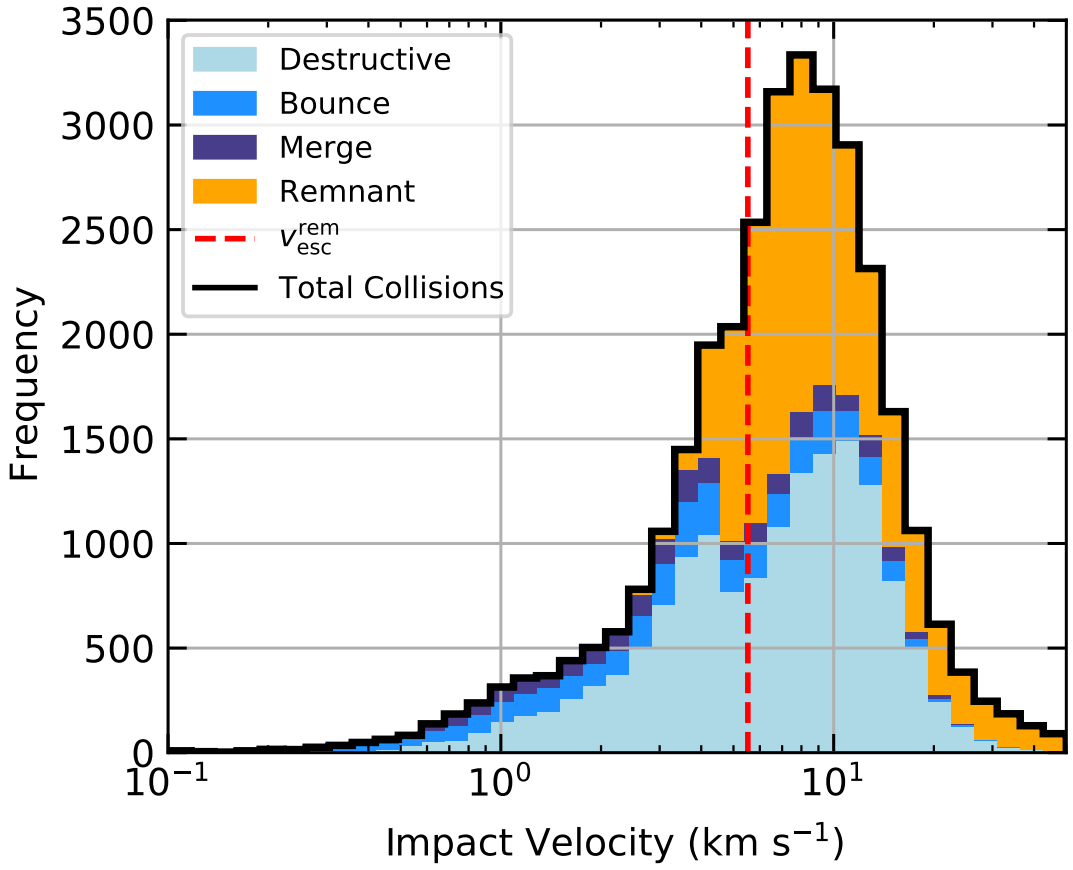

Figure 4.5: The distribution of impact velocities of planetesimal-planetesimal collisions and remnant-planetesimal collisions. The histogram counts all collisions for disks 13 to 52 in Table B.2. The colour denotes the frequency of a type of collision, blues are for planetesimal-planetesimal collisions and orange for remnant-planetesimal collisions. The blues split into: light blue for destructive outcome, blue for bounce outcome, and purple for merge collisions. All remnant-planetesimal collisions are merging. The red dashed line represents the escape velocity of the remnant, $v_{\rm esc}^{\rm rem}$.The black line represents the total number of collisions.

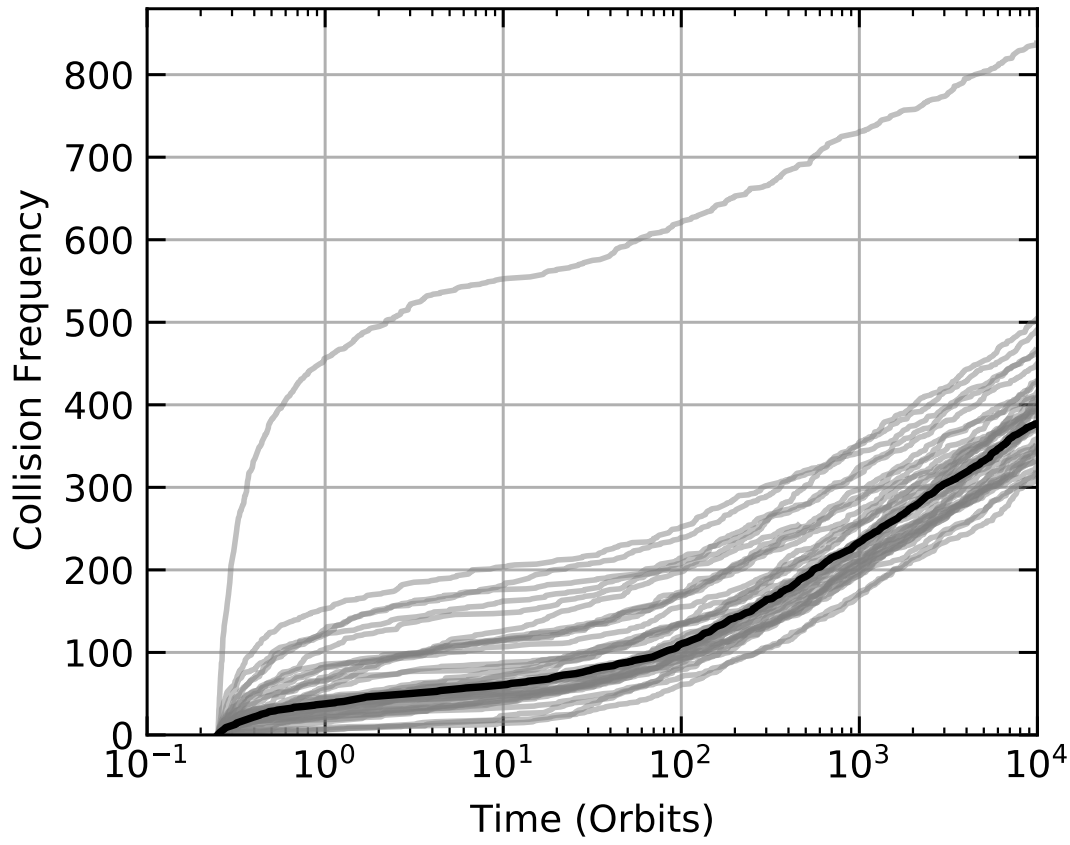

Figure 4.6: The destructive collision count over 10^4 orbits for disks 13 to 52 in table B.2. The grey lines represent individual simulations and the black line represents the median interpolated collision count.

shows the expected collision rate from equation 4.2 with parameters fit from the median collision frequency shown in Fig.4.7. We show that the expected collision rate is a good fit for collisions occurring at the collision point from five orbits onwards. The deviations away from the fit before five orbits could be caused by the remnant disturbing a large selection of planetesimals. As the planetesimals are escaping from the remnant at the start of the simulations, the remnant will have a large influence over the dynamics of the planetesimals in the first few orbits while the disk is starting to form. We see in Fig. 4.9 that the density inside 10 Hill radii of the remnant decreases sharply over the first five orbits of the simulations for disk 13 (teal) before remaining relatively constant throughout the rest of the simulation. The planetesimal number density decreasing rapidly around the remnant could be related to the collision rate dropping rapidly below the collision rate around the collision point. However, the collision rate outside the collision point keeps decreasing until around 100 orbits after the giant impact, much later than the density around the remnant levels off.

For collisions that occur around the collision point, we find correlation between the decrease in the number density of planetesimals at the collision point and the number of collisions recorded overall. In Fig. 4.10 we show the number density around the collision point for simulated disks at varying semi-major axes and two different giant impact orientations. We discuss how the position of the disk and orientation affects disk evolution in sections c) and d). For now we focus on disk 13 (teal, left panel) which has an semi-major axis (sma) of 0.5 au and is formed from a giant impact with an orientation of 0.5π. The number density is found to vary over time as,

$$n_{\mathrm{colp}}(t) = \frac{a}{\left(b + \frac{t}{t_c}\right)^p}, \tag{4.3}$$

where t_c is the turning point, and a, b, and p are constants. We find that disk 13 can be fitted approximately with the same t_c value for both equations 4.1 and 4.3. For the density fit, we used a value of $t_c = 160$ orbits. The decrease in number density of planetesimals at the collision point decreases the collision rate over time after an initial steady period. The collision point starts to smooth out over a timescale of over 100 orbits for a planetesimal disk formed from giant impact 1 with an orientation of 0.5π at 0.5 au.

We track the collisions to get an estimate for the mass that will be passed down the size distribution to grains which will impact the observability of the extreme debris disk in near to mid infrared wavelengths. Fig. 4.11 shows the median mass of disk masses from disks 13 to

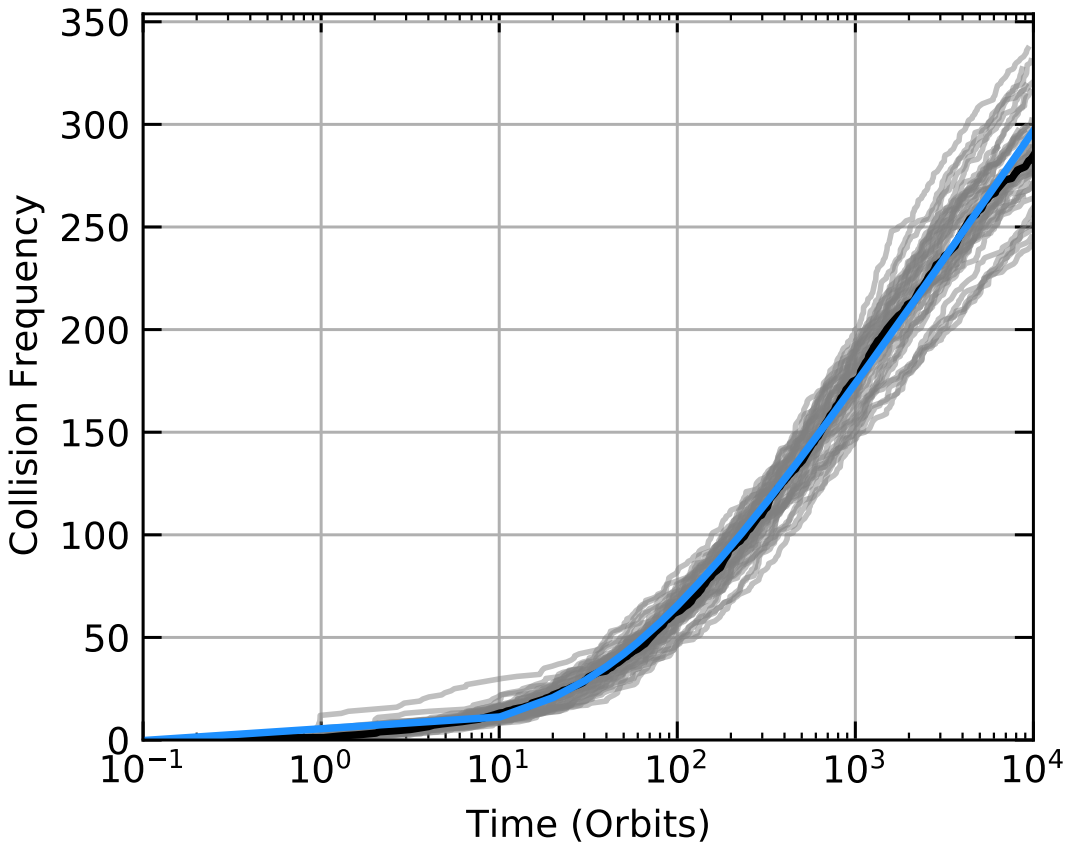

Figure 4.7: Same as Fig. 4.6 but only counts destructive collisions within $|\phi| < \pi/10$ slice of the collision point. The blue line is the fit to the data using equation 4.1 with $a = 0.16$, $b = 0.44$, $c = 0.43$, and $t_p = 98.66$.

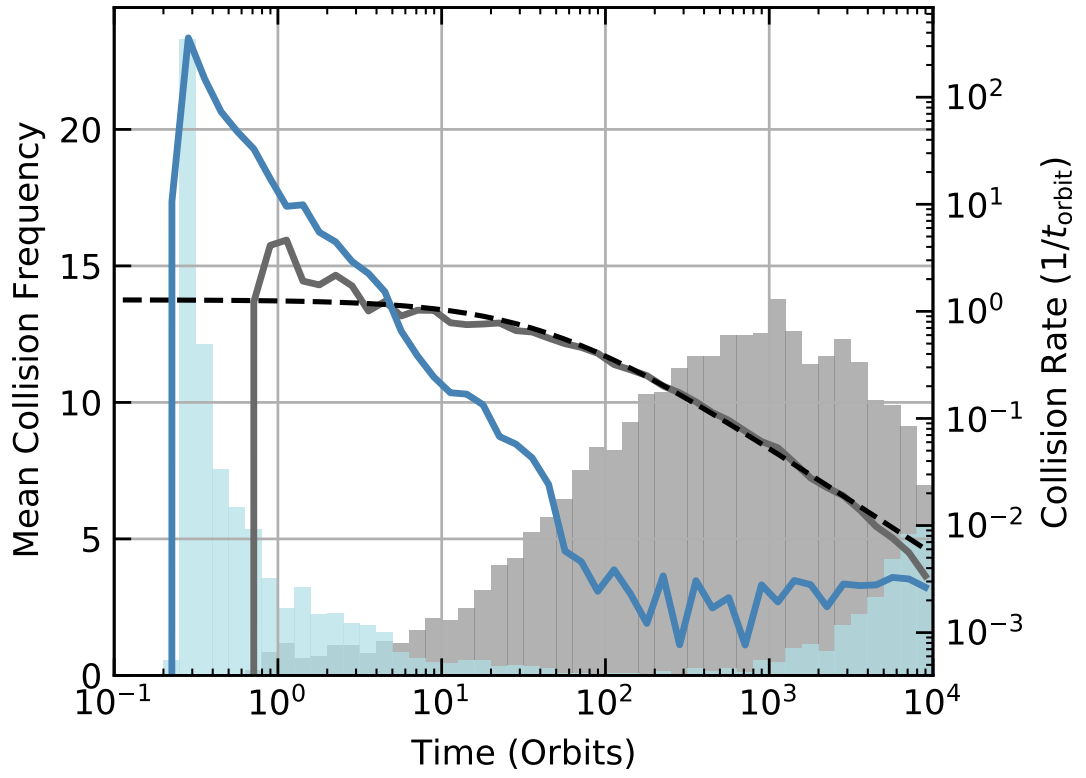

Figure 4.8: Left y-axis: histogram of the mean count of collisions in disks from 13 to 52 in Table B.2. Right y-axis: the mean collision rate with the solid lines determined from the mean count in each histogram bin divided by the bin width. The data is split between collisions occurring in an azimuthal slice of $|\phi| < \pi/10$ around the collision point (grey) and collisions occurring elsewhere (blue) with $|\phi| \geq \pi/10$. The black dashed line represents the expected collision rate for collisions around the collision point from equation 4.2 with parameters fit from the median collision frequency in Fig.4.7.

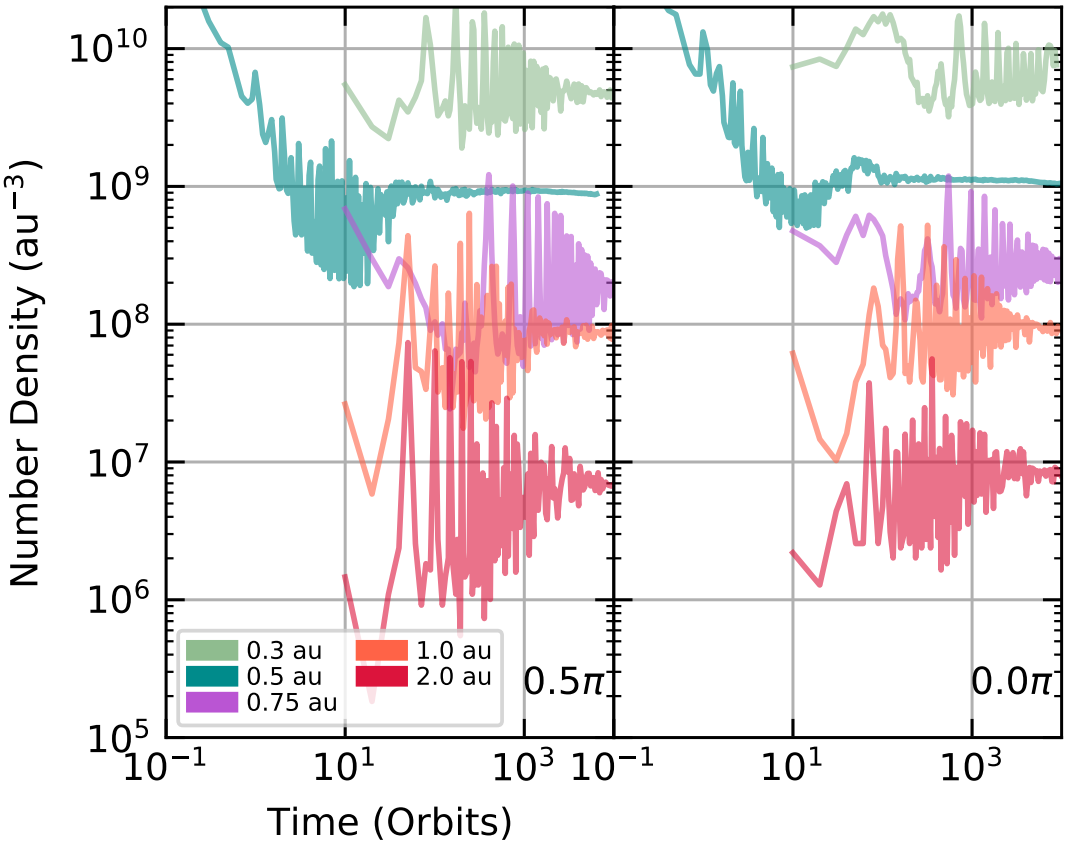

Figure 4.9: The number density of particles within 10 Hill radii of the remnant over time. Disks 1, 2, 3, 13, 53, 54, 55, 56, 57, and 58 were chosen to represent the change in density around the remnant as a function of semi-major axis. Disk 13 placed at 0.5 au is the only disk to be shown to extend below 10 orbits as it is the only disk for which output steps were saved every 0.1 orbits, the rest had steps saved every 10 orbits. The disks were formed from giant impact 1 with an orientation of 0.5π (left) and 0.0π (right).

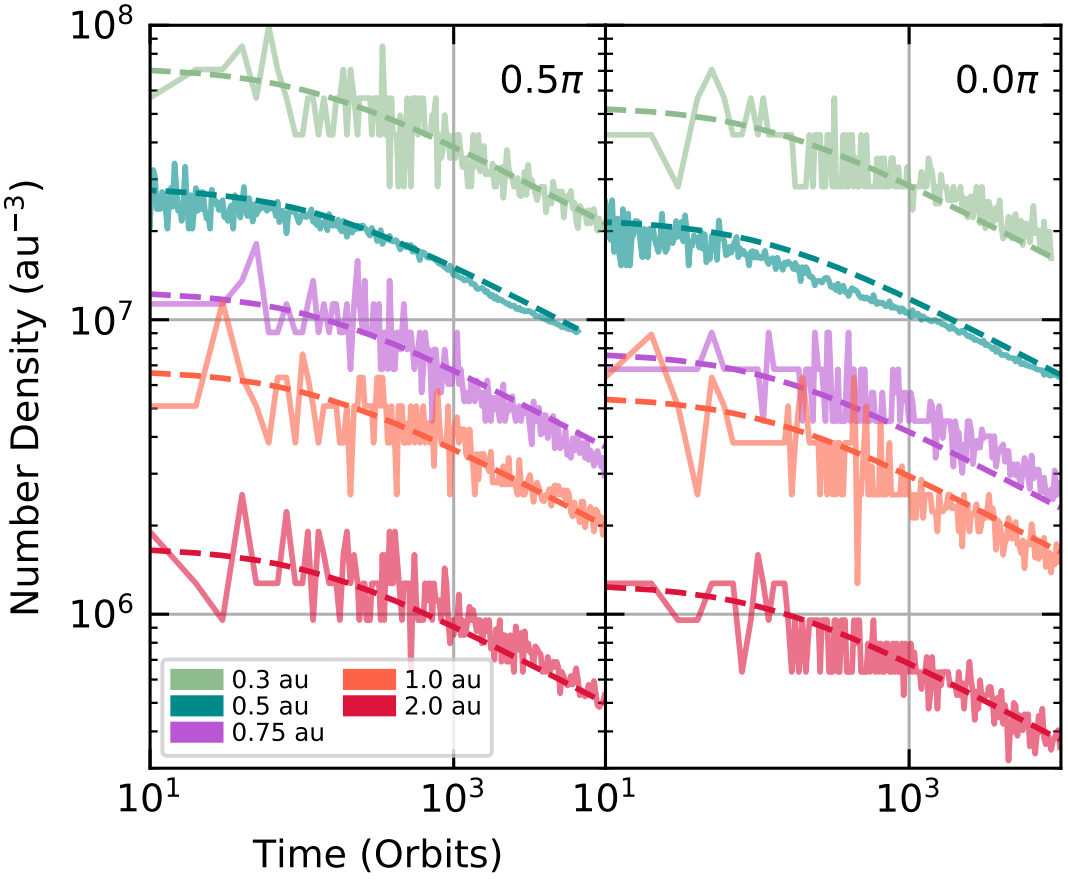

Figure 4.10: The number density at the collision point over time for disks 1, 2, 3, 13, 53, 54, 55, 56, 57, and 58. The solid lines are binned mean number density at the collision point. The dashed lines are the expected number density evolution fitted using equation 4.3. The disks were formed from giant impact 1 with an orientation of 0.5π (left) and 0.0π (right).

52 in Table B.2 over 10^4 orbits in black, and also shows the median mass produced within the azimuthal cut of $|\phi| < \pi/10$ and the mass produced outside the azimuthal cut in green and blue respectively. The coloured area around each line shows the 16th and 84th percentiles of mass produced. We see that the collisions between planetesimals outside the collision point give a sharp increase in mass in the initial few orbits. The mass produced at the collision point does come to dominate after $\sim$100 orbits and by 10^4 orbits the mass produced is an order of magnitude more than that produced outside the collision point, though we see in Fig. 4.2 that the collision rate around the collision point decreases over time. As we expect the disk to become more symmetric over time, the collision rate around the collision point will match the collision rate around the rest of the disk. Hence, at late times past the 10^4 orbits we simulate we would expect the contribution from the collision point to the mass produced to be less than that from the rest of the disk. The collision point enhances the number of collisions that we would expect from a symmetric disk in the disk's early formation and evolution.

c) Semi-major axis variation

Giant impacts do not only occur at 0.5 au, but can occur at any distance from their host star. For giant impact 1 with orientation of 0.5π, we vary the semi-major axis at which the impact occurred. We choose sma values of 0.3, 0.5, 0.75, 1 and 2 au with the disks being listed in Table B.2 as disks 2, 13, 54, 56, and 58. We limit the choice of sma values to 2 au as while giant impacts can occur further out, extreme debris disks are observed within the terrestrial planet formation zone. The disks use the same random seed for obtaining the properties of the planetesimals. The v_i/V^* distribution is shown in Fig. 4.12 for the giant impact induced disks at different sma. The coloured lines represent the different sma, and the grey shows the spread between the 2.5th and 97.5th percentile of the velocity distribution shown in Fig. 4.4. We find that while there appears to be some difference in the distribution going towards more destructive collisions at larger sma, all lines fall within the random sampling of a disk placed at 0.5 au. There is no major difference found between these single runs in terms of collisional outcomes. The collisional outcomes are expected to be similar as the disks are formed from the same giant impact. While we vary the bulk Keplerian motion given to the planetesimals, the velocity dispersion of the planetesimal population will remain the same. If the velocity dispersion remains the same then there should be no significant difference in relative speeds of the planetesimals. It is possible that there could be a difference when more runs are conducted

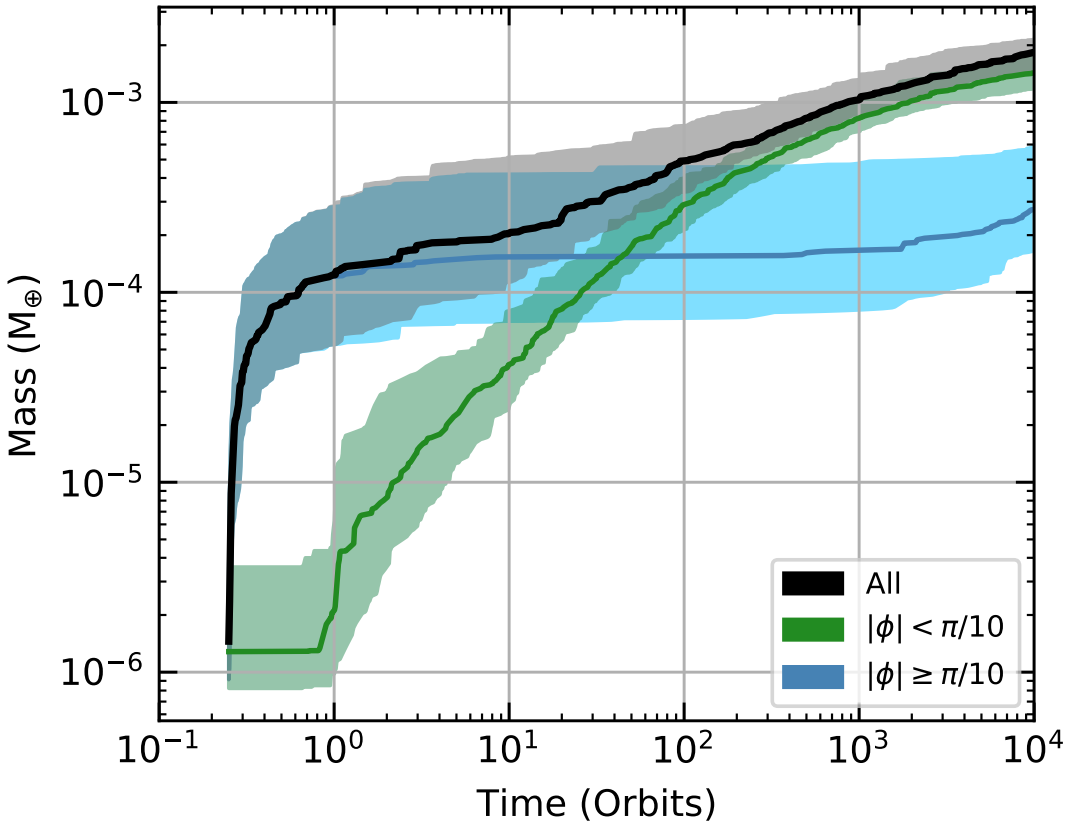

Figure 4.11: The median cumulative mass produced in destructive collisions in disks 13 to 52 in Table B.2. All collisions are shown in black, while collisions that occur within an azimuthal cut of $|\phi| < \pi/10$ around the collision point and collisions outside the collision point are shown in green and blue respectively. The coloured regions represent the 16th and 84th percentiles of the mass.

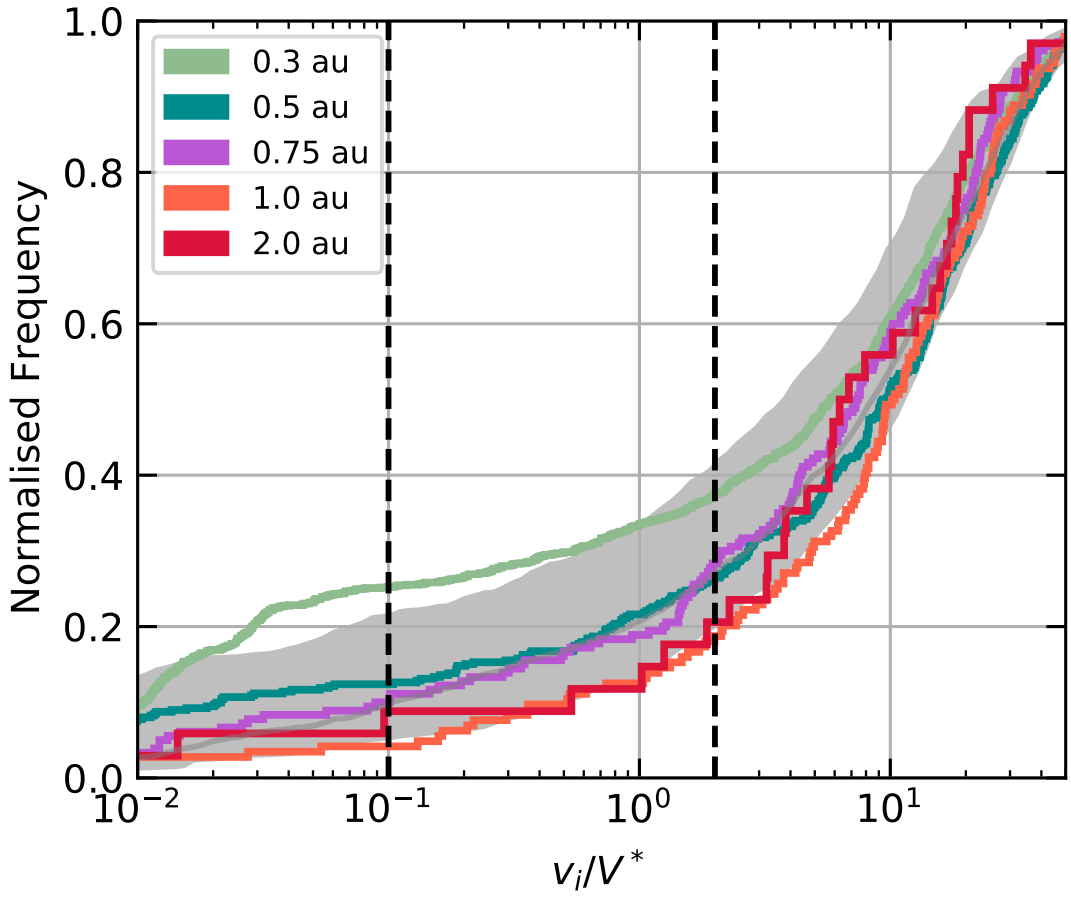

Figure 4.12: The cumulative velocity distribution for disks formed from giant impact 1 at different semi-major axes. The disks are disks 2, 13, 54, 56, and 58 in Table B.2. The grey denotes the 2.5th and 97.5th percentile of the median velocity distribution shown in Fig. 4.4.

but there would still have to be some overlap. The small difference seen between the distributions could be down to the number of collisions occurring in each disk.

The number of collisions for the disks at different sma are shown in Fig. 4.13. The number of collisions decreases as we move away from the star. We also see the initial collisional activity disappear beyond 0.5 au. The initial collisional activity dropping off can be explained by the change in the bulk Keplerian velocity given to the planetesimals. The Keplerian velocity varies as $v_k \propto r^{-\frac{1}{2}}$ for a circular orbit, where r is the distance. The ratio of velocity dispersion to Keplerian velocity then varies as $\sigma_v/v_k \propto r^{\frac{1}{2}}$, if σ_v is kept constant. For the same giant impact we would expect the disk to shear out on a faster orbital timescale further away from the star. Hence when collisions are turned on at 0.25 orbits, the planetesimals around the remnant have sheared out quicker in disks placed at greater sma. We see in Fig. 4.9 how the number density close to the remnant decreases as you move further away from the star, hence the remnant dynamically influences fewer planetesimals.

When the collision count is normalised, equation 4.1 still holds for collisions occurring at the collision point. This suggests that the orbital timescale for the collision point to smooth out is the same regardless of where the giant impact occurred. Though we do see a difference in the number of collisions that happen outside the collision point due to σ_v/v_k scaling with distance from the star. The close in disks have a planetesimal population that is more densely packed around the remnant in the initial few orbits.

The difference in the number of collisions between planetesimals can be explained by the difference in density at the collision point. The collision point does evolve the same for all disks but the initial density differs. We see in Fig. 4.10 how the density at the collision point changes over time for disks from 0.3 to 2 au. The density of particles at the collision point directly relates to the number of collisions expected. Since all disks share the same number of particles, it is likely that the initial volume of the collision point is larger for disks further out reducing the density. Again, the change in σ_v/v_k is the likely cause.

The mass of debris produced through planetesimal collisions for each disk is shown in Fig. 4.14. The sma are varied by colour, the dashed lines show the mass for disks formed from giant impact 1 with orientation 0.5π, and the dotted lines show the mass for the same impact with an orientation of 0π. We find between the 0.3 au and 2 au case over an order of magnitude difference in the mass of the disk. The other disks fall within this range. We see in Fig. 4.15 the mass over time of each disk split into mass produced around the collision point (top) and

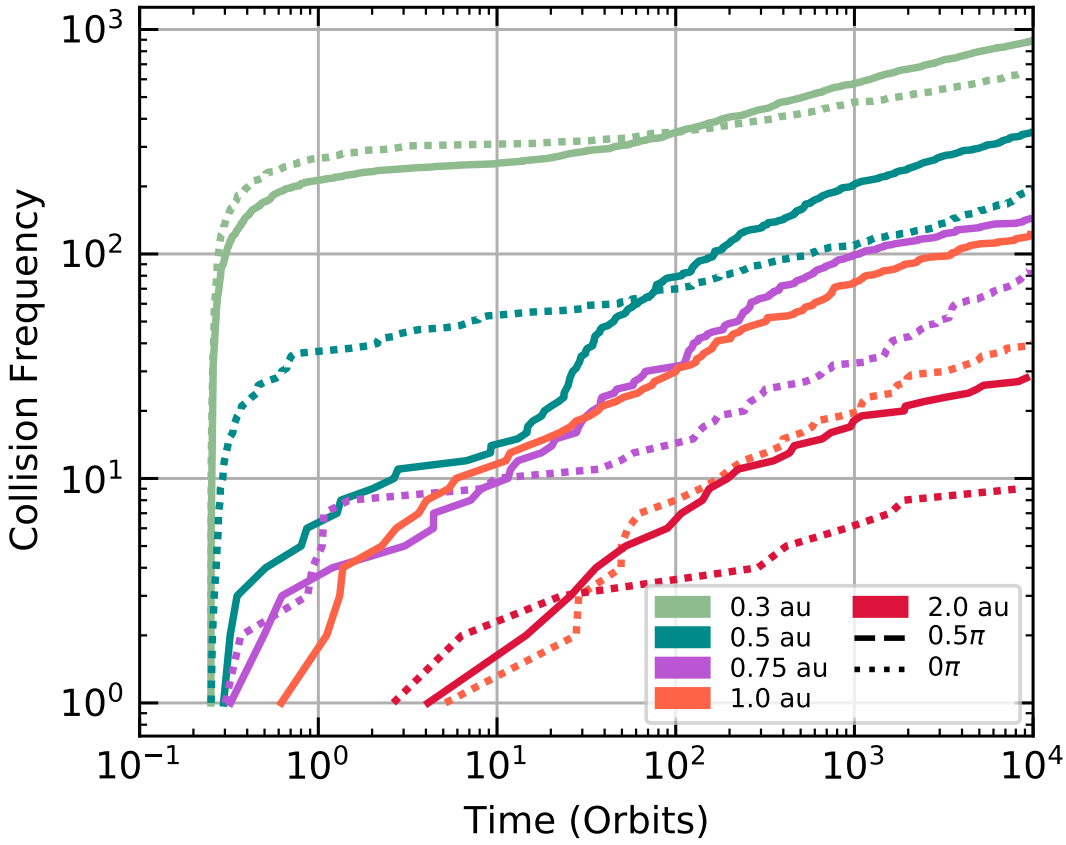

Figure 4.13: The cumulative collision count for disks 2, 13, 54, 56, and 58 in table B.2 over 10^4 orbits. The number of destructive collisions over time for disks formed fro giant impact 1 placed at different au. The dashed and dotted lines represent the $0.5\ \pi$ and $0\ \pi$ orientations respectively.

mass produced from collisions elsewhere (bottom). The disks close into the star experience a large contribution to the debris mass from collisions outside the collision point within the first few orbits. Beyond the 0.5 au disk we do not see a significant contribution to mass. Of course these are only one potential snapshot of the random distributions the planetesimals can take on. We might see a significant contribution from disks outside 0.5 au in some snapshots though this seems unlikely when comparing the densities around the remnant between the disks.

The effect of the lower density is seen in Fig. 4.16. The behaviour of each disk is the same over time, the collision rate decreases following equation 4.2. It is the initial collision rate that varies with distance from the star. The further away the giant impact occurs, the smaller the initial collision rate.

d) Orientation

All giant impacts distribute ejecta anisotropically. The orientation which the giant impact occurs at with respect to the stellar system reference frame can have a huge impact on the disk structure. We showed in Watt et al. (2021) (chapter 3) how the orientation affects the light curve seen from a vapour condensate disk, specifically the dips in the light curve at the collision point and anti-collision line not always appearing. For giant impact 1 we ran 40 simulations for disks forming at 0.5 au formed with an impact orientation of 0.5π, we have also run 10 simulations for an orientation of 0π to understand if orientation plays a large role in planetesimal collisions as it does in the behaviour of the light curve in the vapour condensate disk.

Fig. 4.17 shows the v_i/V^* for disks 3 to 12 in Table B.2 in grey. The median distribution is shown in black, and the orchid area shows the 2.5th to 97.5th percentile range for the v_i/V^* in Fig. 4.4. Between the different orientations, we find no significant differences between the number of destructive collisions between planetesimals. Like in the different sma cases, the disks formed from giant impact 1 with different orientations have the same absolute velocity distribution. The relative velocity difference between the planetesimal groups will only be down to random sampling the parent population of ejecta from the SPH simulation. There is a difference in the distribution of the directions the velocity kicks are given due to differing orientations but this has no bearing on the absolute velocity values.

The orientation of the giant impact does change the number of collisions within the resulting disk. We show in Fig. 4.18 how the number of collisions in disks 3 to 12 varies over time compared to disks 13 to 52 which are shown in Fig. 4.6. Between the two sets of simulations, we

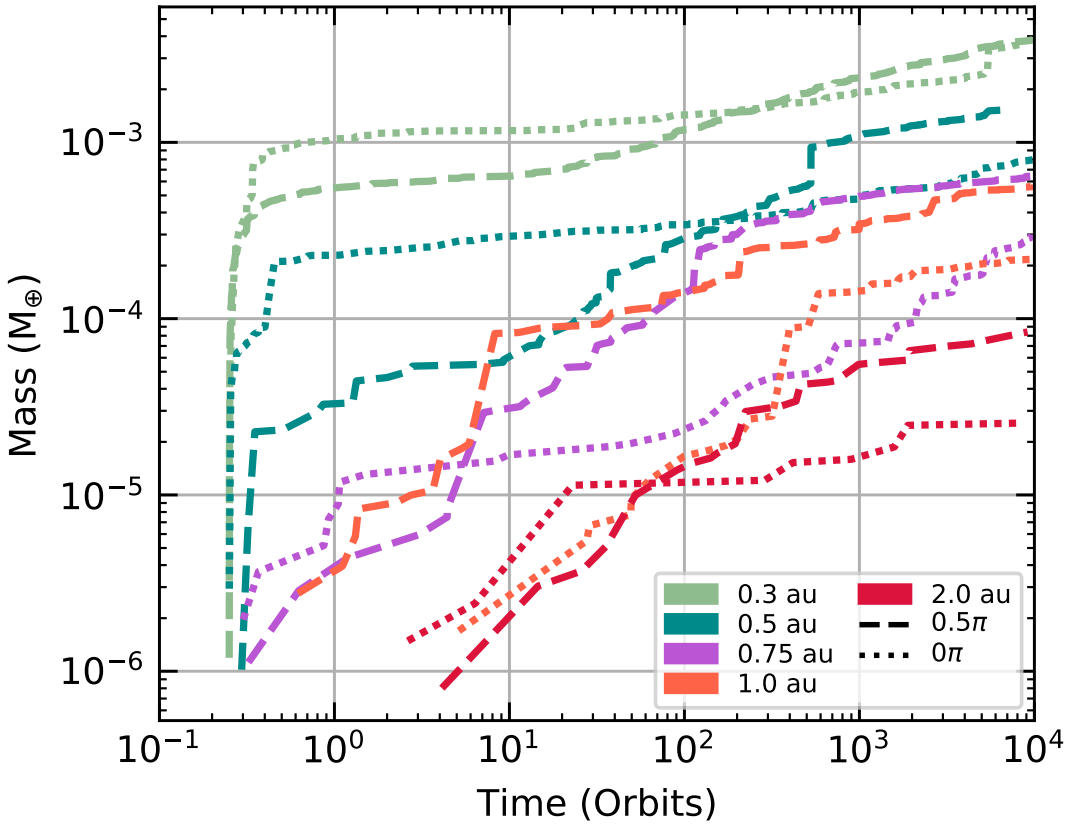

Figure 4.14: Mass produced through destructive planetesimal collisions over time for the disks formed from giant impact 1 with orientations 0π (dotted) and 0.5π (dashed) between 0.3 au and 2 au.

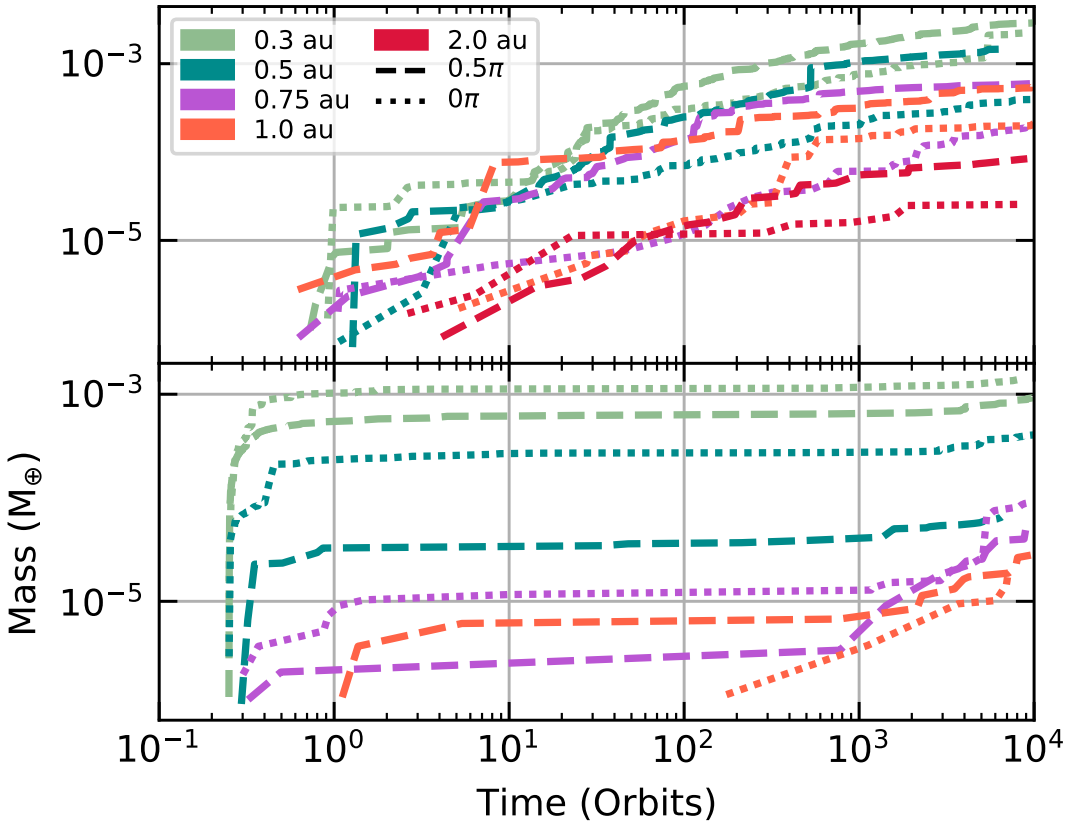

Figure 4.15: Disk mass split into mass produced within a azimuthal cut of $|\phi| < \pi/10$ around the collision point (top) and outside the collision point (bottom). Disks are formed from 0.3 au to 2 au. Dashed lines are for disks formed from giant impact 1 with an orientation of 0.5π and dotted lines are for an orientation of 0π.

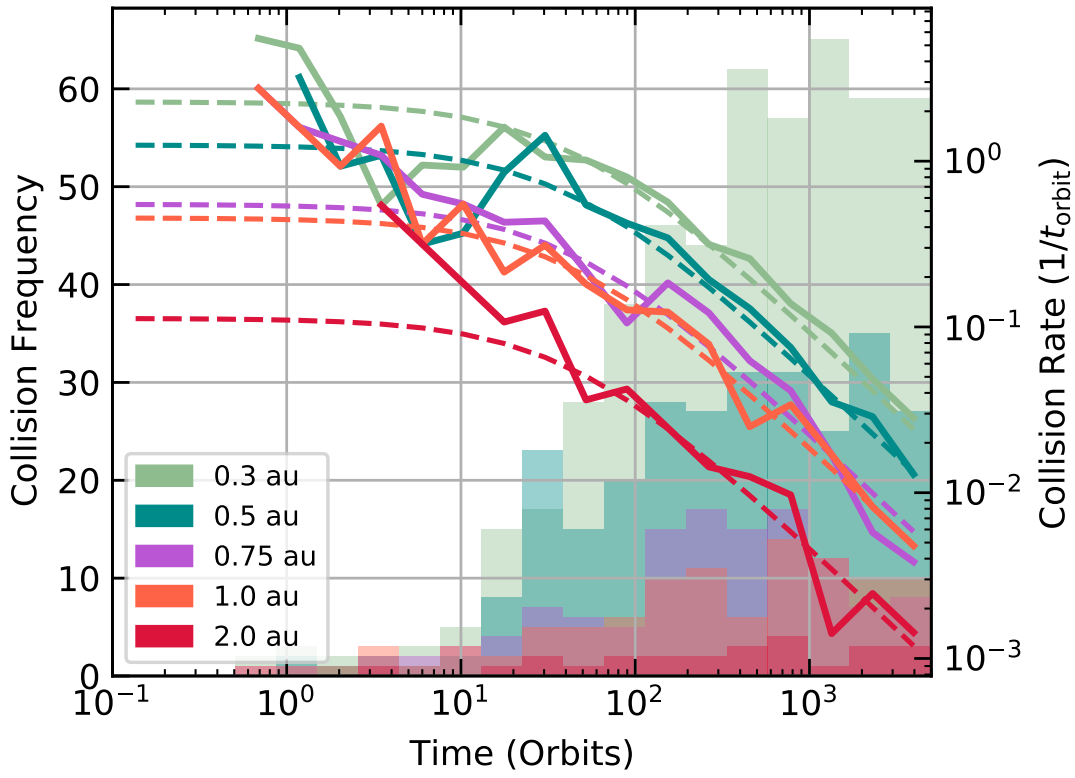

Figure 4.16: Left: An histogram of collisions in disks 2, 13, 54, 56, and 58 over time in orbits. Right: Collision rate for each disk calculated from the bin count divided by the bin width. Dashed lines show fits for the collision rate using equation 4.2.

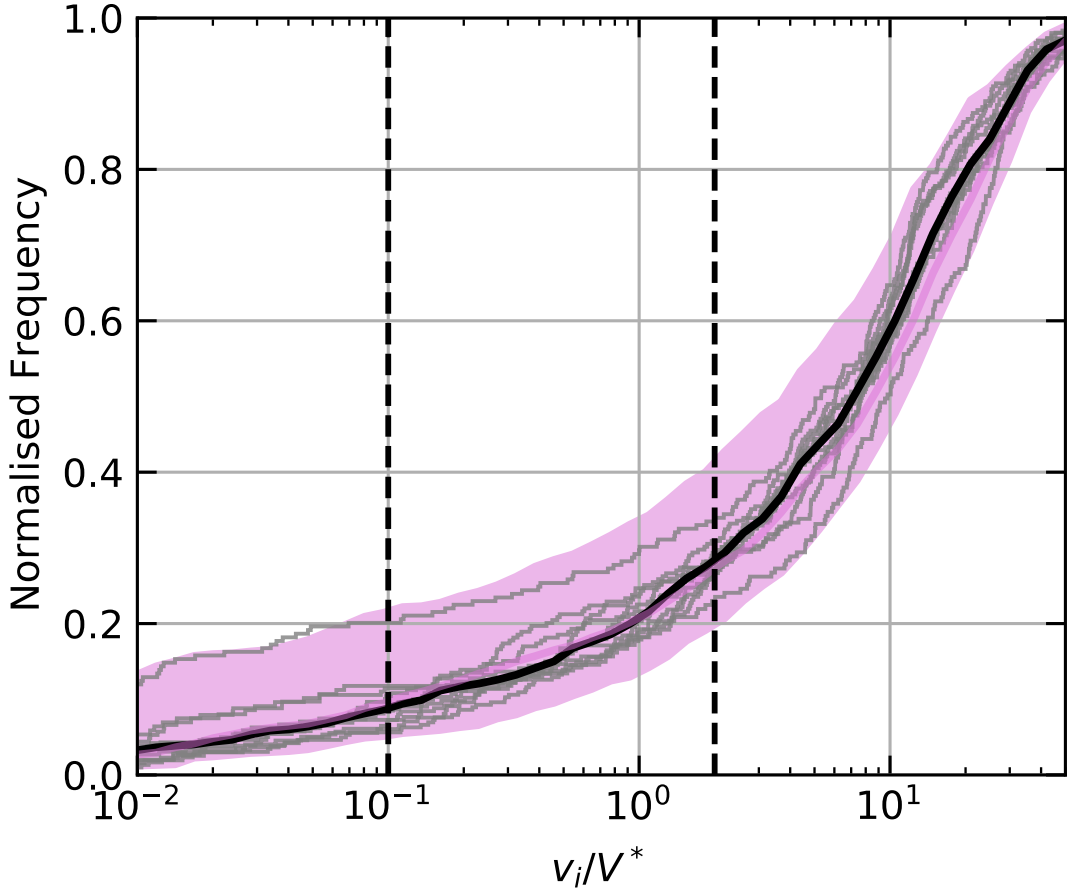

Figure 4.17: Same as Fig. 4.4 but now for disks 3 to 12 in Table B.2. The orchid area is the 2σ range of the median fit to disks 13 to 52. The figure compares collision outcomes between the 10 simulated disks for giant impact 1 with an orientation of 0π against an orientation of 0.5π.

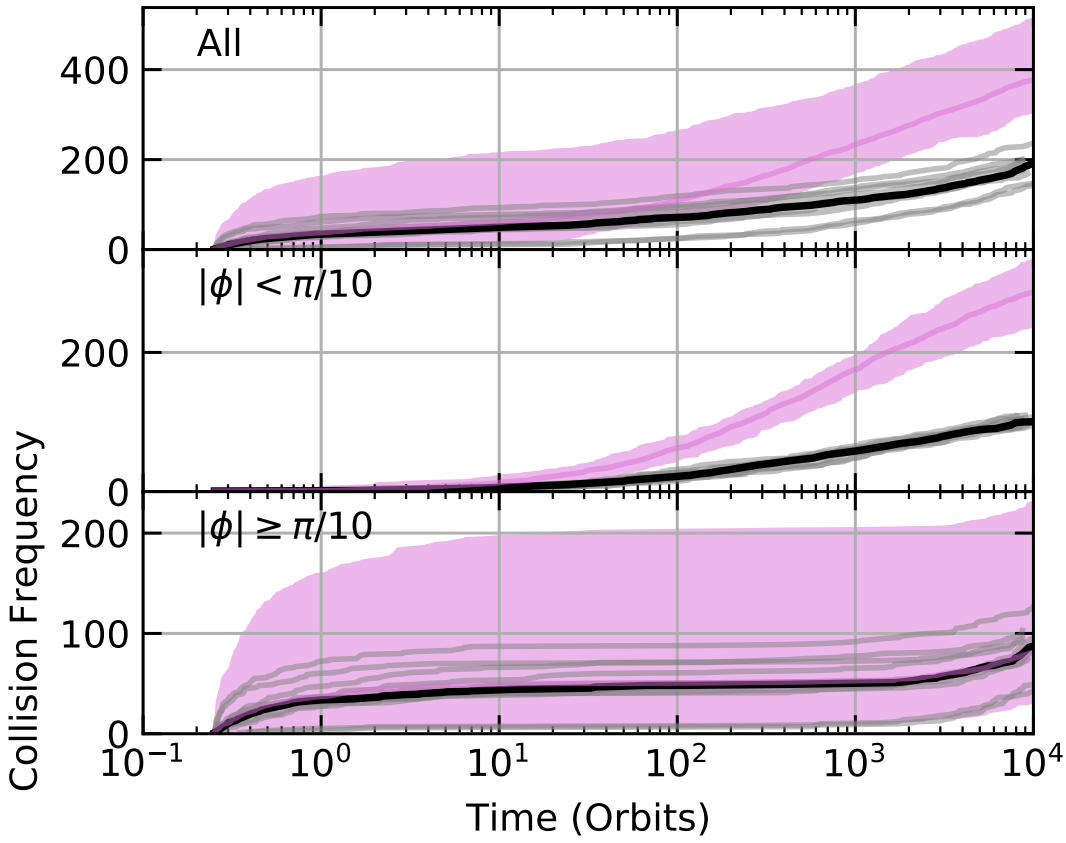

Figure 4.18: The cumulative collision count for disks 3 to 12 in table B.2 in grey. The median collision count is shown in black, and the orchid filled area represents the 2σ range about the median collision line for disks 13 to 52. The figure is split into three parts, the top shows all destructive collisions between planetesimals, the middle shows collisions that happened within an azimuthal cut of $|\phi| < \pi/10$, and the bottom shows collisions that happened outside the collision point.

find that the median number of collisions in disks formed from giant impact 1 with an orientation of 0π to be approximately half the number of collisions that occurred in disks that formed from an orientation of 0.5π. The difference is caused by the number of collisions at the collision point in the two sets of simulations. A decrease in the number of collisions at the collision point indicates that the number density in the 0π disk simulation set is reduced compared to the number density of the 0.5π simulation set. Fig 4.10 shows the median number density of disks formed from giant impact 1 with orientations of 0π and 0.5π, varying in impact sma from 0.3 to 2 au. The overall behaviour of how the density evolves is the same regardless of the initial orientation of the giant impact, with the density falling off as expected from equation 4.3. We find that there is no significant difference for the collisions that occur outside the collision point. We see this trend appear in Fig. 4.14 and Fig. 4.15 where the difference in the mass produced between the different orientations is caused solely by the mass produced at the collision point. The difference between the number of collisions at the collision point will be down to the difference in orbital parameters given to the planetesimals. The orbital parameter difference is caused by the difference in the direction of the orbital kicks given to the planetesimals. In the 0π orientation, the kicks given to the planetesimals are dominated by radial velocity kicks. Radial velocity kicks are less efficient at changing the orbit of a particle than tangential velocity kicks. The 0.5π orientation has the velocity kicks mostly in the tangential direction, hence the orbital parameter difference and therefore different disk structure. For the 0π orientation the planetesimals are on more similar orbits when compared to 0.5π orientation, reducing the number of potential orbital crossings between planetesimals.

Fig. 4.19 shows the mean collision rate around the collision point for the disks 3 to 12 (green) and disks 13 to 52 (orchid) as solid lines. The mean collision rate outside the collision point is shown with blue and orchid dotted lines for disks 3 to 12 and disks 13 to 52 respectively. The dashed lines show the expected collision rate using equation 4.2. There is no difference between the evolution of the collision rates between the different orientations of giant impact 1, we only find a difference in the initial collision rate with 0.5π orientation starting with a larger collision rate around the collision point. Even within the first few orbits the collision rate is the same, suggesting the remnant is a large influence early on. Once the collision rate outside the collision point stops being the dominant collision position, the collision rate around the collision point settles to the expected collision rate. We find there is no difference in how a disk formed from different orientations of a giant impact evolves over time. The only difference between

disks is the initial set up which sets the initial collision rate. This is seen in how the density at the collision point evolves over time in Fig. 4.10. The density at the collision point is typically lower for the 0.0π orientation over 10^4 orbits, though the density change is not as drastic as when the sma is varied.

e) Varying Impact

Giant impact 1 is not the only impact that can occur. We have conducted a preliminary test of the parameter space to look at two other impact scenarios. These impacts are listed in Table 4.1. In summary, impact 3 is the same as impact 1 with a higher impact velocity, while impact 2 is a more typical collision with a mass ratio of 0.4, and an impact parameter of $b = 0.4$.

In Fig. 4.20 we show histograms for the collision count and the collision rate for the three giant impacts with orientations of 0.5π and placed at 0.5 au. We find for giant impacts 1 and 3 that they have similar behaviour which is to be expected as the only varying parameter is the impact velocity between the two. We find giant impact 2 to be less collisionally active. At late times we see that all giant impacts follow the expected collision rate at the collision point. We see deviations early on due to small number statistics with giant impact 2 and the effect of the remnant in giant impacts 1 and 3. We note that in the giant impact 2 case, the second largest remnant had a large enough mass to be considered important to track gravitationally. The two large remnants in giant impact 2 might be the cause of the reduced collision rate. Another important difference with giant impact 2 is the change in distribution of the planetesimals initially. The difference in distributions is what is likely to cause the large difference in collision rates between the two disks. We need to explore more parameter space in order to definitively say how differing giant impact parameters would affect the collision rate in the disk. We have shown in these initial giant impacts that the collision rate in the disk can vary greatly even with planetesimal disks having similar masses (giant impact 2 produces a disk with 70% of the mass of giant impact 1 and 3). We also show that the evolution of the collision rate at the collision point is consistent across different giant impacts.

4.4 Discussion

We now discuss how our results affect the observability of an EDD. We also discuss what the limitations of the study are and potential improvements.

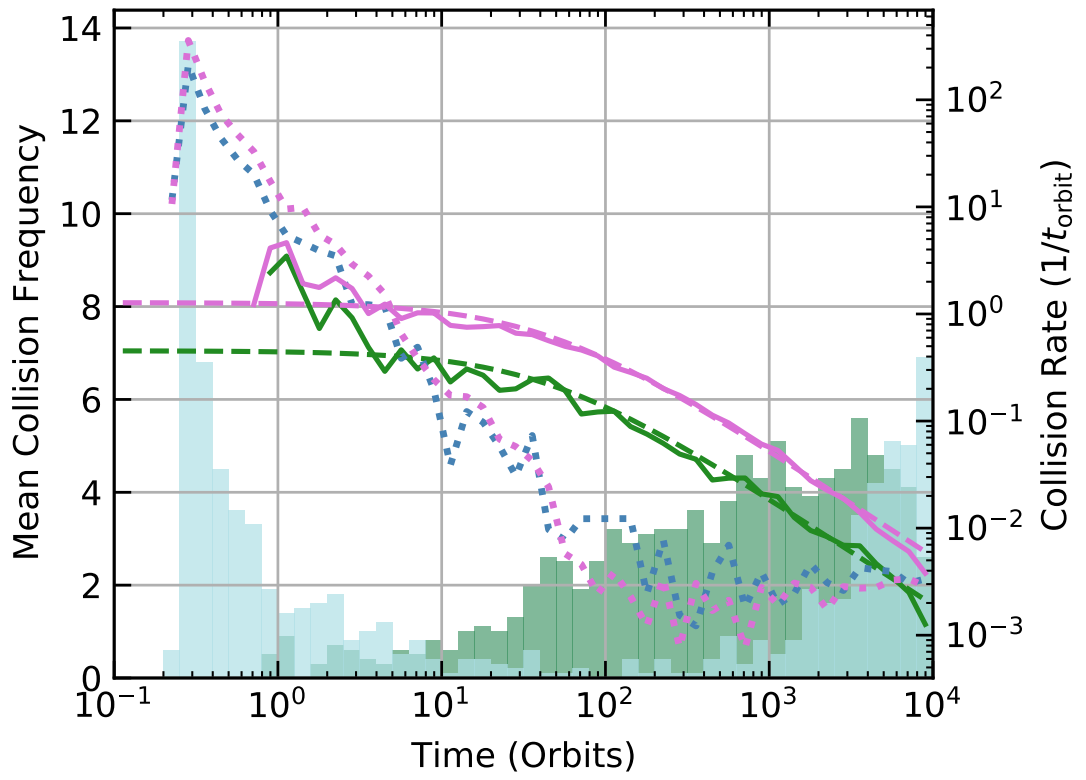

Figure 4.19: Left: The mean destructive collision count histograms for disks 3 to 12. Right: The mean destructive collision rate calculated from the bin count divided by the bin width, lines track collision rates. Green represents collisions occurring in an azimuthal cut of $|\phi| < \pi/10$ centred on the collision point, and blue represents collisions that occur outside the collision point. The orchid represents mean destructive collision rate around the collision point for disks 13 to 52. The solid lines follow the measured collision rate around the collision point, dotted lines track the collision rate outside the collision point, and the dashed lines represent the expected collision rate around the collision point from equation 4.2.

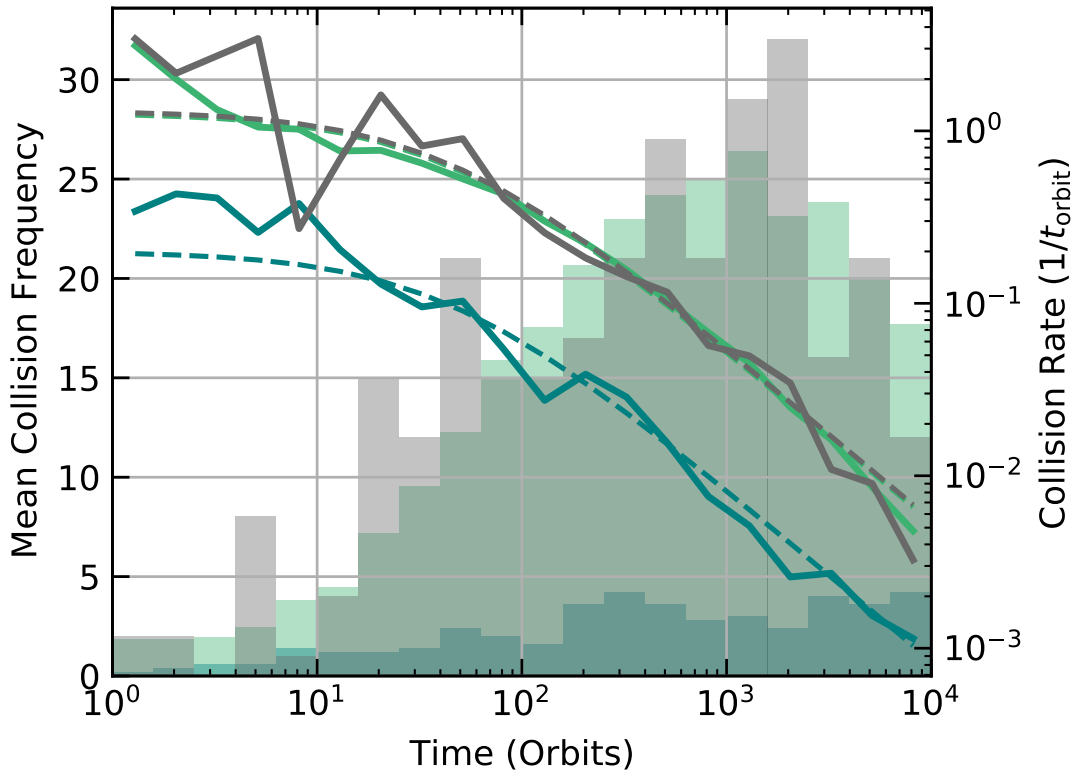

Figure 4.20: Same as Fig. 4.16 but now shows the mean collision frequency for the three giant impacts listed in Table 4.1. The disks used are listed as 13-52, 59-63, and 64 in Table B.2. Giant impacts 1, 2, and 3 are green, blue and grey respectively.

4.4.1 Flux

Now we know how a planetesimal disk formed after a giant impact might collisionally behave over time, we can look at the effect of the planetesimal disk on the observed extreme debris disk. It is complicated to model the effect of debris produced in planetesimal-planetesimal collisions on the observability and track how that debris evolves over time. There are many factors to consider such as how the planetesimals form solid objects post-giant impact. Are they a collection of small rocks forming rubble piles, or completely formed solid bodies? In the early disk lifetime, it could be possible that some of each planetesimal has not fully solidified or aggregated. Throughout we have assumed that the planetesimals are solid bodies which are the best producers of small grains as shocks are able to pass through them more easily. In the example of a rubble pile, the object is more likely to break up into smaller chunks but nothing that would be immediately visible. In any collision, we do not know what the size distribution of the ejecta will be.

To simplify we can estimate the fractional luminosity of debris produced by a planetesimal disk by using a traditional debris disk model. Fig 4.21 shows a fractional luminosity over time plot for disks between 0.3 and 2 au formed from giant impact 1 with orientations 0.5π and 0π which are the dashed and dotted lines respectively. The dashed and dotted lines are the smoothed expected fractional flux where the mass is added at the time each collision occurs. The fractional luminosity for each disk is calculated using the model from Wyatt (2008) that describes the evolution of a traditional debris disk,

$$f/M_{\rm tot} = 0.37 r^{-2} D_{bl}^{-0.5} D_c^{-0.5}, \tag{4.4}$$

where f is the fractional luminosity of the disk, $M_{\rm tot}$ is the total mass in the disk in Earth masses, r is the position of the disk in au, D_c is the diameter of the largest planetesimal in km and D_{bl} is the blowout size in . We assume that the largest object in the destroyed planetesimal material is 10 m and that the blowout size is that of a solar-like star: $0.8\ \mu$m. To evolve a debris disk, all values in equation (4.4) are fixed besides $M_{\rm tot}$ which varies with time as:

$$M_{\rm tot}(t) = M_{\rm tot}(0)/[1 + (t - t_{\rm stir})/t_c], \tag{4.5}$$

where,

$$t_c = 1.4 \times 10^{-9} r^{13/3} (dr/r) D_c Q_D^{*5/6} e^{-5/3} M_*^{-4/3} M_{\rm tot}^{-1}, \tag{4.6}$$

dr/r is the width of the disk which is set to 0.5, Q_D^* is the planetesimal strength assumed to be 150 J kg^{-1}, e is the mean planetesimal eccentricity of the planetesimal disk, and M_*, the central star mass, is one solar mass. The timescale of mass loss (t_c) starts when the destructive collisions occur which is determined by t_{stir}.

The above describes a fully formed traditional debris disk and how it evolves over time. To know how the fractional luminosity behaves after adding mass from planetesimal-planetesimal collisions, we need to estimate how the mass from each collision evolves. To do so we make equation (4.5) a summation of each planetesimal collision:

$$M_{\mathrm{tot}}(t) = \sum_{i}^{N_{\mathrm{tot}}} m_i(0)/[1 + (t - t_{\mathrm{stir}})/t_{c,i}], \tag{4.7}$$

where,

$$t_{c,i} = 1.4 \times 10^{-9} r^{13/3} (dr/r) D_c Q_D^{*5/6} e^{-5/3} M_*^{-4/3} m_i^{-1}, \tag{4.8}$$

here m_i is the mass liberated from each destructive planetesimal-planetesimal collision , i, N_{tot} is the total number of destructive planetesimal-planetesimal collisions, and all other variables keep the same values as above. With equation (4.7) and (4.8) we can add mass at any arbitrary time. The issue that arises with our method here is we are evolving the mass from different planetesimal-planetesimal collisions separately. This is not realistic as the mass liberated from one collision will affect the evolution of the mass liberated from a different collision. We could not have added mass at any arbitrary time using equation (4.5) and (4.6) as the total mass is determined by the initial total mass and t_c which is inversely proportional to M_{tot}. The disk would evolve too quickly in this scenario. In our scenario, the mass in the disk will evolve slower than expected though it does allow for complex fractional luminosity behaviour. The complex luminosity behaviour is realistic compared to an ever steeper curve as mass is added and near instantly will be observable. The changes in the fractional luminosity will be near instantaneous after every planetesimal-planetesimal collision. In both cases, we do not take into account how the mass added to the observable disk from planetesimal collisions interacts with the vapour condensate disk or the mass that falls between our definition of melt material that forms planetesimals and vapour material that forms small grains.

We can also estimate how the total mass within the disk varies over time with a t_c that varies with time. We define a $t_c(t)$ as

$$t_c(t) = 1.4 \times 10^{-9} r^{13/3} (dr/r) D_c Q_D^{*5/6} e^{-5/3} M_*^{-4/3} M_{\mathrm{des}}(t)^{-1}, \tag{4.9}$$

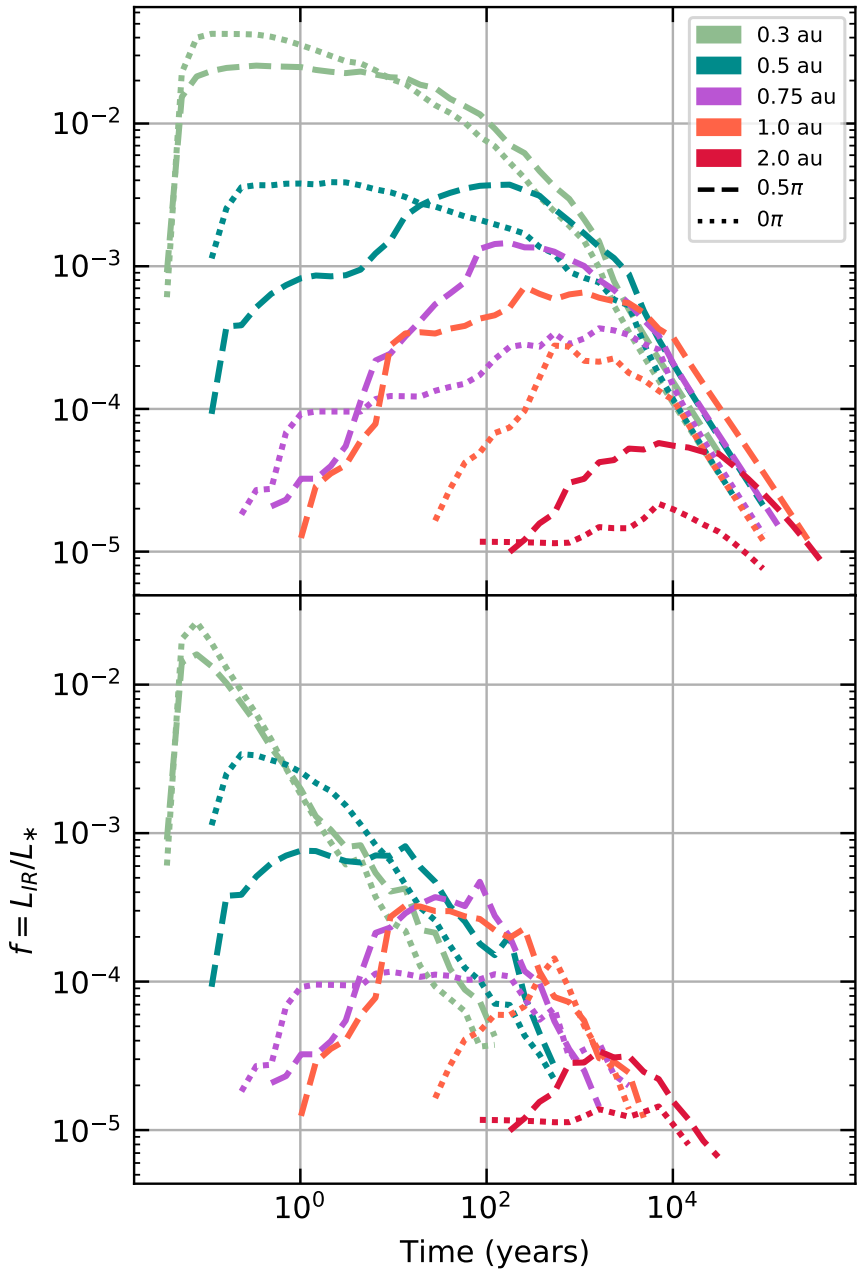

Figure 4.21: The estimated flux (Wyatt, 2008) of the planetesimal disk of giant impact 1 with a orientation of 0.5π (dashed) and 0.0π (dotted). The planetesimal disks are placed between 0.3 and 2 au. The disks used are 1, 2, 3, 13, 53, 54, 55, 56, 57, and 58. Top: timescale is set by equation (4.8). Bottom: timescale is set by equation (4.9).

where $M_{\rm des}(t)$ is the total mass added to the observable disk up to time t. Now if we use equation (4.9) in equation (4.7) the change in mass would be more drastic than if we use equation (4.8). We note though that $t_c(t)$ is dependent on the mass added from each destructive planetesimal collision hence $t_c(t)$ will only decrease with time. Using equation 4.9 will cause depletion of mass from the disk on timescales shorter than what would be expected.

In Fig. 4.21 we show how the observed planetesimal disks varies with time for both methods we have outlined. We find that the giant impact location has a massive affect on the flux of the extreme debris disk. The closer in the giant impact, the greater the effect of the planetesimal disk on the fractional luminosity of the extreme debris disk. We expected a brighter disk closer in as the disk overall will be hotter, but this is not the only reason. The planetesimal disk that will feed the extreme debris disk material is more collisionally active closer to the central star. Planetesimal disks closer to the star are likely to have a larger number of collisions happen earlier in the lifetime of the disk, leading to an initial large increase in dust added to the observable extreme debris disk. The vapour condensate disk should be observable near instantaneously after the giant impact (Watt et al., 2021), and planetesimal disks close to the star will provide more material for the extreme debris disk. Hence, extreme debris disks formed from a giant impact close to their host star will have a larger fractional luminosity not just because the disk will be hotter but there will be more mass in small grains provided by the planetesimal population being collisionally active early in the lifetime of the disk.

The difference we would expect to see from orientation of the giant impact does not make a real difference in terms of fractional luminosity for disks close to the star but has a larger affect the further the giant impact occurs from the star. We see in section d) that there is no difference between the early collision rate of the disk when orientated differently. The difference only arises in the collision rate at the collision point. For giant impact 1, as it is placed closer to the star the collisional activity in the initial few orbits increases and produces a substantial amount of mass. The mass produced from collisions in the early disk allow the 0π orientations to have similar fractional luminosities to the 0.5π cases in disks placed at 0.3 and 0.5 au. Once the giant impact is placed at a distance which reduces the initial collision rate then the difference between 0π and 0.5π cases is established. We see there is a significant difference between the different orientations from the 0.75 au case outwards in Fig. 4.21.

We find there to be a stark difference between the fractional luminosity evolution depending

on whether we use equation (4.8) with each destructive planetesimal collision being set a collisional timescale or (4.9) with which all planetesimal mass follows a single collisional timescale that varies with time. With equation (4.8) we find that the fractional luminosity tends to be brighter and remains in a brightened state for longer than compared to equation (4.9) which we expected. Interesting to note that for equation (4.8) we find that all disks regards of distance from the star will be observable up to $\sim 10^5$ years after the giant impact if we assume an $R_\nu = 0.03$ where $R_\nu = F_{\nu\ \mathrm{disk}}/F_{\nu\ *}$. For equation (4.9) the time at which the disk becomes undetectable varies with distance from the star, with the 0.3 au disks having the shortest detectable lifetimes. Equation (4.9) gives us an estimate of the lower limit on the detectability lifetimes of the disks while equation (4.9) is likely the upper limit on the detectability lifetime.

4.4.2 Disk Mass

The observable mass produced by collisions between planetesimals in our simulated disks will not account for all the observable mass produced in a real planetesimal disk. First, we do not account for the mass between our planetesimal size distribution (>10 km) and the vapour condensate (<100 mm). While the mass between does not make up a large fraction of the total mass in the disk, it is a reservoir of material which could affect the flux of the disk. While initially it will not be observable, disks formed by giant impacts will have a greater collision rate enhanced by the collision point. These intermediate-sized bodies can be ground down on a quick timescale to be observable. From the SPH simulations, we define the mass between as the total mass of particles with a vapour fraction between 10% and 20%. Here we assume the vapour fraction is significant enough to hinder the growth of larger melt objects so this material will form smaller melt objects.

The mass between was not looked at as it will not provide a substantial amount of material to the visible disk over a large amount of time. Though this is dependent on the assumed vapour fraction cuts. The disks formed from giant impacts are asymmetric, it is difficult to exactly know when this mass will be added to the observable disk. Compared to a traditional debris disk, the collision point in a giant impact induced disk increases the collisional activity within the disk. Since we know the vapour condensate would be seen near instantaneously after the giant impact and planetesimals add to the disk flux after a few orbits we would expect the mass between to be processed relatively quickly, therefore adding to the flux of the disk on the order of a few orbits. Since the top grain/boulder size (biggest being metres in size) of this other mass will be

small, once it is collisionally active the lifetime will be short so we can assume all the mass will be added at once. If the fraction of other mass is comparable to the vapour mass then it will have a significant impact on the fractional luminosity seen from the extreme debris disk. More work needs to be done on the assumption that giant impacts will form different populations of dust/boulders and how these populations interact with each other.

4.4.3 Mass definition

We have defined three different populations formed after a giant impact: a vapour condensate disk seen near instantaneously after the impact, a planetesimal population which is formed by near purely melt material, and the mass between these populations which will be a mixture of melt and vaporised material. We made the assumption that for any object made up of more than 10% vapour material will not be able to clump into a planetesimal-like object as the expanding vapour bubble(s) will impede this behaviour. However, this is not a known value hence how does the behaviour of the planetesimal disk change with the vapour cutoff value? Changing the vapour cutoff value will change the mass used to draw planetesimals from in our simulations. A larger vapour cutoff will increase the planetesimal mass and vice versa. From the SPH simulations of the giant impacts we are able to define the largest planetesimals in our simulations and from these planetesimals we extend the size distribution downwards until we have distributed all melt mass into planetesimals. By changing the vapour cutoff value, we change the the smallest planetesimal size in our distribution as we fix the size distribution to be $dN \propto D^{-3}$. Changing the vapour cutoff value changes the number of planetesimals at the smaller end of the planetesimal distribution. The collisional activity in a simulated disk is related to the number of objects in that disk. Therefore, changing the vapour cutoff value will change the likelihood of collisions between planetesimals occurring, not just the mass in the disk overall. In our scenario with a fixed size distribution, a larger vapour cutoff will lead to a disk with more mass that is collisionally more active.

If we fix the number of planetesimals when changing the vapour cutoff fraction, therefore changing the size distribution, this will also affect the collisional activity in the disk as it will change the number of larger planetesimals found in the disk. The larger the planetesimal is, the more likely a collision will occur with it. An increase in mass due to a increase in the vapour cutoff value will also lead to a more collisionally active disk as there will be an increase in larger planetesimals. Though the collisional outcomes will differ depending on what we fix. Fixing

the size distribution will lead to a change in the number of smaller planetesimals which are more easily disrupted at lower impact velocities (at least for planetesimals in the gravity regime). Fixing the number of planetesimals will change the number of larger planetesimals which take greater impact velocities to disrupt. In reality, neither will be fixed and the size distribution of the planetesimals formed from a giant impact will most likely not be a smooth power law. As the size distribution is unknown, we decide to fix it so that the planetesimal disk can be compared to traditional debris disk behaviour.

4.4.4 Gravity

In our N-body simulations of planetesimal disks we have not allowed gravitational interactions between planetesimals to take place. It is a simplification which allowed a much greater compute speed. No gravity between planetesimals would reduce the collision rate within the whole disk. Gravity would act to enlarge the cross-section of each planetesimal due to gravitational focusing, therefore the collisional cross-section of each planetesimal would be larger than the physical size. So with gravity it is like each planetesimal having an inflated radius, with the larger planetesimals having their radii inflated more than the smaller planetesimals. Jackson et al. (2014) has an expression for the collision rate of a single planetesimal as $R_{\rm col} = n\sigma v_{\rm rel}$ where n is the number density, σ is the cross-section and $v_{\rm rel}$ is the velocities of other planetesimals relative to the planetesimal we are measuring the collision rate for. The collision rate varies with a factor of σ, hence we should not expect to find any different behaviour in how the collision rate varies across our simulated disks. We would only expect there to be an initially increased collision rate before decreasing as in eq. 4.2.

4.4.5 The Full Disk

It was proposed by Su et al. (2019) that the flux behaviour seen in ID8 after 2017 could be caused by a planetesimal population from giant impacts which could have occurred at an earlier time in the lightcurve in 2013 and 2014. We discussed the possibility in Watt et al. (2021) (chapter 3) of a planetesimal population and how the fractional luminosity might evolve using the Wyatt (2008) model for debris disks. We assumed that a planetesimal population would take some time to collisionally grind enough material to produce debris to add to the disk. We made a conservative estimate that the process of creating small debris from planetesimals would take 100 orbits.

In this chapter, we have shown that planetesimals can contribute to a debris disk on much shorter timescales. We have found that the planetesimal disk formed from a giant impact is highly destructive with most collision exceeding our criterion for full destruction of both planetesimals in a disk. The collision is tied to the sma which the giant impact occurred at. For a giant impact that occurs between 0.3 and 0.5 au we would expect a highly active planetesimal disk producing a substantial amount of observable dust grains. ID8 has suspected impacts between 0.3 and 0.5 au and therefore the planetesimal disk should be highly active. It is fully possible that the impacts which could have occurred in 2013 and 2014 produced a planetesimal disk which was feeding material to the EDD in 2017.

We have not explored how the vapour condensate disks which we studied in Watt et al. (2021) (chapter 3) and the planetesimal disks will interact. It is possible that the dust added to the EDD from the planetesimals might reduce or wipe out any periodic behaviour in the EDD. It may also enhance the periodic behaviour with planetesimals overwhelmingly colliding at the collision point. Further study is needed on how these two disks interact.

4.5 Conclusions

The aim of this chapter was to better understand how the ejecta from a giant impact formed and evolved EDDs. We focused on the formation of planetesimals post-giant impact from the ejecta and how the mass passed from the planetesimals into small grains which are observable. The idea to study planetesimal activity was spurred on by the behaviour of the lightcurve from ID8 which has a period of increasing excess flux that is not attributed to an impact in 2017. We used a mixed simulation that involved modelling giant impacts using SPH to calculate the ejected mass and distribution. We then assumed that the planetesimals formed from the melted ejecta. We used N-body (REBOUND) to evolve the planetesimal distribution spatially and collisionally.

From the N-body simulations we have shown that planetesimal disks are collisionally active at early times in the disk lifetime. We studied the parameter space varying sma, the giant impact used to form disks, and the orientation of the giant impact. The mass produced in a disk can be different depending on the randomly sampled distribution given to the planetesimal population. Though behaviour and evolution of the planetesimal disk is consistent across all parameters. We provide equations that describe the number of collisions, collision rate and number density at the collision point. The collision point is the dominant location for collisions over the 10^4 orbits for

which we simulated each disk. There is variation in the number of collisions outside the collision point which can affect the mass produced and the collision rate outside the collision point varies with sma. The collision rate outside the collision point is initially linked to the number density around the remnant(s) within the disk. For giant impacts closer to the star, planetesimals need larger kicks in order to escape the influence of the remnants(s). Hence at early times, disks that sit close to the star will have enhanced collision rates not expected from the collision rate given for the collision point. We find that the orientation of a giant impact does affect the collision rate at the collision point, but not as much as varying sma.

We find that the collisionally active disks can have a significant influence on the fractional luminosity of the disk. For disks that sit closer to the star, the larger collision rate produces more mass early on that can pass down to the observable disk. Hence, not only are the disks warmer but there is more mass that can be observable. We show that a planetesimal disk can sustain an EDD on a timescale before the vapour condensate material is removed from the disk. Further study is needed on how the vapour condensate and the dust from the planetesimal collision interact. Especially there is a need to understand how the periodic behaviour of some EDDs is affected by mass being added from a planetesimal population within the disk.

5

Conclusion

5.1 Summary

The main focus of this work was to better understand how giant impacts between planetary embryos influence the detection and evolution of extreme debris disks. It was motivated by the apparent lack of observations for giant impact induced disks which potentially suggested that giant impacts are not common. We investigated extreme debris disk creation and evolution through a combination of SPH simulations using GADGET-2 to measure the ejecta from giant impacts from which we would draw our vapour condensate and planetesimal populations, using N-body codes to evolve the disks spatially and collisionally using my own code and REBOUND, and finally reproducing potential lightcurves for the vapour condensate disks through the radiative transfer code RADMC3D.

Chapter 3 focused on the formation of an EDD from the ejected vaporised material of a giant impact. The work was split into two sections, in the first section a large numerical survey of many giant impacts was conducted. As the work focused on formation of EDDs within the terrestrial zone, planetary embryos of masses between $5 \times 10^{-2} M_{\oplus}$ and $1\ M_{\oplus}$ were modelled. Impact parameters were also varied to sample a large parameter space, the impact velocity was varied from $v_i \sim 6 - 40\ \mathrm{km\ s^{-1}}$, the impact parameter was set to $b = 0,\ 0.4, \mathrm{or}\ 0.8$, and the mass ratio of the two impacting bodies was also varied from $\gamma \sim 0.1 - 1$. From the giant impact simulations the vapour mass of the escaping ejecta was measured and a zeroth order linear relation was found between the mass of the escaping vapour and the specific energy of the impact. Another key result was the discovery that all giant impacts are very anisotropic when it

comes to distributing the escaping material.

We used the distribution of the escaping material to create our initial data for simulating the spatial evolution of vapour condensates. The focus was to understand how the behaviour of periodic variability changed with varying giant impact setups. We simulated disks for 20 orbits with no collisional activity and assuming that the vapour condensate particles would not gravitationally interact. Model lightcurves for each disk were produced using RADMC3D assuming the dust had parameters like dust found in the ISM and that the vapour condensate had a size distribution of $dN \propto D^{-3.5}$ with the maximum and minimum sizes being set to 5 mm and 0.8 μm respectively. We found that the anisotropic distribution of escaping material from the giant impact plays a large role in what behaviour is and is not seen in the lightcurve. Varying the orientation of the giant impact changed the orbital parameter distribution of the vapour condensate particles, with some configurations producing the periodic dips in the lightcurve from the dust passing through the optically thick pinch points at the collision point and anti-collision line while others wiped the variation away as the optically thick points were diminished. It is possible for a giant impact to produce a disk with a lightcurve which does not show periodic variation due to how the giant impact is orientated. We discussed the potential lifetime of grains with a maximum size of 100 μm and 100 mm and how the dust could potentially be replenished. We would expect the vapour condensate to be depleted on a timescale of a few orbits. Something needs to provide mass to the vapour condensate disk in order for the disk to survive for many orbits.

Chapter 4 gives evidence that the boulder population made up of planetesimals ranging in sizes from 10 km to 1000 km will be collisionally active within the disk formed by a giant impact almost instantaneously. The collisions are violent and numerous enough to produce a substantial amount of material which would sustain an EDD past the time when you would expect for the vapour condensates alone to be mostly removed. We show that planetesimal disks formed closer to the star from the same giant impact will be more collisionally active. The increase in collisional activity is due to the increased collision rate at the collision point and also collisions occurring outside the collision point in the first few orbits after the giant impact. For disks placed further away from the star, the collisions outside the collision point are greatly reduced. The change in collision rate outside the collision point occurs because the ratio between the velocity kicks and the Keplerian velocity becomes smaller as the giant impact moves closer to the star. The clumped planetesimals stay on similar orbits to the remnant(s) for longer

allowing the remnant(s) to have an increased influence on the dynamics of the planetesimals in the early disk. The collision rate at the collision point is determined by the initial density of the planetesimal clump which increases with decreasing distance from the star. We showed that orientation also changes the collision rate at the collision point. The orientation had no effect on the collision rate outside of the collision point. We find that the evolution of the collision rate over time is consistent across all varying parameters. The collision rate of different disks are only offset by a factor determined from the initial density of the disk. We finally showed the fractional luminosity estimates of dust produced from planetesimal-planetesimal collisions. The fractional luminosities typically had a sharp increase at the start if the disk was placed close to the star (< 0.5 au), this initial spike shows that a vapour condensate disk can be supplied a substantial amount of material in the time before all the vapour condensate is removed from the disk. The planetesimal population formed from a giant impact can sustain and prolong the observability of EDDs if the giant impact occurs close to the host star.

5.2 Future Work

The work in this thesis can be extended in a few ways: 1) to explore a larger parameter space, 2) model the lightcurve of dust produced from planetesimal collisions, and 3) to model the system as a singular system. We can expand the number and resolution of the SPH giant impact simulations. By switching from GADGET-2 to a new SPH code, Swift (Schaller et al., 2018; Kegerreis et al., 2019), we could greatly increase the impact resolution up to $10^6 - 10^7$ particles. The larger particle resolution would allow us to more precisely measure the vaporised and melted masses. It would also allow us to build a larger planetesimal population found through groupings of particles in the SPH simulations. The relation between vapour mass and specific impact energy could also be extended to improve on the zeroth order estimation of the mass we measured. The parameter space could be extended moving the initial progenitor orbit onto eccentric orbits and changing the placement of the giant impact around an eccentric disk. For the vapour condensate disk we have explored how the periodic behaviour in eccentric disks changes with varying parameters in Lewis et al. (2023). It was found that for increased eccentricity, the position of the giant impact would suppress the periodic variability and hence suppress a key feature used to identify giant impacts. The eccentric disk study can be extended to the planetesimal disk where the collision position would then likely alter the collision rate within the disk.

For extension 2) simple modelling of how the lightcurve varies over time with the addition of mass from destructive planetesimal collisions should be relatively easy to accomplish. It would require the evolution of dust produced from planetesimal-planetesimal collisions to be modelled using an N-body code. Radiative transfer modelling can then be done on the evolved dust. The modelling of radiative transfer for planetesimal produced dust is important as many collisions take place around the location at which the giant impact occurred. The dust produced from planetesimal collisions could prolong the periodic behaviour or even potentially induce it. To carry out this study would require good assumptions on the number and mass of particles produced in planetesimal collisions. Too few and the disk will not be resolved and too many becomes computationally expensive.

Currently we have modelled the EDD formed from a giant impact as two separate disks. We have the vapour condensate disk which produces the initial mass of the observed disk and reproduces behaviours in the lightcurve we would expect. Then we have the boulder populated disk filled with planetesimals. The planetesimals will collide and provide mass to the observed disk over time. In reality these disks will interact with one another. The mass produced from the planetesimals will be collisionally active with the small grains formed from the vapour condensate. It has been proposed that small grains can survive in the disk when below the blowout size if they are shielded within an optically thick clump. Dust produced from planetesimal collisions could add to the optical thickness of the disk potentially prolonging the life of smaller than blowout size grains.

In conclusion, giant impact induced disks can reproduce the behaviour and mass seen within extreme debris disks. Though we also find that these behaviours do not always occur. There is a large variation in the type of behaviour seen dependent on the collision parameters such as location, orientation, impact speed, impact parameter, etc. We find that giant impacts eject material anisotropically and that the orientation of the giant impact with respect to the progenitor orbit will vary the disk structure, collisional activity of planetesimals, and the lightcurve we observe. We expect a boulder population formed from melted material to be collisionally active early on in the disk lifetime which will sustain the vapour condensate disk formed from vapourised escaping material. Giant impacts which occur closer to the star will be more collisionally active and hence more mass will be passed from the boulder population to the observed disk on shorter timescales.

Overall, an observed extreme debris disk is likely to have formed from a giant impact if

it shows sudden increase or decrease in excess flux and shows periodic variability. Though extreme debris disks without any periodic variability should not be discounted from forming via giant impacts as we have shown that many variables can cause supression of the periodic behaviour. The longevity of extreme debris disks is also dependent on the boulder population and how close the giant impact happens to the star. For the formation of an extreme debris disk from masses of a few Mars masses the disk would likely need to sit close to the host star where the timescale for a collisional cascade is decreased. We have shown in one case the collisional activity of the planetesimals within a extreme debris disk could provide material to keep the fractional luminosity above 0.01 for 10-100 years after the giant impact has occurred. Though this is highly dependent on many factors such as total boulder mass, the size distribution of the planetesimals, and the collisional cascade of the debris from the planetesimal-planetesimal collisions. In summary, extreme debris disks formed from giant impacts probably are a common occurrence but the change in lightcurve behaviour over time and the quick depletion of material from the disk make observing giant impact induced extreme debris disks particularly difficult.

Appendix A

Chapter 3 Appendix

A.1 Inverse Distance Weighting

The use of inverse distance weighting is to interpolate the velocity of generated particles from the initial SPH particles to upscale to the required particle resolution we want for the N-body simulations. The velocity of a generated particle, $v(\boldsymbol{x})$, is calculated from,

$$v(\mathbf{x}) = \frac{\Sigma_{i=1}^{N} w_i(\mathbf{x}) v_i}{\Sigma_{i=1}^{N} w_i(\mathbf{x})},$$

where

$$w_i(\mathbf{x}) = \frac{1}{d(\mathbf{x}, \mathbf{x}_i)^3},$$

here the weight, $w_i(\mathbf{x})$, of the velocity of particle i, v_i, is calculated from the inverse of the distance between the generated particle and particle i cubed. We choose to cube the distance so the velocity of the generated particle is strongly influenced by the particles close by. $v(\mathbf{x})$ is calculated from the original SPH particle and its 4 closest neighbours. Figure A.1 shows an example of the generated N-body (blue) distribution against the original Gadget-2 (black) distribution of particles for sim 8 in table A.1 for the absolute velocity versus the distance from the origin. The origin here is defined as the centre of mass between the largest and second largest remnants post-impact. The figure shows that our generated data matches the original data well.

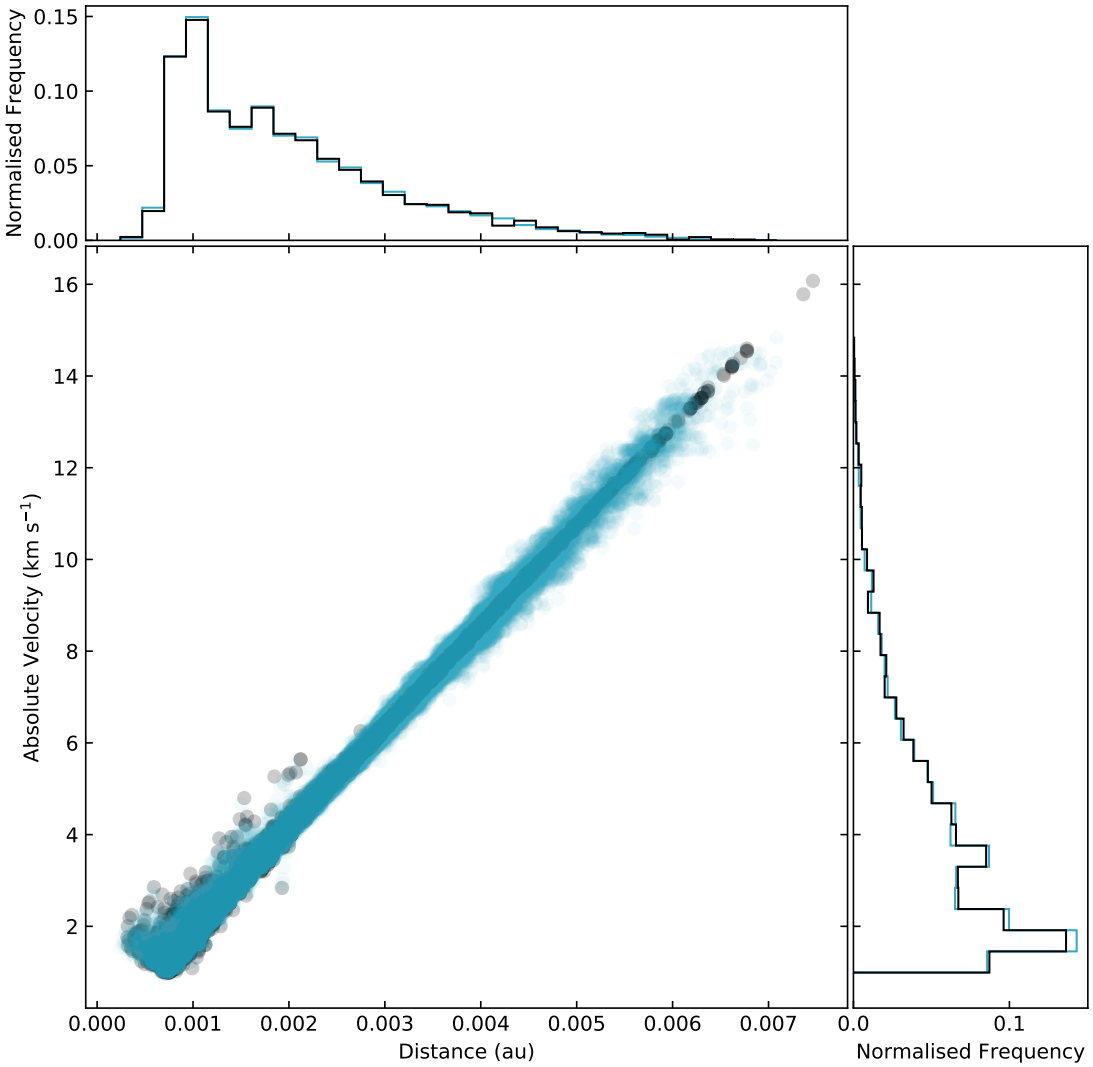

Figure A.1: Compares the distribution of absolute velocity versus the distance from the origin for particles escaping the giant impact in Gadget-2 simulation (black) and the generated upscaled particles in the N-body code (blue). The origin is defined as the centre of mass of the largest and second largest remnants. Data used from sim 8 which is a giant impact between two 0.1 $M_{\oplus}$ embryos at an impact velocity of 10 $\mathrm{km\ s^{-1}}$ and at $b = 0$.

A.2 Full SPH Simulation Results

Below are the full results of the SPH simulations used in this paper. The data has been split into two tables; the table A.1 shows results for impacts with a total mass less than 1 $M_{\oplus}$, table A.2 shows impacts with a total mass greater than or equal to 1 $M_{\oplus}$.

Table A.1: Summary of all parameters and results from SPH simulations for masses below $1\mathrm{M}_{\oplus}$. $\mathrm{M_{tot}}$ − total mass in collision in earth masses; $\mathrm{M_{targ}/M_{proj}}$ − mass ratio of target mass to projectile mass; N − number of particles in the simulation; v_i − impact velocity in $\mathrm{km\ s^{-1}}$; v_i/v_{esc} − impact velocity normalised by mutual escape velocity; b− impact parameter; $\mathrm{M_{lr}/M_{tot}}$ − ratio of largest remnant mass to total mass; $\mathrm{M_{unb}/M_{tot}}$ − ratio of escaping mass to total mass; $\mathrm{M_{vap}/M_{tot}}$ − ratio of escaping vapour mass to total mass; $Q_{\mathrm{R}}/Q^*_{\mathrm{RD}}$ − specific impact energy normalised by the catastrophic disruption threshold.

* Q^*_{RD} is calculated from interpolating Q_{R} values either side of a giant impact having M_{lr} larger ans smaller than half the total mass.

† Q^*_{RD} is calculated using methods outlined in Leinhardt & Stewart 2012 using the interpolated Q^*_{RD} value as a base.

The rest were calculated using methods outlined in Leinhardt & Stewart 2012.

Index	$\mathrm{M_{tot}}$	$\mathrm{M_{proj}/M_{targ}}$	N	v_i	v_i/v_{esc}	b	$\mathrm{M_{lr}/M_{tot}}$	$\mathrm{M_{unb}/M_{tot}}$	$\mathrm{M_{vap}/M_{tot}}$	$Q_{\mathrm{R}}/Q^*_{\mathrm{RD}}$
–	$\mathrm{M_{\oplus}}$	–	10^4	$\mathrm{km\ s^{-1}}$	–	–	–	–	10^{-2}	–
1	0.19	0.561	6.0	5.6	1.11	0.0	0.95	0.05	0.80	0.196
2	0.19	0.561	6.0	6.7	1.33	0.0	0.91	0.09	1.28	0.280
3	0.19	0.561	6.0	7.1	1.41	0.0	0.89	0.11	1.55	0.315
4	0.19	0.561	6.0	8.0	1.59	0.0	0.84	0.16	2.33	0.400
5	0.19	0.561	6.0	8.8	1.75	0.0	0.77	0.23	2.72	0.484
6	0.19	0.561	6.0	9.8	1.95	0.0	0.70	0.29	3.65	0.600
7	0.20	1.000	4.0	9.7	1.93	0.0	0.67	0.33	4.20	0.560*
8	0.20	1.000	4.0	10.0	1.99	0.0	0.73	0.26	3.34	0.596*
9	0.20	1.000	4.0	12.0	2.38	0.0	0.55	0.44	6.45	0.858*
10	0.20	1.000	4.0	14.0	2.78	0.0	0.44	0.56	9.94	1.167*
11	0.20	1.000	4.0	15.0	2.98	0.0	0.38	0.62	12.11	1.340*

Table A.1

Index	M_{tot}	M_{proj}/M_{targ}	N	v_i	v_i/v_{esc}	b	M_{lr}/M_{tot}	M_{unb}/M_{tot}	M_{vap}/M_{tot}	Q_R/Q^*_{RD}
–	$M_\oplus$	–	10^4	km s^{-1}	–	–	–	–	10^{-2}	–
12	0.24	1.000	20.0	5.6	1.03	0.0	0.95	0.05	0.71	0.193
13	0.24	1.000	20.0	6.6	1.21	0.0	0.91	0.09	1.40	0.269
14	0.24	1.000	20.0	7.1	1.30	0.0	0.89	0.11	1.92	0.311
15	0.24	1.000	20.0	7.9	1.45	0.0	0.85	0.15	2.90	0.385
16	0.24	1.000	20.0	8.6	1.58	0.0	0.82	0.18	2.77	0.456
17	0.24	1.000	20.0	9.7	1.78	0.0	0.72	0.27	3.44	0.580
18	0.32	0.262	12.0	7.9	1.27	0.0	0.97	0.03	0.80	0.145
19	0.32	0.262	12.0	9.4	1.52	0.0	0.93	0.07	1.48	0.205
20	0.32	0.262	12.0	10.0	1.61	0.0	0.92	0.08	1.85	0.232
21	0.32	0.262	12.0	11.2	1.81	0.0	0.87	0.12	2.60	0.291
22	0.32	0.262	12.0	12.3	1.98	0.0	0.81	0.18	3.21	0.351
23	0.32	0.262	12.0	13.8	2.23	0.0	0.74	0.26	4.66	0.442
24	0.38	0.466	14.0	7.3	1.13	0.0	0.95	0.05	1.30	0.187
25	0.38	0.466	14.0	8.7	1.35	0.0	0.92	0.08	2.08	0.265
26	0.38	0.466	14.0	9.3	1.45	0.0	0.89	0.11	2.99	0.303
27	0.38	0.358	7.0	10.0	1.54	0.0	0.93	0.07	1.41	0.255*
28	0.38	0.466	14.0	10.4	1.62	0.0	0.85	0.15	3.05	0.379
29	0.38	0.466	14.0	11.4	1.77	0.0	0.77	0.23	4.25	0.456
30	0.38	0.466	14.0	12.7	1.97	0.0	0.68	0.32	5.88	0.566

Table A.1

Index	M_{tot}	M_{proj}/M_{targ}	N	v_i	v_i/v_{esc}	b	M_{lr}/M_{tot}	M_{unb}/M_{tot}	M_{vap}/M_{tot}	Q_R/Q^*_{RD}
–	$M_\oplus$	–	10^4	km s^{-1}	–	–	–	–	10^{-2}	–
31	0.38	0.358	7.0	15.0	2.31	0.0	0.69	0.31	6.59	0.574*
32	0.38	0.358	7.0	17.0	2.62	0.0	0.62	0.38	8.81	0.737*
33	0.38	0.358	7.0	20.0	3.08	0.0	0.49	0.51	13.57	1.020*
34	0.56	1.000	10.0	5.2	0.70	0.0	0.96	0.04	2.37	0.095
35	0.56	1.000	10.0	7.4	1.00	0.0	0.94	0.06	2.41	0.193
36	0.56	1.000	10.0	9.0	1.21	0.0	0.89	0.10	3.38	0.286
37	0.56	1.000	10.0	10.0	1.35	0.0	0.93	0.07	2.10	0.353
38	0.56	1.000	10.0	10.4	1.40	0.0	0.85	0.15	3.66	0.381
39	0.56	1.000	10.0	15.0	2.02	0.0	0.69	0.31	7.49	0.793
40	0.62	0.190	12.0	10.0	1.26	0.0	0.99	0.01	0.43	0.103
41	0.62	0.190	12.0	15.0	1.90	0.0	0.91	0.09	2.56	0.232
42	0.80	0.531	15.0	10.0	1.17	0.0	0.97	0.03	1.21	0.207*
43	0.80	0.531	15.0	15.0	1.76	0.0	0.81	0.19	5.10	0.465*
44	0.80	0.531	15.0	18.9	2.22	0.0	0.64	0.36	10.85	0.738*
45	0.80	0.531	15.0	23.2	2.73	0.0	0.44	0.56	18.17	1.112*
46	0.87	0.129	17.0	10.0	1.10	0.0	0.99	0.01	0.35	0.049
47	0.87	0.129	17.0	15.0	1.66	0.0	0.97	0.03	0.83	0.110
48	0.19	0.561	6.0	6.3	1.25	0.4	0.93	0.07	1.01	0.182
49	0.19	0.561	6.0	7.5	1.49	0.4	0.88	0.12	0.93	0.258

Table A.1

Index	M_{tot}	M_{proj}/M_{targ}	N	v_i	v_i/v_{esc}	b	M_{lr}/M_{tot}	M_{unb}/M_{tot}	M_{vap}/M_{tot}	Q_R/Q^*_{RD}
–	$M_\oplus$	–	10^4	km s^{-1}	–	–	–	–	10^{-2}	–
50	0.19	0.561	6.0	8.0	1.59	0.4	0.62	0.13	1.08	0.293
51	0.19	0.561	6.0	8.9	1.77	0.4	0.59	0.17	1.45	0.363
52	0.19	0.561	6.0	9.8	1.95	0.4	0.57	0.21	2.00	0.440
53	0.19	0.561	6.0	10.9	2.17	0.4	0.53	0.26	2.70	0.545
54	0.20	1.000	4.0	10.0	1.99	0.4	0.40	0.19	1.86	0.418†
55	0.20	1.000	4.0	15.0	2.98	0.4	0.26	0.48	7.23	0.940†
56	0.24	1.000	20.0	6.7	1.23	0.4	0.93	0.07	1.62	0.195
57	0.24	1.000	20.0	7.9	1.45	0.4	0.89	0.11	1.32	0.271
58	0.24	1.000	20.0	8.4	1.54	0.4	0.44	0.12	1.52	0.306
59	0.24	1.000	20.0	9.4	1.72	0.4	0.40	0.18	1.73	0.384
60	0.24	1.000	20.0	10.3	1.89	0.4	0.36	0.27	2.46	0.461
61	0.24	1.000	20.0	11.5	2.11	0.4	0.32	0.33	3.41	0.574
62	0.32	0.262	12.0	7.7	1.24	0.4	0.95	0.05	0.68	0.113
63	0.32	0.262	12.0	9.1	1.47	0.4	0.92	0.08	1.25	0.158
64	0.32	0.262	12.0	9.7	1.56	0.4	0.90	0.10	1.71	0.179
65	0.32	0.262	12.0	10.9	1.76	0.4	0.80	0.11	1.55	0.226
66	0.32	0.262	12.0	11.9	1.92	0.4	0.76	0.14	1.99	0.270
67	0.32	0.262	12.0	13.3	2.15	0.4	0.73	0.17	2.71	0.337
68	0.38	0.466	14.0	8.0	1.24	0.4	0.92	0.07	1.69	0.168

Table A.1

Index	M_{tot}	M_{proj}/M_{targ}	N	v_i	v_i/v_{esc}	b	M_{lr}/M_{tot}	M_{unb}/M_{tot}	M_{vap}/M_{tot}	Q_R/Q^*_{RD}
–	$M_\oplus$	–	10^4	km s^{-1}	–	–	–	–	10^{-2}	–
69	0.38	0.466	14.0	9.5	1.48	0.4	0.90	0.10	1.29	0.236
70	0.38	0.358	7.0	10.0	1.54	0.4	0.91	0.09	1.33	0.189†
71	0.38	0.466	14.0	10.2	1.58	0.4	0.68	0.12	1.71	0.272
72	0.38	0.466	14.0	11.4	1.77	0.4	0.65	0.17	2.40	0.340
73	0.38	0.466	14.0	12.5	1.94	0.4	0.62	0.20	3.08	0.409
74	0.38	0.466	14.0	13.9	2.16	0.4	0.58	0.25	4.22	0.506
75	0.38	0.358	7.0	15.0	2.31	0.4	0.67	0.23	3.98	0.424†
76	0.56	1.000	10.0	10.0	1.35	0.4	0.95	0.05	1.73	0.248
77	0.56	1.000	10.0	15.0	2.02	0.4	0.38	0.24	4.44	0.559
78	0.62	0.190	12.0	10.0	1.26	0.4	0.97	0.03	0.43	0.085
79	0.62	0.190	12.0	15.0	1.90	0.4	0.90	0.10	1.94	0.191
80	0.80	0.531	15.0	10.0	1.17	0.4	0.97	0.03	0.95	0.150†
81	0.80	0.531	15.0	15.0	1.76	0.4	0.65	0.13	2.75	0.338†
82	0.87	0.129	17.0	10.0	1.10	0.4	0.99	0.01	0.24	0.043
83	0.87	0.129	17.0	15.0	1.66	0.4	0.95	0.05	1.07	0.097
84	0.19	0.561	6.0	16.9	3.36	0.8	0.60	0.10	1.16	0.146
85	0.19	0.561	6.0	19.9	3.96	0.8	0.59	0.12	1.74	0.203
86	0.19	0.561	6.0	21.3	4.24	0.8	0.59	0.14	2.04	0.233
87	0.19	0.561	6.0	23.8	4.73	0.8	0.58	0.16	2.64	0.291

Table A.1

Index	M_{tot}	M_{proj}/M_{targ}	N	v_i	v_i/v_{esc}	b	M_{lr}/M_{tot}	M_{unb}/M_{tot}	M_{vap}/M_{tot}	Q_R/Q^*_{RD}
–	$M_\oplus$	–	10^4	km s^{-1}	–	–	–	–	10^{-2}	–
88	0.19	0.561	6.0	26.1	5.19	0.8	0.57	0.18	3.30	0.349
89	0.19	0.561	6.0	29.2	5.81	0.8	0.55	0.21	4.30	0.437
90	0.20	1.000	4.0	10.0	1.99	0.8	0.48	0.04	0.19	0.051†
91	0.20	1.000	4.0	15.0	2.98	0.8	0.46	0.07	0.70	0.114†
92	0.24	1.000	20.0	18.9	3.46	0.8	0.45	0.10	1.42	0.192
93	0.24	1.000	20.0	22.3	4.09	0.8	0.44	0.13	2.22	0.268
94	0.24	1.000	20.0	23.9	4.38	0.8	0.43	0.14	2.62	0.308
95	0.24	1.000	20.0	26.7	4.89	0.8	0.42	0.16	3.42	0.384
96	0.24	1.000	20.0	29.3	5.37	0.8	0.41	0.19	4.28	0.462
97	0.24	1.000	20.0	32.7	5.99	0.8	0.39	0.23	5.51	0.576
98	0.32	0.262	12.0	18.7	3.02	0.8	0.77	0.09	1.23	0.072
99	0.32	0.262	12.0	22.1	3.56	0.8	0.77	0.10	1.76	0.100
100	0.32	0.262	12.0	23.6	3.81	0.8	0.76	0.11	2.03	0.114
101	0.32	0.262	12.0	26.4	4.26	0.8	0.76	0.13	2.62	0.143
102	0.32	0.262	12.0	28.9	4.66	0.8	0.75	0.15	3.22	0.172
103	0.32	0.262	12.0	32.3	5.21	0.8	0.74	0.17	4.15	0.214
104	0.38	0.358	7.0	10.0	1.54	0.8	0.75	0.02	0.15	0.019†
105	0.38	0.358	7.0	15.0	2.31	0.8	0.73	0.05	0.59	0.043†
106	0.38	0.466	14.0	21.1	3.28	0.8	0.65	0.10	1.71	0.127

Table A.1

Index	M_{tot}	M_{proj}/M_{targ}	N	v_i	v_i/v_{esc}	b	M_{lr}/M_{tot}	M_{unb}/M_{tot}	M_{vap}/M_{tot}	Q_R/Q^*_{RD}
–	$M_\oplus$	–	10^4	km s^{-1}	–	–	–	–	10^{-2}	–
107	0.38	0.466	14.0	24.9	3.87	0.8	0.64	0.12	2.48	0.177
108	0.38	0.466	14.0	26.6	4.13	0.8	0.64	0.13	2.87	0.202
109	0.38	0.466	14.0	29.8	4.63	0.8	0.63	0.15	3.67	0.254
110	0.38	0.466	14.0	32.6	5.07	0.8	0.62	0.18	4.63	0.304
111	0.56	1.000	10.0	10.0	1.35	0.8	0.50	0.01	0.10	0.031
112	0.56	1.000	10.0	15.0	2.02	0.8	0.48	0.04	0.51	0.069
113	0.62	0.190	12.0	10.0	1.26	0.8	0.87	0.01	0.13	0.009
114	0.62	0.190	12.0	15.0	1.90	0.8	0.85	0.03	0.46	0.020
115	0.62	0.190	12.0	16.5	2.09	0.8	0.84	0.06	0.98	0.024
116	0.62	0.190	12.0	23.4	2.96	0.8	0.83	0.09	1.84	0.048
117	0.62	0.190	12.0	28.6	3.61	0.8	0.82	0.11	2.67	0.072
118	0.62	0.190	12.0	33.0	4.17	0.8	0.81	0.13	3.53	0.096
119	0.62	0.190	12.0	36.9	4.66	0.8	0.80	0.15	4.50	0.119
120	0.80	0.531	15.0	10.0	1.17	0.8	0.67	0.00	0.07	0.016†
121	0.80	0.531	15.0	15.0	1.76	0.8	0.65	0.03	0.38	0.036†
122	0.80	0.531	15.0	19.5	2.29	0.8	0.63	0.06	1.26	0.061†
123	0.80	0.531	15.0	27.6	3.24	0.8	0.62	0.09	2.58	0.123†
124	0.80	0.531	15.0	33.8	3.97	0.8	0.61	0.12	3.94	0.184†
125	0.80	0.531	15.0	39.0	4.58	0.8	0.59	0.16	5.54	0.245†
126	0.87	0.129	17.0	10.0	1.10	0.8	0.93	0.01	0.19	0.005
127	0.87	0.129	17.0	15.0	1.66	0.8	0.90	0.04	0.49	0.010

Table A.2: Summary of all parameters and results from SPH simulations for masses equal to or greater than $1 M_{\oplus}$

Index	M_{tot}	M_{proj}/M_{targ}	N	v_i	v_i/v_{esc}	b	M_{lr}/M_{tot}	M_{unb}/M_{tot}	M_{vap}/M_{tot}	Q_R/Q^*_{RD}
–	$M_{\oplus}$	–	10^4	km s^{-1}	–	–	–	–	10^{-2}	–
128	1.05	1.000	20.0	6.4	0.69	0.0	0.96	0.04	2.58	0.082*
129	1.05	1.000	20.0	9.1	0.98	0.0	0.94	0.06	2.87	0.165*
130	1.05	1.000	20.0	10.0	1.07	0.0	0.97	0.03	1.40	0.200*
131	1.05	0.360	20.0	10.0	1.06	0.0	0.98	0.02	1.28	0.145
132	1.05	1.000	20.0	11.2	1.20	0.0	0.89	0.11	4.16	0.251*
133	1.05	1.000	20.0	12.9	1.38	0.0	0.84	0.16	5.38	0.333*
134	1.05	0.360	20.0	15.0	1.59	0.0	0.91	0.09	3.14	0.327
135	1.05	1.000	20.0	15.0	1.61	0.0	0.83	0.17	5.41	0.450*
136	1.05	1.000	20.0	18.6	1.99	0.0	0.67	0.33	10.12	0.691*
137	1.05	1.000	20.0	22.8	2.45	0.0	0.48	0.52	18.32	1.039*
138	1.05	0.360	20.0	24.7	2.61	0.0	0.58	0.42	14.41	0.887
139	1.21	0.090	22.0	10.0	0.97	0.0	1.00	0.00	0.21	0.023
140	1.21	0.090	22.0	15.0	1.46	0.0	0.99	0.01	0.37	0.051
141	1.29	0.679	25.0	10.0	0.99	0.0	0.97	0.03	1.79	0.159*
142	1.29	0.679	25.0	15.0	1.49	0.0	0.89	0.11	4.31	0.358*
143	1.29	0.679	25.0	25.4	2.52	0.0	0.48	0.51	18.47	1.026*
144	1.39	0.250	25.0	10.0	0.95	0.0	0.99	0.01	0.58	0.084
145	1.39	0.250	25.0	15.0	1.42	0.0	0.96	0.04	1.64	0.188

Table A.2

Index	M_{tot}	M_{proj}/M_{targ}	N	v_i	v_i/v_{esc}	b	M_{lr}/M_{tot}	M_{unb}/M_{tot}	M_{vap}/M_{tot}	Q_R/Q^*_{RD}
–	$M_\oplus$	–	10^4	km s^{-1}	–	–	–	–	10^{-2}	–
146	1.54	1.000	30.0	10.0	0.93	0.0	0.97	0.03	1.96	0.152*
147	1.54	1.000	30.0	15.0	1.40	0.0	0.90	0.10	4.34	0.341*
148	1.54	1.000	30.0	21.2	1.97	0.0	0.67	0.33	11.35	0.681*
149	1.54	1.000	30.0	25.9	2.41	0.0	0.49	0.51	19.20	1.017*
150	1.63	0.471	30.0	10.0	0.91	0.0	0.98	0.02	1.43	0.133
151	1.63	0.471	30.0	15.0	1.36	0.0	0.93	0.07	2.92	0.299
152	1.63	0.471	30.0	25.1	2.28	0.0	0.62	0.38	13.44	0.837
153	1.88	0.694	35.0	10.0	0.87	0.0	0.97	0.03	2.23	0.136*
154	1.88	0.694	35.0	23.4	2.03	0.0	0.65	0.35	12.77	0.744*
155	1.88	0.694	35.0	28.7	2.49	0.0	0.43	0.57	21.83	1.119*
156	2.22	1.000	40.0	23.9	1.96	0.0	0.66	0.34	12.70	0.799
157	1.05	1.000	20.0	10.0	1.07	0.4	0.98	0.02	1.09	0.140†
158	1.05	0.360	20.0	10.0	1.06	0.4	0.98	0.02	0.60	0.111
159	1.05	0.360	20.0	15.0	1.59	0.4	0.91	0.09	2.36	0.249
160	1.05	1.000	20.0	15.0	1.61	0.4	0.45	0.10	2.36	0.315†
161	1.21	0.090	22.0	10.0	0.97	0.4	1.00	0.00	0.12	0.021
162	1.21	0.090	22.0	15.0	1.46	0.4	0.98	0.02	0.63	0.048
163	1.29	0.679	25.0	10.0	0.99	0.4	0.98	0.02	0.99	0.113†
164	1.29	0.679	25.0	15.0	1.49	0.4	0.90	0.10	3.59	0.254†

Table A.2

Index	M_{tot}	M_{proj}/M_{targ}	N	v_i	v_i/v_{esc}	b	M_{lr}/M_{tot}	M_{unb}/M_{tot}	M_{vap}/M_{tot}	Q_R/Q^*_{RD}
–	$M_\oplus$	–	10^4	km s^{-1}	–	–	–	–	10^{-2}	–
165	1.39	0.250	25.0	10.0	0.95	0.4	0.99	0.01	0.40	0.068
166	1.39	0.250	25.0	15.0	1.42	0.4	0.94	0.06	1.64	0.153
167	1.54	1.000	30.0	10.0	0.93	0.4	0.99	0.01	1.05	0.106†
168	1.54	1.000	30.0	15.0	1.40	0.4	0.94	0.06	2.88	0.239†
169	1.63	0.471	30.0	10.0	0.91	0.4	0.99	0.01	0.67	0.098
170	1.63	0.471	30.0	15.0	1.36	0.4	0.93	0.07	2.47	0.221
171	1.88	0.694	35.0	10.0	0.87	0.4	0.99	0.01	0.89	0.097†
172	1.88	0.694	35.0	15.0	1.30	0.4	0.95	0.05	2.21	0.218†
173	2.22	1.000	40.0	10.0	0.82	0.4	0.99	0.01	1.07	0.099
174	2.22	1.000	40.0	15.0	1.23	0.4	0.97	0.03	1.82	0.222
175	1.05	1.000	20.0	10.0	1.07	0.8	0.50	0.00	0.04	0.017†
176	1.05	0.360	20.0	10.0	1.06	0.8	1.00	0.00	0.09	0.012
177	1.05	0.360	20.0	15.0	1.59	0.8	0.74	0.02	0.35	0.026
178	1.05	1.000	20.0	15.0	1.61	0.8	0.49	0.02	0.33	0.038†
179	1.21	0.090	22.0	10.0	0.97	0.8	0.98	0.01	0.22	0.002
180	1.21	0.090	22.0	15.0	1.46	0.8	0.93	0.03	0.47	0.006
181	1.21	0.090	22.0	18.3	1.78	0.8	0.92	0.06	1.20	0.008
182	1.21	0.090	22.0	25.8	2.50	0.8	0.91	0.08	1.87	0.016
183	1.21	0.090	22.0	31.7	3.08	0.8	0.91	0.09	2.43	0.025

Table A.2

Index	M_{tot}	M_{proj}/M_{targ}	N	v_i	v_i/v_{esc}	b	M_{lr}/M_{tot}	M_{unb}/M_{tot}	M_{vap}/M_{tot}	Q_R/Q^*_{RD}
–	$M_\oplus$	–	10^4	km s^{-1}	–	–	–	–	10^{-2}	–
184	1.29	0.679	25.0	10.0	0.99	0.8	0.99	0.01	0.64	0.013†
185	1.29	0.679	25.0	15.0	1.49	0.8	0.60	0.02	0.30	0.028†
186	1.39	0.250	25.0	10.0	0.95	0.8	0.99	0.01	0.35	0.007
187	1.39	0.250	25.0	15.0	1.42	0.8	0.81	0.02	0.36	0.016
188	1.54	1.000	30.0	10.0	0.93	0.8	0.99	0.01	0.97	0.013†
189	1.54	1.000	30.0	15.0	1.40	0.8	0.49	0.01	0.27	0.029†
190	1.63	0.471	30.0	10.0	0.91	0.8	0.99	0.01	0.44	0.011
191	1.63	0.471	30.0	15.0	1.36	0.8	0.69	0.01	0.29	0.024
192	1.88	0.694	35.0	10.0	0.87	0.8	0.99	0.01	0.49	0.011†
193	1.88	0.694	35.0	15.0	1.30	0.8	0.59	0.01	0.27	0.025†
194	2.22	1.000	40.0	10.0	0.82	0.8	0.99	0.01	0.52	0.012
195	2.22	1.000	40.0	15.0	1.23	0.8	0.50	0.01	0.22	0.028

Appendix B

Chapter 4 Appendix

Table B.1: Summary of the set up values used to equilibrate planetary embryos used in the giant impact SPH simulations. GI Index indicates what embryo was used in giant impacts listed in Table 4.1; $N_{\rm tot}$ is the number of SPH particles in the embryo; Mass is the mass of the embryo in 10^{-1} Earth masses; Radius is the radius of the embryo in 10^{-1} Earth radii; $S_{\rm core}$ is the specific entropy set for the core entropy cooling in 10^7 ergs $\rm g^{-1}$ $\rm K^{-1}$; $S_{\rm mantle}$ is the specific entropy set for the mantle entropy cooling in 10^7 ergs $\rm g^{-1}$ $\rm K^{-1}$; $T_{\rm forced}$ is the equilibration time with specific entropy values and velocity dampening is forced in 10^4s; $T_{\rm equil}$ is the equilibration time without any forced values in 10^4s.

Index	GI Index	$N_{\rm tot}$	Mass	Radius	$S_{\rm core}$	$S_{\rm mantle}$	$T_{\rm forced}$	$T_{\rm equil}$
–	–	–	10^{-1} $\rm M_\oplus$	$10^{-1}\rm R_\oplus$	10^7 ergs $\rm g^{-1}$ /rm$\rm K^{-1}$	10^7 ergs $\rm g^{-1}$ $\rm K^{-1}$	10^4s	10^4s
1	1	200000	1.185	5.242	1.58	2.24	7.2	7.2
2	2	285715	2.525	6.648	1.61	2.30	5.0	2.6
3	2	114285	1.185	5.214	1.58	2.24	3.0	2.0
4	3	20000	0.995	4.879	1.36	2.74	7.2	7.2

Table B.2: Summary of planetesimal disk set up and results from Rebound simulations. GI Index is the giant impact reference to the giant impact used to set up the disk in table 4.1; $N_{\rm tot}-$ total number of planetesimals in the simulation; $M_{\rm des}-$ the total mass produced in the simulation through destructive planetesimal-planetesimal collisions; sma - the semi-major axis the giant impact occurred at to set up the disk; rot - the orientation of the giant impact when setting up the disk; $N_{\rm p-p}-$ the number of planetesimal-planetesimal collisions; %des - the percentage of destructive collisions between planetesimals; %bounce - the percentage of bouncing collisions between planetesimals; %merge - the percentage of merging collisions between planetesimals; $N_{\rm lr-p}-$ the number of collisions between the remnant(s) and planetesimals.

Index	GI Index	$N_{\rm tot}$	$M_{\rm des}$	sma	rot	$N_{\rm p-p}$	%des	%bounce	%merge	$N_{\rm lr-p}$
–	–	–	$10^{-5}{\rm M}_\oplus$	au	π	–	–	–	–	–
1	1	19845	360.73	0.30	0.00	818	78.24	15.77	5.99	533
2	1	19845	383.87	0.30	0.50	1371	65.21	10.14	24.65	725
3	1	19845	79.83	0.50	0.00	262	74.05	19.85	6.11	308
4	1	19845	56.01	0.50	0.00	187	79.14	9.09	11.76	261
5	1	19845	80.92	0.50	0.00	255	78.82	13.33	7.84	243
6	1	19845	76.18	0.50	0.00	198	78.28	16.16	5.56	230
7	1	19845	74.86	0.50	0.00	259	73.36	18.92	7.72	313
8	1	19845	77.10	0.50	0.00	209	68.42	11.96	19.62	285
9	1	19845	61.73	0.50	0.00	259	76.45	16.22	7.34	251
10	1	19845	118.98	0.50	0.00	302	78.15	16.56	5.30	303
11	1	19845	76.07	0.50	0.00	261	75.48	17.62	6.90	219
12	1	19845	93.00	0.50	0.00	227	74.45	14.98	10.57	245
13	1	19845	152.36	0.50	0.50	412	75.97	11.65	12.38	245
14	1	19845	176.33	0.50	0.50	512	77.15	13.87	8.98	382
15	1	19845	298.34	0.50	0.50	422	81.99	11.85	6.16	404
16	1	19845	195.60	0.50	0.50	431	72.16	16.71	11.14	345
17	1	19845	206.13	0.50	0.50	517	72.53	13.35	14.12	350
18	1	19845	200.93	0.50	0.50	469	82.94	12.37	4.69	356
19	1	19845	158.00	0.50	0.50	396	80.05	8.59	11.36	351

Table B.2

Index	GI Index	$N_{\rm tot}$	$M_{\rm des}$	sma	rot	$N_{\rm p-p}$	%des	%bounce	%merge	$N_{\rm lr-p}$
–	–	–	$10^{-5}{\rm M}_\oplus$	au	π	–	–	–	–	–
20	1	19845	249.36	0.50	0.50	521	78.12	12.86	9.02	448
21	1	19845	209.90	0.50	0.50	335	75.82	19.40	4.78	99
22	1	19845	218.94	0.50	0.50	581	67.30	14.80	17.90	241
23	1	19845	183.65	0.50	0.50	483	72.46	20.70	6.83	331
24	1	19845	211.63	0.50	0.50	488	77.25	12.91	9.84	383
25	1	19845	148.49	0.50	0.50	424	79.48	11.56	8.96	302
26	1	19845	148.27	0.50	0.50	465	79.35	13.98	6.67	416
27	1	19845	215.02	0.50	0.50	452	83.41	11.28	5.31	328
28	1	19845	144.07	0.50	0.50	523	71.89	15.11	13.00	388
29	1	19845	163.25	0.50	0.50	525	77.71	15.43	6.86	373
30	1	19845	205.85	0.50	0.50	563	73.53	19.89	6.57	312
31	1	19845	182.74	0.50	0.50	481	82.33	11.02	6.65	380
32	1	19845	172.12	0.50	0.50	733	68.76	23.74	7.50	402
33	1	19845	186.81	0.50	0.50	636	67.45	15.57	16.98	362
34	1	19845	207.42	0.50	0.50	453	77.04	12.14	10.82	308
35	1	19845	155.72	0.50	0.50	457	75.27	11.82	12.91	310
36	1	19845	137.74	0.50	0.50	479	80.38	15.24	4.38	374
37	1	19845	166.40	0.50	0.50	476	84.03	12.39	3.57	346
38	1	19845	207.93	0.50	0.50	576	74.13	17.19	8.68	373
39	1	19845	312.64	0.50	0.50	1335	62.77	26.82	10.41	370
40	1	19845	140.96	0.50	0.50	420	77.62	14.29	8.10	477
41	1	19845	167.36	0.50	0.50	464	77.16	13.36	9.48	292
42	1	19845	215.60	0.50	0.50	763	64.35	14.29	21.36	286
43	1	19845	200.43	0.50	0.50	525	77.71	14.86	7.43	316
44	1	19845	119.73	0.50	0.50	434	73.27	12.44	14.29	354
45	1	19845	166.46	0.50	0.50	532	73.87	19.36	6.77	406
46	1	19845	138.18	0.50	0.50	447	76.73	15.66	7.61	377
47	1	19845	225.87	0.50	0.50	735	62.99	17.01	20.00	334

Table B.2

Index	GI Index	$N_{\rm tot}$	$M_{\rm des}$	sma	rot	$N_{\rm p-p}$	%des	%bounce	%merge	$N_{\rm lr-p}$
–	–	–	$10^{-5}{\rm M}_{\oplus}$	au	π	–	–	–	–	–
48	1	19845	137.91	0.50	0.50	433	76.44	16.17	7.39	404
49	1	19845	212.88	0.50	0.50	521	71.79	20.92	7.29	332
50	1	19845	156.07	0.50	0.50	413	80.63	14.04	5.33	353
51	1	19845	174.44	0.50	0.50	579	77.72	15.20	7.08	356
52	1	19845	201.52	0.50	0.50	605	77.02	17.69	5.29	373
53	1	19845	30.04	0.75	0.00	102	83.33	8.82	7.84	138
54	1	19845	64.25	0.75	0.50	180	79.44	11.67	8.89	75
55	1	19845	22.85	1.00	0.00	50	80.00	8.00	12.00	93
56	1	19845	57.72	1.00	0.50	144	84.72	11.11	4.17	137
57	1	19845	2.56	2.00	0.00	12	75.00	16.67	8.33	21
58	1	19845	8.40	2.00	0.50	34	82.35	11.76	5.88	55
59	2	12559	34.34	0.50	0.50	86	72.09	18.60	9.30	58
60	2	12559	33.61	0.50	0.50	79	75.95	11.39	12.66	55
61	2	12559	40.90	0.50	0.50	87	66.67	22.99	10.34	86
62	2	12559	42.37	0.50	0.50	76	75.00	14.47	10.53	68
63	2	12559	52.90	0.50	0.50	112	68.75	16.07	15.18	55
64	3	13545	209.94	0.50	0.50	418	77.75	11.72	10.53	193

Bibliography

Ahrens T. J., Love S. G., 1996, in Lunar and Planetary Science Conference. p. 1

Amelin Y., Kaltenbach A., Iizuka T., Stirling C. H., Ireland T. R., Petaev M., Jacobsen S. B., 2010, Earth and Planetary Science Letters, 300, 343

Artymowicz P., 1997, Annual Review of Earth and Planetary Sciences, 25, 175

Aumann H. H., et al., 1984, ApJ, 278, L23

Balog Z., Kiss L. L., Vinkó J., Rieke G. H., Muzerolle J., Gáspár A., Young E. T., Gorlova N., 2009, ApJ, 698, 1989

Baruteau C., et al., 2014, in Beuther H., Klessen R. S., Dullemond C. P., Henning T., eds, Protostars and Planets VI. p. 667 (arXiv:1312.4293), doi:10.2458/azu˙uapress˙9780816531240-ch029

Benz W., Asphaug E., 1999, Icarus, 142, 5

Bergin E. A., Tafalla M., 2007, ARA&A, 45, 339

Bjorkman J. E., Wood K., 2001, ApJ, 554, 615

Blum J., Wurm G., 2008, ARA&A, 46, 21

Bonomo A. S., et al., 2019, Nature Astronomy, 3, 416

Boss A. P., 1997, Science, 276, 1836

Boss A. P., 2011, ApJ, 731, 74

Brož M., Chrenko O., Nesvorný D., Dauphas N., 2021, Nature Astronomy, 5, 898

Burkhardt C., Spitzer F., Morbidelli A., Budde G., Render J. H., Kruijer T. S., Kleine T., 2022, arXiv e-prints, p. arXiv:2201.08092

Cai K., Durisen R. H., Michael S., Boley A. C., Mejía A. C., Pickett M. K., D'Alessio P., 2006, ApJ, 636, L149

Canup R. M., 2004, ARA&A, 42, 441

Canup R. M., 2008, Icarus, 196, 518

Carter P. J., Leinhardt Z. M., Elliott T., Walter M. J., Stewart S. T., 2015, ApJ, 813, 72

Carter P. J., Leinhardt Z. M., Elliott T., Stewart S. T., Walter M. J., 2018, Earth and Planetary Science Letters, 484, 276

Carter P. J., Lock S. J., Stewart S. T., 2019a, Replication Data for: "The energy budgets of giant impacts", doi:10.7910/DVN/YYNJSX, `https://doi.org/10.7910/DVN/YYNJSX`

Carter P. J., Davies E. J., Lock S. J., Stewart S. T., 2019b, in Lunar and Planetary Science Conference. Lunar and Planetary Science Conference. p. 1246

Carter P. J., Lock S. J., Stewart S. T., 2020, Journal of Geophysical Research (Planets), 125, e06042

Chambers J. E., Wetherill G. W., 1998, Icarus, 136, 304

Chen C. H., et al., 2006, ApJS, 166, 351

Clement M. S., Kaib N. A., Raymond S. N., Walsh K. J., 2018, Icarus, 311, 340

Clement M. S., Kaib N. A., Raymond S. N., Chambers J. E., Walsh K. J., 2019, Icarus, 321, 778

Clement M. S., Kaib N. A., Raymond S. N., Chambers J. E., 2021, Icarus, 367, 114585

Ćuk M., Stewart S. T., 2012, Science, 338, 1047

Davies E. J., Root S., Carter P. J., Duncan M. S., Spaulding D. K., Kraus R. G., Stewart S. T., Jacobsen S. B., 2019, in Lunar and Planetary Science Conference. Lunar and Planetary Science

Conference. p. 1257

Davies E. J., Carter P. J., Root S., Kraus R. G., Spaulding D. K., Stewart S. T., Jacobsen S. B., 2020, Journal of Geophysical Research (Planets), 125, e06227

Denman T. R., Leinhardt Z. M., Carter P. J., Mordasini C., 2020, MNRAS, 496, 1166

Dohnanyi J. S., 1969, J. Geophys. Res., 74, 2531

Dorschner J., Begemann B., Henning T., Jaeger C., Mutschke H., 1995, A&A, 300, 503

Draine B. T., 2003, ARA&A, 41, 241

Dullemond C. P., Juhasz A., Pohl A., Sereshti F., Shetty R., Peters T., Commercon B., Flock M., 2012, RADMC-3D: A multi-purpose radiative transfer tool, Astrophysics Source Code Library, record ascl:1202.015 (ascl:1202.015)

Fu R. R., Kehayias P., Weiss B. P., Schrader D. L., Bai X.-N., Simon J. B., 2020, Journal of Geophysical Research (Planets), 125, e06260

Fujiwara H., et al., 2010, ApJ, 714, L152

Fujiwara H., et al., 2013, A&A, 550, A45

Gabriel T. S. J., Allen-Sutter H., 2021, ApJ, 915, L32

Genda H., Kobayashi H., Kokubo E., 2015, ApJ, 810, 136

Genda H., Iizuka T., Sasaki T., Ueno Y., Ikoma M., 2017, Earth and Planetary Science Letters, 470, 87

Ginzburg S., Chiang E., 2020, MNRAS, 498, 680

Gomes R., Levison H. F., Tsiganis K., Morbidelli A., 2005, Nature, 435, 466

Gorlova N., et al., 2004, ApJS, 154, 448

Gorlova N., Balog Z., Rieke G. H., Muzerolle J., Su K. Y. L., Ivanov V. D., Young E. T., 2007, ApJ, 670, 516

Greenberg R., Wacker J. F., Hartmann W. K., Chapman C. R., 1978, Icarus, 35, 1

Grigorieva A., Artymowicz P., Thébault P., 2007, A&A, 461, 537

Günther H. M., et al., 2017, A&A, 598, A82

Halliday A. N., 2000, Earth and Planetary Science Letters, 176, 17

Hansen B. M. S., 2009, ApJ, 703, 1131

Hernández J., et al., 2007, ApJ, 662, 1067

Hillenbrand L. A., et al., 2008, ApJ, 677, 630

Holsapple K. A., 1994, Planet. Space Sci., 42, 1067

Housen K. R., Holsapple K. A., 1990, Icarus, 84, 226

Hughes A. M., Duchêne G., Matthews B. C., 2018, ARA&A, 56, 541

Ida S., Makino J., 1992, Icarus, 96, 107

Ida S., Makino J., 1993, Icarus, 106, 210

Jackson A. P., Wyatt M. C., 2012, MNRAS, 425, 657

Jackson A. P., Wyatt M. C., Bonsor A., Veras D., 2014, MNRAS, 440, 3757

Johansen A., Jacquet E., Cuzzi J. N., Morbidelli A., Gounelle M., 2015, in , Asteroids IV. pp 471–492, doi:10.2458/azu_uapress_9780816532131-ch025

Johansen A., Ronnet T., Bizzarro M., Schiller M., Lambrechts M., Nordlund Å., Lammer H., 2021, Science Advances, 7, eabc0444

Johnson B. C., Melosh H. J., 2012, Icarus, 217, 416

Johnson B. C., Melosh H. J., 2014, Icarus, 228, 347

Kegerreis J. A., Eke V. R., Gonnet P., Korycansky D. G., Massey R. J., Schaller M., Teodoro L. F. A., 2019, MNRAS, 487, 5029

Kennedy G. M., Wyatt M. C., 2013, MNRAS, 433, 2334

Kenyon S. J., Bromley B. C., 2016, ApJ, 817, 51

Kokubo E., Ida S., 1995, Icarus, 114, 247

Kokubo E., Ida S., 1998, Icarus, 131, 171

Kokubo E., Ida S., 2000, Icarus, 143, 15

Kokubo E., Ida S., 2002, ApJ, 581, 666

Kral Q., Thébault P., Augereau J. C., Boccaletti A., Charnoz S., 2015, A&A, 573, A39

Kral Q., et al., 2017, The Astronomical Review, 13, 69

Lambrechts M., Morbidelli A., Jacobson S. A., Johansen A., Bitsch B., Izidoro A., Raymond S. N., 2019, A&A, 627, A83

Leinhardt Z. M., Richardson D. C., 2005, ApJ, 625, 427

Leinhardt Z. M., Stewart S. T., 2012, ApJ, 745, 79

Lewis T., Watt L., Leinhardt Z. M., 2023, MNRAS, 519, 172

Lin D. N. C., Bodenheimer P., Richardson D. C., 1996, Nature, 380, 606

Lisse C. M., Sitko M. L., Marengo M., 2015, ApJ, 815, L27

Lisse C. M., et al., 2020, ApJ, 894, 116

Liu L.-G., 1975, Geophysical Journal, 43, 697

Lock S. J., Stewart S. T., Petaev M. I., Leinhardt Z., Mace M. T., Jacobsen S. B., Cuk M., 2018, Journal of Geophysical Research (Planets), 123, 910

Luger R., et al., 2017, Nature Astronomy, 1, 0129

Marcus R. A., Stewart S. T., Sasselov D., Hernquist L., 2009, ApJ, 700, L118

Matzner C. D., Levin Y., 2005, ApJ, 628, 817

Mayor M., Queloz D., 1995, Nature, 378, 355

Melis C., Zuckerman B., Rhee J. H., Song I., 2010, ApJ, 717, L57

Melis C., Zuckerman B., Rhee J. H., Song I., Murphy S. J., Bessell M. S., 2012, Nature, 487, 74

Melis C., Olofsson J., Song I., Sarkis P., Weinberger A. J., Kennedy G., Krumpe M., 2021, ApJ, 923, 90

Melosh H. J., 2007, Meteoritics and Planetary Science, 42, 2079

Meng H. Y. A., Rieke G. H., Su K. Y. L., Ivanov V. D., Vanzi L., Rujopakarn W., 2012, ApJ, 751, L17

Meng H. Y. A., et al., 2014, Science, 345, 1032

Meng H. Y. A., et al., 2015, ApJ, 805, 77

Meng H. Y. A., Rieke G. H., Su K. Y. L., Gáspár A., 2017, ApJ, 836, 34

Min M., Hovenier J. W., de Koter A., 2005, A&A, 432, 909

Mittal T., Chen C. H., Jang-Condell H., Manoj P., Sargent B. A., Watson D. M., Lisse C. M., 2015, ApJ, 798, 87

Monaghan J. J., 1997, Journal of Computational Physics, 136, 298

Moór A., et al., 2021, ApJ, 910, 27

Morbidelli A., Levison H. F., Tsiganis K., Gomes R., 2005, Nature, 435, 462

Morris M. A., Garvie L. A. J., Knauth L. P., 2015, ApJ, 801, L22

Murakami H., et al., 2007, PASJ, 59, S369

NASA Exoplanet Archive 2022, Confirmed Planets Table, doi:10.26133/NEA12, `https://exoplanetarchive.ipac.caltech.edu/cgi-bin/TblView/nph-tblView?app=ExoTbls&config=PS`

Nagahara H., Kushiro I., Mysen B. O., 1994, Geochim. Cosmochim. Acta, 58, 1951

Neugebauer G., et al., 1984, ApJ, 278, L1

Olofsson J., Juhász A., Henning T., Mutschke H., Tamanai A., Moór A., Ábrahám P., 2012, A&A, 542, A90

Ormel C. W., 2017, in Pessah M., Gressel O., eds, Astrophysics and Space Science Library Vol. 445, Formation, Evolution, and Dynamics of Young Solar Systems. p. 197, doi:10.1007/978-3-319-60609-5˙7

Pierens A., Raymond S. N., 2011, A&A, 533, A131

Pilbratt G. L., et al., 2010, A&A, 518, L1

Quintana E. V., Barclay T., Borucki W. J., Rowe J. F., Chambers J. E., 2016, ApJ, 821, 126

Raymond S. N., Izidoro A., 2017, Science Advances, 3, e1701138

Raymond S. N., Kokubo E., Morbidelli A., Morishima R., Walsh K. J., 2014, in Beuther H., Klessen R. S., Dullemond C. P., Henning T., eds, Protostars and Planets VI. p. 595 (arXiv:1312.1689), doi:10.2458/azu_uapress_9780816531240-ch026

Rein H., Liu S. F., 2012, A&A, 537, A128

Rhee J. H., Song I., Zuckerman B., 2008, ApJ, 675, 777

Schaller M., et al., 2018, SWIFT: SPH With Inter-dependent Fine-grained Tasking, Astrophysics Source Code Library (ascl:1805.020)

Schrader D. L., Nagashima K., Waitukaitis S. R., Davidson J., McCoy T. J., Connolly H. C., Lauretta D. S., 2018, Geochim. Cosmochim. Acta, 223, 405

Shannon A., Bonsor A., Kral Q., Matthews E., 2016, MNRAS, 462, L116

Shoemaker E. M., 1962, Physics and astronomy of the moon (New York: Academic)

Simon J. B., Armitage P. J., Li R., Youdin A. N., 2016, ApJ, 822, 55

Springel V., 2005, MNRAS, 364, 1105

Su K. Y. L., et al., 2019, AJ, 157, 202

Su K. Y. L., Rieke G. H., Melis C., Jackson A. P., Smith P. S., Meng H. Y. A., Gáspár A., 2020, ApJ, 898, 21

Su K. Y. L., Kennedy G. M., Schlawin E., Jackson A. P., Rieke G. H., 2022, ApJ, 927, 135

Thébault P., Augereau J. C., 2007, A&A, 472, 169

Thebault P., Kral Q., 2018, A&A, 609, A98

Thorngren D. P., Fortney J. J., Murray-Clay R. A., Lopez E. D., 2016, ApJ, 831, 64

Toomre A., 1964, ApJ, 139, 1217

Toon O. B., Ackerman T. P., 1981, Appl. Opt., 20, 3657

Tsiganis K., Gomes R., Morbidelli A., Levison H. F., 2005, Nature, 435, 459

Valencia D., O'Connell R. J., Sasselov D., 2006, Icarus, 181, 545

Walsh K. J., Morbidelli A., Raymond S. N., O'Brien D. P., Mandell A. M., 2011, Nature, 475, 206

Watt L., Leinhardt Z., Su K. Y. L., 2021, MNRAS, 502, 2984

Weinberger A. J., Becklin E. E., Song I., Zuckerman B., 2011, ApJ, 726, 72

Werner M. W., et al., 2004, ApJS, 154, 1

Wetherill G. W., Stewart G. R., 1989, Icarus, 77, 330

Wettlaufer J. S., 2010, ApJ, 719, 540

Williams J. P., Cieza L. A., 2011, ARA&A, 49, 67

Woitke P., et al., 2016, A&A, 586, A103

Wolszczan A., Frail D. A., 1992, Nature, 355, 145

Wright E. L., et al., 2010, AJ, 140, 1868

Wyatt M. C., 2008, ARA&A, 46, 339

Wyatt M. C., Jackson A. P., 2016, Space Sci. Rev., 205, 231

Wyatt M. C., Bonsor A., Jackson A. P., Marino S., Shannon A., 2017, MNRAS, 464, 3385

Zubko V. G., Mennella V., Colangeli L., Bussoletti E., 1996, MNRAS, 282, 1321

Zuckerman B., 2015, ApJ, 798, 86

Zuckerman B., Melis C., Rhee J. H., Schneider A., Song I., 2012, ApJ, 752, 58

de Wit W. J., Grinin V. P., Potravnov I. S., Shakhovskoi D. N., Müller A., Moerchen M., 2013, A&A, 553, L1